Optical Waveguide Interconnects in Optoelectronic Matrix Switches.

Optical Waveguide Interconnects in Optoelectronic Matrix Switches.

by

Michael Ersoni, B.Sc.

A Thesis

Submitted to the School of Graduate Studies

in Partial Fulfilment of the Requirements

For the Degree

Master of Engineering

December 1995

Master of Engineering (1995) **McMaster University**

Department of Engineering Physics **Hamilton, Ontario**

Title: Optical Waveguide Interconnects in Optoelectronic Matrix Switches

Author: Michael Ersoni, B.Sc. (Concordia University)

Supervisor: Dr. Paul E. Jessop

No. of pages: i-xii, 1-104

Abstract

The speed and simplicity of the metal-semiconductor-metal (MSM) detector has made it a prime candidate for use in integrated optoelectronic circuits. While in most applications the optical input is coupled in through the top surface of the device, it is also possible to distribute the optical signal by means of transparent waveguides that are located below the absorbing detector layer. By controlling the degree of coupling between the waveguide and detector layers the detectors can be made to act as optical taps. The optical signal can thus be shared among a series of detectors as required in optoelectronic switching applications. We have made a series of simple ridge waveguides, each with a number of MSM structures designed for the characterization of absorption, responsivity and frequency response. A 4x4 optoelectronic switch was also fabricated and analyzed. We show that balancing the switch is accomplished by tailoring the absorption coefficient in the detector region so that all detectors absorb equal amounts of optical power.

ACKNOWLEDGEMENTS

The author would like to thank Dr. Paul Jessop for his supervision and constant patience throughout this work. I would also like to thank my parents, and fiance for supporting and helping me get through the good times and the bad. I would like to thank all the wonderful people I met at McMaster, especially the members of my group, Dr. Doug Bruce, Tullio Pannarello, Wu, David and Kevin, who at various times have all helped me through this entire work. All the soccer guys I played with, I'm really going to miss you guys, thanks for all the games. Finally I would like to thank God, who never spoke to me directly, but was always there to motivate and help me.

TABLE OF CONTENTS

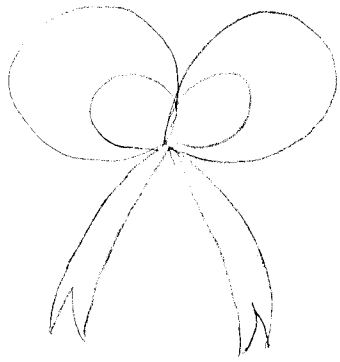

LIST OF FIGURES

LIST OF TABLES

Chapter 1: Introduction

Over the past few years there has been a rapid increase in the amount of information transferred in point to point communication links. The proper routing and splitting of signals has created the need for ultra-fast and accurate detection systems. Typically the incoming information is split and then separated with the use of matrix switches. Recently there has been a push for faster and more efficient integrated optoelectronic components because of their relatively large bandwidths and high speed performance.

The basic operation of a matrix switch is not very complicated. It essentially consists of an array of N input data ports with N output ports. The information is input into the N input ports and the output can be taken from any one of the output ports. An essential requirement of switches is that any one of the output ports be able to tap into the information of any selected input port, while rejecting the signal from the other input ports. The majority of modern communication systems will typically transmit information over long distances by fiber and then convert the information to electrical signals where the switching (routing) of the data is accomplished. With the recent advances of integrated photonic communication systems, electrical switching has become a less attractive research venue. This has created a need for integrated optoelectronic switches that can maintain the high data transfer rates. An optoelectronic version of a matrix switch is illustrated in Figure 1.1. Veilleux et al. have already demonstrated an optoelectronic switch which injects the signal in through the top of the device [1]. In our system the information is carried via multimode fibers and injected into a semiconductor waveguide-detector structure. The optical signal is distributed to the detectors by routing it through transparent waveguides that are located directly below the absorbing detector layers. The amount of optical power absorbed in each detector section can be controlled by adjusting the degree of coupling between detector layer and waveguide. The optical signal can then be shared among a series of detectors as is required in optoelectronic switching applications.

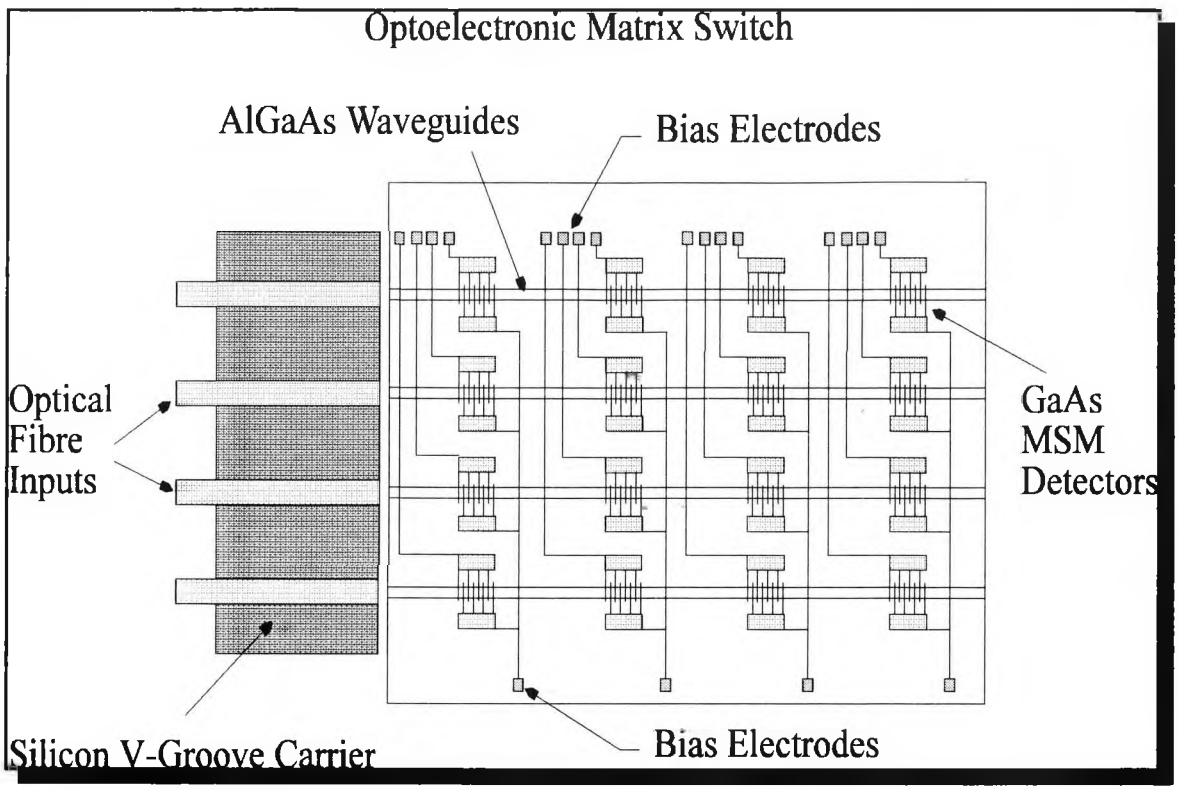

Figure 1.1 An optoelectronic switch which distributes the incoming optical signal to detectors, through transparent waveguides located vertically below the detectors.

As was previously mentioned, current switching technology is essentially carried out using electronic switches. Although this technology is well established, a major obstacle at high frequencies is electromagnetic cross coupling. This is a natural consequence of the linear frequency dependence of inductive electronic components. As the frequency increases the inductive impedance will eventually degrade any measurable signal, and will also begin to act as a receiver antenna for adjacent components. To reduce or eliminate the electronically generated noise, the use of expensive and sophisticated compensating electronics is required [2,3]. Furthermore, because modern communication links employ fiber optic cables in long haul communication, the use of fiber splitters in simple optoelectronic switches is both lossy and difficult. These losses can be avoided by not transferring the incoming signal to electrical as is done in an electrical switch and utilizing a modified optoelectronic switch illustrated in Figure 1.1. The use of multiple detectors, distributed in-line along a common waveguide would eliminate the use of bulky fiber splitters and the need for difficult fiber alignments.

Proper operation of the optoelectronic switch requires a number of fairly important system specifications. The detectors must be relatively fast with switching (On-Off) times in the low picoseconds [1]. The isolation of the detectors, which is defined as the ratio of on state power to off state power, should be no lower than 50dB [1], and the optical crosstalk between adjacent waveguides should be approximately zero. Metal-Semiconductor-Metal (MSM) detectors have become one of the most commonly used detectors for optoelectronic matrix switch applications, because of both their relatively high bandwidths, which have been shown to be in excess of 15 GHz [4], and zero volt off states. These properties make MSMs extremely attractive for use in large array switches. For example, in a 1000x1000 element switch, the routing of the signal into one output would require the biasing of one detector. All other output ports would have zero bias and present zero signal at the output. This is in contrast to p-n or p-i-n photodiodes that must be forward biased to be rendered insensitive to the incident optical signal. In such a case all the elements in the switch must be forward biased and only the required output port detector would be reverse biased. The use of p-n or p-i-n photodiodes would therefore require a large amount of power consumption which is not practical in real life applications.

This thesis examines the integration of GaAs/AlGaAs based waveguide-detectors and the operation of a 4x4 optoelectronic matrix switch. The transparent AlGaAs waveguides will be used to carry the optical information to the absorbing GaAs detector sections located above the waveguide (See Figure 1.2) as described above.

Chapter Two examines the theory of electromagnetic wave propagation and investigates all major loss mechanisms in semiconductor waveguides. Using this information a single and multimode integrated waveguide-detector structure is modelled. The optimized structures were then grown by Metal Organic Chemical Vapour Deposition (MOCVD) at the Communication Research Centre (CRC).

Chapter Three introduces some important properties of detectors and more specifically presents a derivation of the current expected to flow in a MSM photodiode and photoconductor. This analysis will be essential in properly analyzing both the dc and high speed response of the experimentally fabricated devices.

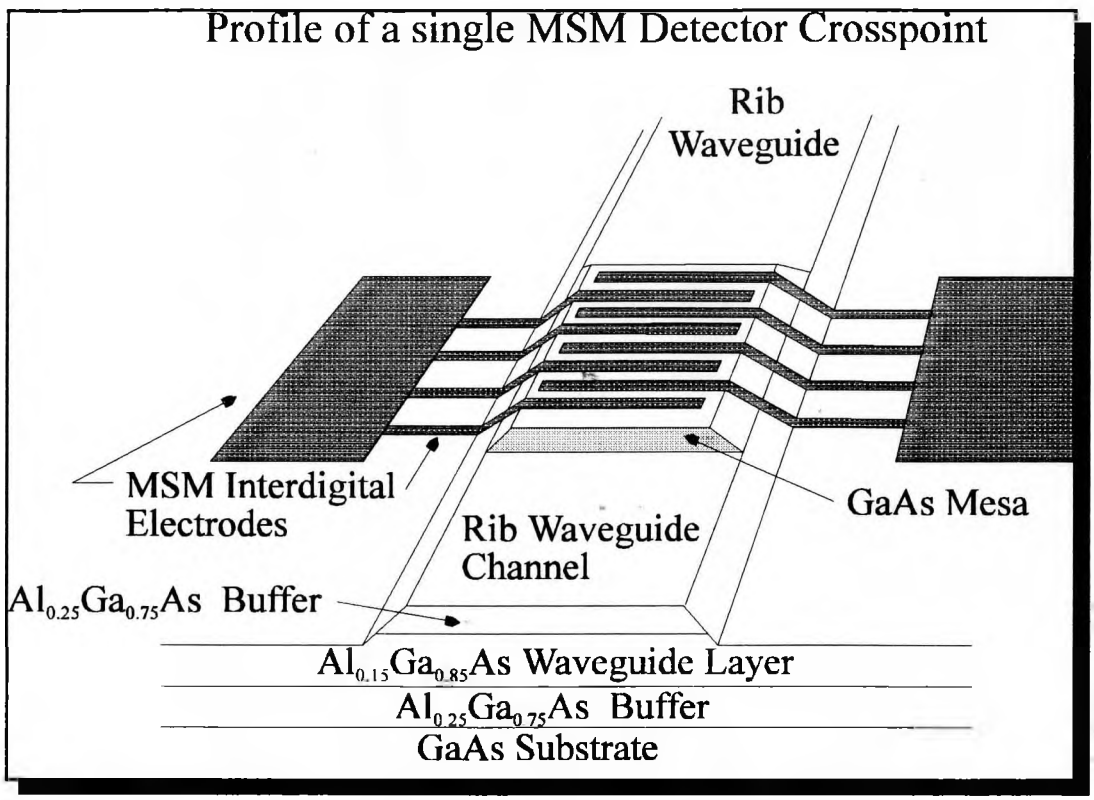

Figure 1.2 Detector, waveguide cross-section in optoelectronic matrix switch.

Chapter Four presents a detailed summary and analysis of all experimental data acquired. We first examine the optical characterization of both the passive and detector regions. Using the experimentally determined values for the losses in the waveguides, the dc responsivities will be determined. As a final analysis, the frequency response will then be presented and compared with expected theoretical values.

Chapter Five will conclude with some very important recommendations for improvements that can be made to our system which will greatly increase the performance and manufacturability of the switch. Finally, Appendix One will review the basic processing information used in the device fabrication and briefly discuss the design and logic used in the design of the optoelectronic mask.

Chapter 2: Waveguide Theory

2.1) Introduction

The integration of optoelectronic components would be an impossibility without the use of waveguides. The equivalent of wires in electrical circuits, waveguides are the interconnects of integrated optical components, their proper operation is essential. This chapter will be devoted to the theoretical analysis of optical wave propagation in semiconductor waveguides. Using Maxwell's equations, section 2.2 will solve for guided mode solutions of the three layer planar waveguide. This will lead to concepts such as guided optical modes (guided waves), radiation modes (scattered light), and attenuation. After the theoretical framework of waveguides is established, a basic understanding of ridge waveguides, and the effective index method will be presented. Using this information, a proper etch depth for the fabricated waveguides will be determined. Section 2.4 will then examine the loss mechanisms in semiconductor waveguides and material systems, where an expression for the absorption coefficient of direct band-gap semiconductors will be derived. Finally, in section 2.6 a suitable device structure will be introduced and modelled using the theory developed in previous sections.

2.2) Basic Three Layer Planar Waveguide:

The basic three layer planar waveguide is composed of three different materials with dissimilar indices of refraction, see Figure 2.1. There exists an infinite cladding layer n_1, substrate layer n_3, and a waveguiding layer n_2, with thickness t_g. It can be shown that to obtain optically confined modes, it is essential that $n_2 > n_3, n_1$. This condition can be obtained by using Snell's law and imposing that there be no refracted ray at the $(n_1 - n_2)$ and $(n_2 - n_3)$

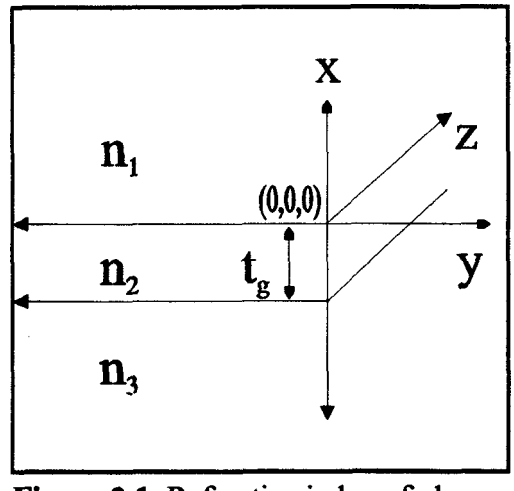

Figure 2.1 Refractive index of planar waveguide structure.

interfaces. To obtain a general solution of the planar waveguide structure, Maxwell's equations in time varying point differential form will be solved, and can be stated as,

$$\nabla \cdot \overline{D} = \rho \tag{1}$$

$$\nabla \cdot \overline{B} = 0 \tag{2}$$

$$\nabla \times \overline{E} = -\frac{\partial \overline{B}}{\partial t} \tag{3}$$

$$\nabla \times \overline{H} = \frac{\partial \overline{D}}{\partial t} + \overline{J}. \tag{4}$$

Where the above quantities are defined as follows:

E the electric field intensity, in V/m.
D the electric displacement vector, in Coul/m^2.
H the magnetic field intensity, in A/m.
B the magnetic flux density vector, Wb/m^2.
J the electric current density, in A/m^2.
ρ the electric charge density, in Coul/m^2.

Stated in general form, Maxwell's equations (1- 4) are, for most applications unusable. Because all electromagnetic fields generally have a sinusoidal time dependence, it is possible to specify the time dependence of the fields in the form of $\mathbf{E}(\mathbf{r},t)= \mathbf{E}(\mathbf{r})e^{j\omega t}$. Maxwell's equations are then transformed into,

$$\nabla \cdot \overline{D} = \rho \tag{5}$$

$$\nabla \cdot \overline{B} = 0 \tag{6}$$

$$\nabla \times \overline{E} = -j\omega\overline{B} \tag{7}$$

$$\nabla \times \overline{H} = j\omega\overline{D} + \overline{J}. \tag{8}$$

Assuming a source-free, linear, isotropic, homogeneous medium, Maxwell's curl equations can be combined with the divergence equations to give the Helmholtz's equations.

$$\nabla^2\overline{H} + \omega^2\mu\epsilon\overline{H} = 0 \tag{9}$$

$$\nabla^2\overline{E} + \omega^2\mu\epsilon\overline{E} = 0 \tag{10}$$

Where $k = \omega(\mu\epsilon)^{1/2} = \omega/v_p$ is normally defined as the propagation constant, or wave number. Because Helmholtz's equations are derived from Maxwell's, in applying the appropriate boundary conditions to the **E(r)** and **B(r)** fields, we will simultaneously solve equations 5-8.

2.3) Solution of Electromagnetic Equations in a Planar Waveguide

The solution of Maxwell's equations in an infinite planar waveguide can be naturally divided into two physical cases. We can solve equations 9 or 10 by considering either the transverse electric (TE) or transverse magnetic (TM) polarized waves. Because the method of solution in both cases is similar, only TE modes will be solved. Elementary electromagnetism [5] shows that TE waves propagating in the z direction have no x or z electric component and therefore, equation 9 reduces to,

$$\nabla^2 E_y + \omega^2\mu\epsilon E_y = 0. \tag{11}$$

The solution of equation 11 is of the following form,

$$E_y(x,z,t) = E_y(x)e^{i(\omega t-\beta z)}. \tag{12}$$

Where ω is the frequency of the wave, and β is the propagation constant in the z direction. An immediate consequence of equation 12 is that the velocity component in the z-direction can be expressed as $v_z = \omega/\beta = 2\pi\nu/\beta = c2\pi/\beta\lambda = c\,(k/\beta)$, which allows for the determination of the effective index of the medium, $n_{eff} = \beta/k$. This result will be important in the analysis of ridge waveguides. Equations 11 and 12 must hold true in each dielectric layer. The boundary conditions for a TE polarized electric field at a dielectric interface require the continuity of both the electric field and its derivative. Furthermore, to obtain a well behaved travelling wave solution of equation 11, the transverse function $E_y(x)$ must have the following form in each dielectric layer,

$$E_y(x) = A\exp(-qx), \qquad 0 \le x \le \infty; \tag{13}$$

$$E_y(x) = B\cos(hx) + C\sin(hx), \qquad -t_g \le x \le 0; \tag{14}$$

$$E_y(x) = D\exp[p(x+t_g)], \qquad -\infty \le x \le -t_g. \tag{15}$$

This simply requires that the field decay exponentially outside the waveguiding region and be confined sinusoidally inside. The constants A,B,C,D,q,h,p will be determined by applying the boundary conditions at each dielectric interface. More specifically, by requiring the electric field to be continuous at the dielectric interfaces, equations 13-15 can be recast into the following form,

$$E_y(x) = C'\exp(-qx), \qquad 0 \le x \le \infty; \tag{16}$$

$$E_y(x) = C'\cos(hx) - \frac{q}{h}\sin(hx), \qquad -t_g \le x \le 0; \tag{17}$$

$$E_y(x) = C'\left[\cos(ht_g) + \frac{q}{h}\sin(ht_g)\right]\exp[p(x + t_g)], \qquad -\infty \le x \le -t_g; \tag{18}$$

Substituting equations 16-18 into equation 12, and the result into equation 11, we obtain the following conditions, for all three regions,

$$q = (\beta^2 - n_1^2 k^2)^{1/2}, \tag{19}$$

$$h = (n_2^2 k^2 - \beta^2)^{1/2}, \tag{20}$$

$$p = (\beta^2 - n_3^2 k^2)^{1/2}, \tag{21}$$

$$k \equiv \frac{\omega}{c} \tag{22}$$

To obtain the complete solution for the planar waveguide it is necessary to apply the final boundary condition of the electric field, more specifically we require that $\partial E_y / \partial x$ be continuous at $x = -t_g$. This leads to the last and final condition,

$$\tan(ht_g) = \frac{p + q}{h(1 - pq/h^2)}. \tag{23}$$

The above equations 19-21, and 23, can be combined to represent, 1 equation in 1 unknown which must be solved either numerically or graphically. The method of solution does not concern us as much as the results, which essentially show that the solution is obtained by solving for the propagation constant in the z direction, β_m, where each m'th modal solution is an optically guided mode. Figure 2.2 illustrates how the power[1] is distributed in a single mode AlGaAs/GaAs three layer planar waveguide.

An important consequence of the above solution method is that it forms the foundation for solutions of more complicated, n-layer dielectric waveguides. The object of all numerical solution methods is to solve the wave equation for guides optical modes. For instance, the matrix transfer method, which is used to solve n-layer waveguides, solves the wave equation in each dielectric

[1] The power is simply the square of the electric field.

layer and then imposes the continuity requirements on both the fields and their derivatives using matrices [6,7]. The basic physics of the matrix transfer method is no different than the method of solution employed above. The solutions of the E and B fields are sill confined, and only specific modes can propagate in the waveguide.

A limitation of the above solution methods is that a modal analysis is employed. In most

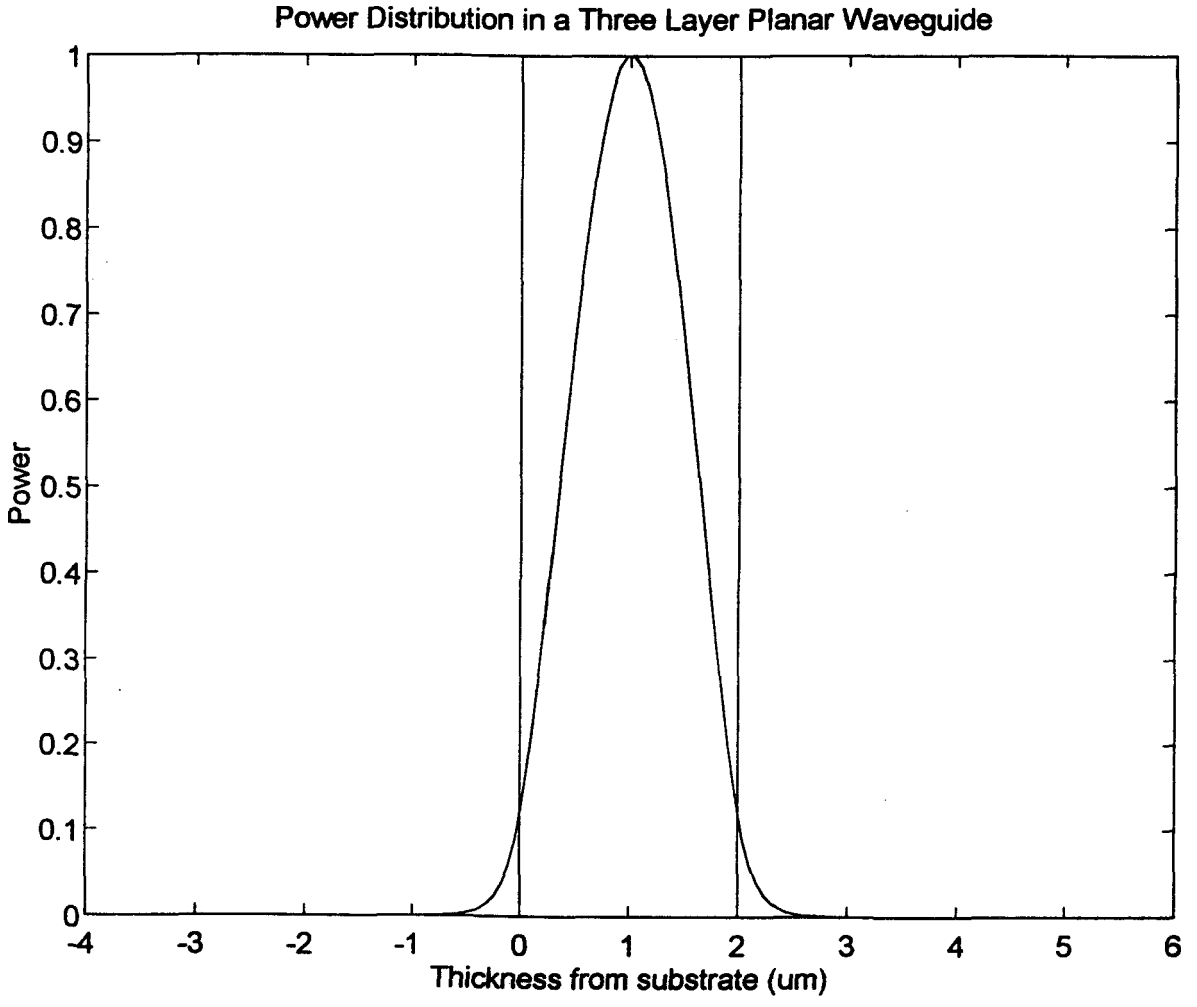

Figure 2.2 Modal solution of a three layer planar waveguide.

applications the waveguiding geometries are too complicated to examine exactly, therefore simplifications are required to determine the waveguiding solutions. For instance, the beam

propagation method, BPM, [8] solves the wave equation in a much more general way. In this method, the medium, with a continuous index of refraction, n(x,y,z), is replaced by a discontinuous index of refraction along the propagation axis. The electromagnetic wave is then propagated down the waveguide from point to point (also called lenses, not in the conventional sense but in a representational sense of the medium.) thus obtaining a solution for the propagation of electromagnetic energy. A major limitation of the BPM is that reflected beams are ignored. This however, does not cause any concern since, for straight transparent waveguides, the majority of the optical power is either absorbed by the detectors or transmitted into free space.

Another important approximation method is the solution of ridge waveguides using the effective index method. Originally introduced by Knox and Toulios [7] this method derives from the results obtained for the three layer planar waveguide above. Since for each planar waveguide there exists an effective index, a ridge waveguide can be solved by finding the effective index for all three planar waveguide regions, and then solving for the effective index in the vertical direction to ensure proper confinement of the fields in the lateral direction [7], see Figure 2.3. The electric field can then be expressed as a product of both solutions, $E(x,y)=E(x)E(y)$. Once the proper index changes have been determined so will the proper etch depth. Later in this chapter, both BPM and matrix transfer methods will be used to determine a suitable waveguiding structure for our devices.

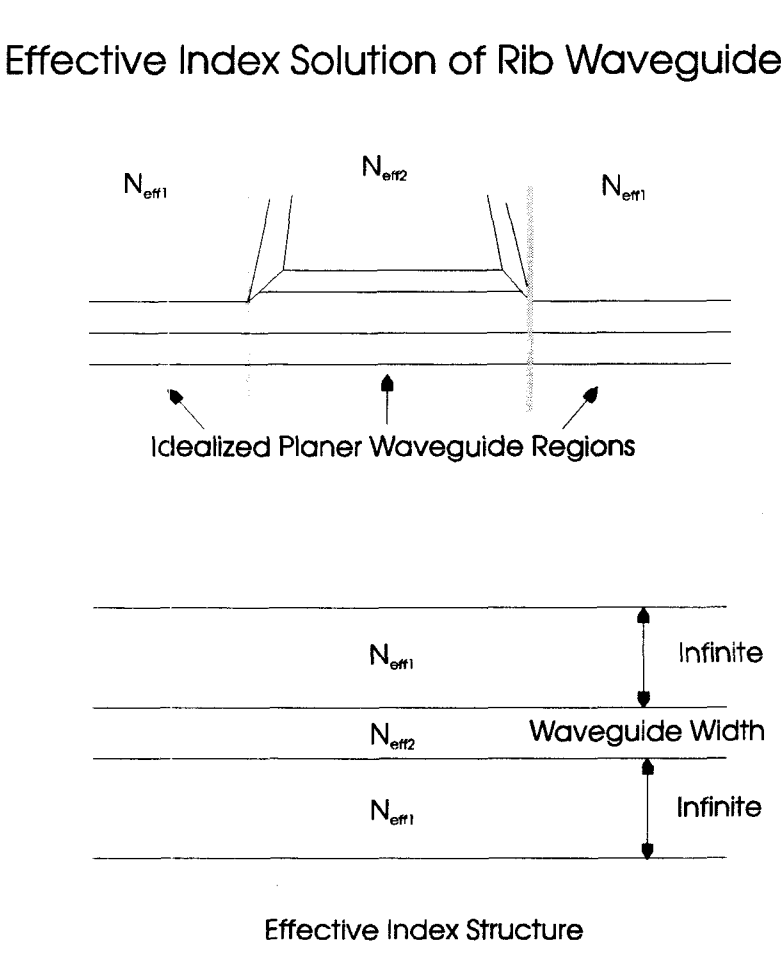

Figure 2.3 Solution of rib waveguide using the effective index method.

2.4) Losses in Optical Waveguides

There are three types of waveguide losses that can severely degrade the performance of optoelectronic devices: scattering, absorption and radiative losses. Scattering losses are essentially composed of two major groups, volume and surface. In the case of semiconductors, scattering losses can, and usually are neglected. This is so because for volume losses, which are incurred because of defects, voids, and dopants present in the semiconductor, the optical wavelengths are large in comparison to the size of these imperfections; therefore, they rarely present any type of problem. Surface scattering, like volume scattering does not present a problem for

semiconductors since, the surface roughness of semiconductors is typically on the order of 0.01μm [9] which is smaller than most optical wavelengths encountered in semiconductors.

The most predominant loss mechanism for semiconductor waveguides, is absorption. Because these losses are an important and a non negligible part of optoelectronic devices, in this section we will derive the absorption coefficient for direct band-gap semiconductors and review the loss mechanisms in semiconductor waveguides from a quantum mechanical point of view.

Finally, radiation losses, like absorption losses, can be a concern in semiconductor materials, but only for waveguides that have non conventional geometries, i.e., if the waveguides have bends in them. Since both the 4x4 switch and the waveguide integrated detectors contain no bends, radiation losses will be ignored. For further reading the reader is referred to Tamir [7].

There are several different mechanisms than can lead to photon absorption in semiconductors. Absorbed photons can cause electrons or holes to undergo any one of the following transitions, band-to-band transitions, dopant level to band transitions, free carrier absorption (intraband absorption), phonon transitions, and exciton transitions[2]. Each absorption mechanism will contribute to the overall absorption coefficient of the material defined as alpha $\alpha(cm^{-1})$. [Losses in optical waveguide are often represented as an exponential decay with power, ie. $I=I_0 \exp(-\alpha x)$. This result can be obtained by assuming a lossy (conductivity σ) medium and solving Maxwell's equation for the electric field amplitudes, the result will be an oscillating electric field with an exponentially decreasing amplitude.]

The study of how photons interact with matter, at a quantum mechanical level, can quickly exceed the scope of this thesis, therefore the definition of certain physical quantities such as the probability density function for absorption/stimulated emission will be stated without proof. (These topics are dealt with at a more fundamental level using quantum electrodynamics QED.) Since direct band-gap semiconductor absorption may be treated as a two level electronic transition, (electron is moved from valence to conduction band.) lets examine an atom with only

---

[2] Band to Band transitions; electrons in lower energy states can absorb photons and jump to a different energy band. Dopant to band transitions; electrons in lower energy states can be excited to impurity energy levels, thereby creating free holes (In p-type.). Free Carrier absorption; electrons absorb photons but remain in the same energy band. Phonon transitions; because phonons, (Lattice vibrations.) are not very energetic only low energy, long wavelength photons absorbed can cause these particles to be created. This is illustrated in the experimentally observed value of the absorption coefficient $\alpha(\nu)$. Excitonic transitions; absorbed photons can cause a created electron-hole pair to be coulombicly attracted and circle about their centre of mass.

two energy levels, placed inside an optical resonator. The objective is to understand how the atom will interact with photons inside the resonator, and to obtain the probability density for the absorption of photons with energy $E=h\nu_0$ so that an electron will undergo an electronic transition from E_1 to E_2.

In any physical transition processes, energy and momentum must always be conserved. Conservation of energy demands that $h\nu_0 = E_2 - E_1$, where E_2 and E_1 are the electron energy levels, and conservation of momentum requires that the total momentum transfer of all involved particles be zero. Since the momentum of electrons is much larger than that of photons conservation of momentum essentially implies, $k_1 \approx k_2$ [3]. To obtain the conservation of energy condition, we simply approximate the energy levels in the conduction and valence band by assuming parabolic bands, thereby obtaining,

$$E_2 - E_1 = \frac{h^2 k^2}{2\pi^2 m_v} + E_g + \frac{h^2 k^2}{2\pi^2 m_c} = h\nu. \tag{24}$$

For direct band-gap semiconductors we can express the wave-vector k as follows,

$$k^2 = \frac{2m_r}{(h/2\pi)^2}(h\nu - E_g), \qquad \text{where} \quad \frac{1}{m_r} = \frac{1}{m_v} + \frac{1}{m_c}. \tag{25}$$

The probability density (transition probability of absorption per second) is defined as [10],

$$p_{ab} = n\frac{c}{V}\sigma(\nu), \quad s^{-1} \tag{26}$$

---

[3] This is an important result, because a photon can raise the electron to a different energy level but it cannot change how it moves though the crystal lattice, ie the momentum. This is why indirect band-gap semiconductors are unsuitable for lasers, the carriers require assistance in making a change in momentum, usually with the aid of phonons.

where n is the number of photons present in the cavity, c is the speed of light, V is the volume of the cavity, and $\sigma(\nu)$ (cm^2) is a narrow function centered about the absorption frequency ν_0, and is called the transition cross section. The integral of $\sigma(\nu)$ through all frequencies is defined as the transition or oscillator strength, S, Eq. 27. The transition cross section $\sigma(\nu)$, can be normalized as $g(\nu)=\sigma(\nu)/S$ and is called the line shape function. The shape of $g(\nu)$ will govern the relative magnitude of absorption, with photons of different frequencies. To obtain the total probability of

$$S = \int_0^\infty \sigma(\nu) d\nu \tag{27}$$

absorbing photons of frequency ν_0 we need to determine the number of photons involved in the absorption process. Let's construct a cylinder with area A and length L that represents a bulk section of semiconductor as in Figure 2.4. The photon flux ϕ (Number of photons/cm^2-s) of light intensity I and frequency ν_0 is given by,

$$\phi = \frac{I}{h\nu}. \tag{28}$$

The number of photons in the interaction region therefore is given by,

$$n = \phi \frac{V}{c} \tag{29}$$

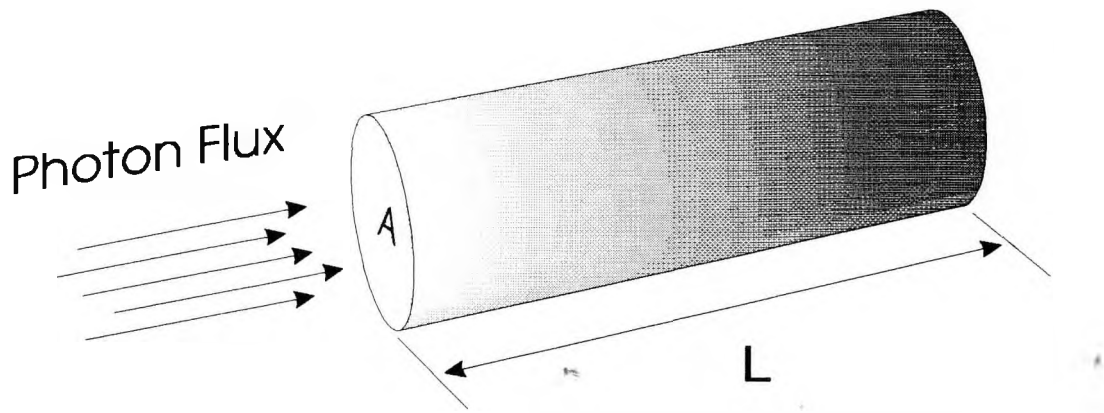

Figure 2.4 Cross section of a semiconductor under the illumination of a constant photon flux ϕ.

since the flux divided by the speed is equal to the number of photons/m^3. The total rate of absorption can now be written as $W_i = P_{ab} = \phi\ \sigma(\nu)$.

To further simplify the above equation for W_i, it is first necessary to examine the spontaneous emission of a photon into all accessible optical states. This is done so that a mathematical expression for S, the oscillator strength, can be used in the derivation of P_{ab}. The number of optical modes per unit volume, per unit bandwidth in a three dimensional optical resonator can be shown to be $M(\nu)=8\pi\nu^2/c^3$ [10]. The total probability of spontaneous emission is given by the weighted sum over all frequencies.

$$P_{sp} = \int_0^\infty [\frac{c}{V}\sigma(\nu)][VM(\nu)]d\nu = c\int_0^\infty \sigma(\nu)M(\nu)d\nu \qquad \textbf{(30)}$$

The above integral can be simplified by observing that the function $\sigma(\nu)$ behaves as a delta function around frequency ν_0 when compared with $M(\nu_0)$ so that the total probability of spontaneous emission of a photon into a specific optical mode is given by,

$$P_{sp} = M(\nu_0)cS = \frac{8\pi S}{\lambda^2}. \qquad \textbf{(31)}$$

At this point it is instructive to define the spontaneous lifetime $t_{sp}=1/P_{sp}$, so that we can obtain an analytical expression for the oscillator strength S,

$$S = \frac{\lambda^2}{8\pi t_{sp}}. \tag{32}$$

The expression obtained for S is extremely important. Under almost all circumstances a first principles derivation for S is practically impossible to calculate. The spontaneous lifetime can be experimentally determined and from that a determination of S is made using equation 32. The transition cross section $\sigma(\nu)$ can now be expressed as follows,

$$\sigma(\nu) = \frac{\lambda^2}{8\pi t_{sp}} g(\nu) \tag{33}$$

and the transition rate W_i becomes,

$$W_i(\nu)d\nu = \phi_\nu \sigma(\nu)d\nu = \phi_\nu \frac{\lambda^2}{8\pi\tau_r} g(\nu)d\nu. \tag{34}$$

2.5) Rates of Absorption

If an electron is going to be moved from the valence band E_1 to the conduction band E_2, through the absorption of a photon; the probability of an electron occupying an energy state E_1 and no electron occupying energy state at E_2 must first be determined. These probabilities will simply multiply and are given by the Fermi function, equation 35. This is called the occupation condition for absorption $f_a(\nu)$, and can be written as,

$$f_a(\nu) = [1 - f_c(E_2)]f_v(E_1)$$
$$\text{where } f_c(\nu) = f_v(\nu) = \frac{1}{[1 + \exp[\frac{(E - E_f)}{k_b T}]}. \quad (35)$$

Using the transition probability and the occupation condition derived above, the rate of photon absorption can now be calculated. Consider an incident photon flux directed into a semiconductor as in Figure 2.4. The rate of absorption (Number of photons absorbed per second per cm^3) will be given by the integral over all frequencies of the transition rate W_i multiplied by the occupation condition f_a and the optical density of states $\varrho(\nu)$. Mathematically we have the following,

$$r_{ab} = \int_0^\infty [\phi_\nu \frac{\lambda^2}{8\pi\tau_r} g(\nu)\varrho(\nu)f_a(\nu)]d\nu. \quad (36)$$

Since the line width function $g(\nu)$ is essentially a delta function at ν_0 when compared to W_i, f_a and, $\varrho(\nu)$, the above integral can be simplified to give,

$$r_{ab} = \phi_\nu \frac{\lambda^2}{8\pi\tau_r} \varrho(\nu)f_a(\nu). \quad (37)$$

The number of photons lost in an incremental length dz along the axis of the cylinder is simply the difference in rates of stimulated emission (which is the exact reverse of absorption) and absorption. Mathematically this can be represented as follows,

$$\frac{d\phi_\nu(z)}{dz} = r_{ab} - r_{st} = \frac{\lambda^2}{8\pi\tau_r} \varrho(\nu)[f_e(\nu) - f_a(\nu)]\phi_\nu(z) = \alpha(\nu)\phi(z). \quad (38)$$

Where the function f_e is simply the occupation condition for an electron under stimulated emission. Since $\varrho(\nu)$ is given by [10],

$$\varrho(\nu) = \frac{(2m_r)^{3/2}}{\pi(h/2\pi)^2}(h\nu - E_g)^{1/2}, \tag{39}$$

and, for a semiconductor in equilibrium the Fermi function $F(E_1) \approx 1$, $F(E_2) \approx 0$ the absorption coefficient for direct band-gap semiconductors $\alpha(\nu)$ can be written as,

$$\alpha(\nu) = \frac{\sqrt{2}c^2 m_r^{3/2}}{\tau_r}\frac{1}{(h\nu)^2}(h\nu - E_g)^{1/2}. \tag{40}$$

Equation 40 is plotted for GaAs, as a function of $(h\nu - E_g)$ and is illustrated in Figure 2.5 [10]. The following parameters, $\tau_r = 0.4$ ns, $m_c = 0.07m_0$, $m_v = 0.5m_0$, n=3.6 and, E_g=1.42 eV were used in the plot [10]. It is evident that the absorption coefficient $\alpha(\nu)$ undergoes a dramatic change around the band-gap energy. The results in Figure 2.5 are very similar to the experimentally observed value of $\alpha(\nu)$ which is illustrated in Figures 2.6 and 2.7 [10]. It is important to note that in designing a waveguiding structure, band to band absorption is by far the most critical parameter. A miscalculation in wavelength can cause a 10^4 error in the calculated absorption coefficient. Figure 2.6 also illustrates the losses due to other mechanisms present in GaAs. As the photon energy decreases below 0.3 eV, free carrier absorption and then phonon absorption begin to increase dramatically. If the operating wavelength is between 0.87 μm and 12 μm GaAs is relatively transparent.

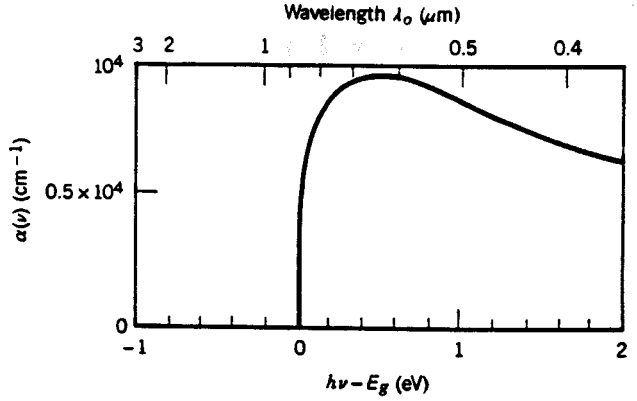

Figure 2.5 Calculated absorption coefficient for direct bandgap absorption in GaAs. After [10].

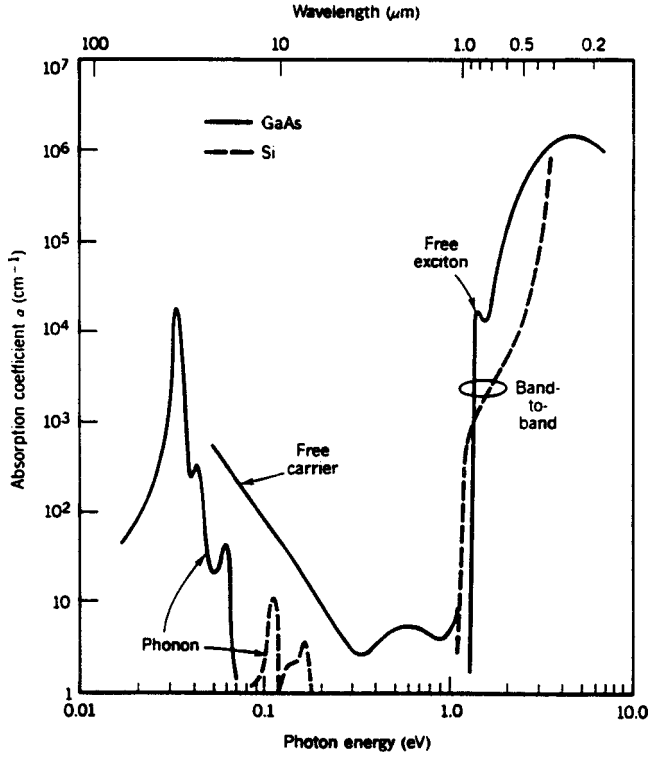

Figure 2.6 Experimentally observed absorption coefficient in GaAs. After [10].

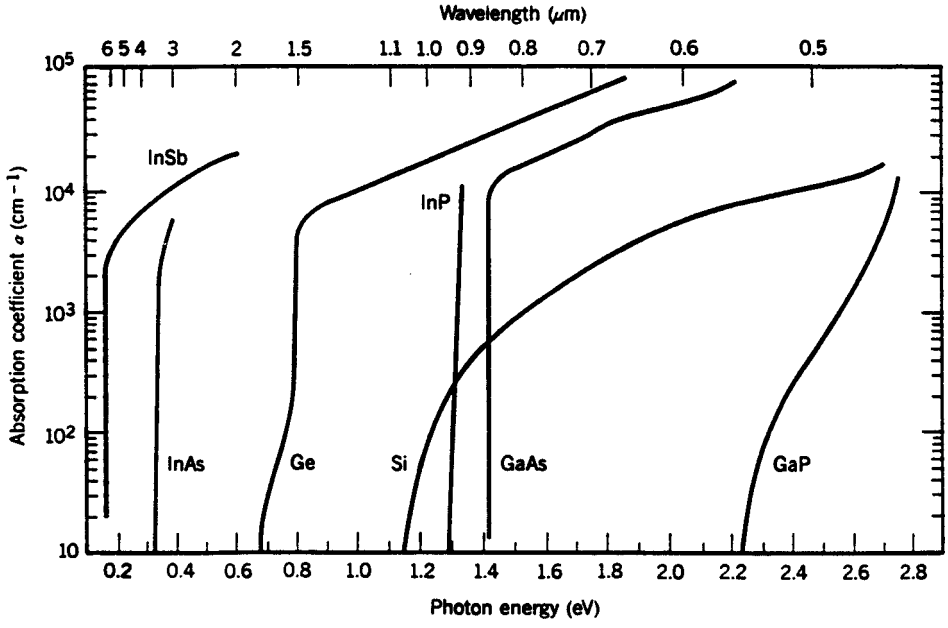

Figure 2.7 Experimentally observed absorption coefficient in GaAs and various other materials. After [10]

2.6) Structure design

The waveguiding structure for the 4x4 matrix switch, and the straight integrated waveguides/detector sections was designed such that an absorbing layer located vertically above the waveguide would tap some desired fraction of the guided optical power. An MSM detector would then be placed on top of the absorbing material so that the photocarriers can be efficiently collected. This section will present a model of a suitable single and multimode waveguide structure. The modal profile for the single mode structure will then be calculated using the transfer matrix method[4], and BPM will be used to model both the single and multimode structures. With this information, the optical power extraction in the detector sections can be determined and compared with the behaviour that was assumed in the mask design of the 4x4 switch. An improper choice of attenuation will cause an imbalance of detector absorption[5].

There are two conditions that must be satisfied to ensure proper operation of the switch. First, the operating wavelength of the laser (820 nm) must not be absorbed in the passive waveguiding region and, second it must be absorbed in the detector region. To accomplish this we have chosen the GaAs/AlGaAs material system. Since band to band absorption is the predominant loss mechanism, the concentration of aluminum for the waveguide must be chosen so that the bangap energy E_g is greater than the photon energy E_p , at 820 nm. The band-gap of $Al_x Ga_{(1-x)}As$ is given by the following empirical formula [9],

$$E_g = 1.439 + 1.042x + 0.468x^2 \qquad [eV] \tag{41}$$

where x is the percent concentration of aluminum in the material. The photon energy for a laser of wavelength 820 nm is 1.51 eV. The band-gap energy of AlGaAs using an aluminum concentration of 15% is, using equation 41, E_g=1.61 eV. The condition that $E_p < E_g$ is satisfied so that in the

---

[4] The transfer matrix method is not suitable for the analysis of multimode waveguides since the power coupled into specific modes is not known.

[5] To obtain a balanced optoelectronic switch, we require the attenuation to be approximately 3dB in 100 μm.

waveguiding region there will not be considerable band to band absorption. In the GaAs detector region the absorption coefficient $\alpha(\nu)$, as seen in Figure 2.6 is approximately $\alpha(\nu)=10000\ cm^{-1}$, which is sufficient in acting as an optical tap.

After choosing a waveguiding region of 15% aluminum composition, the waveguide thickness must be determined. To determine the waveguide depth it is necessary to solve the proposed structures using the Beam Propagation Method and transfer methods as described above. The following two structures were selected for growth,

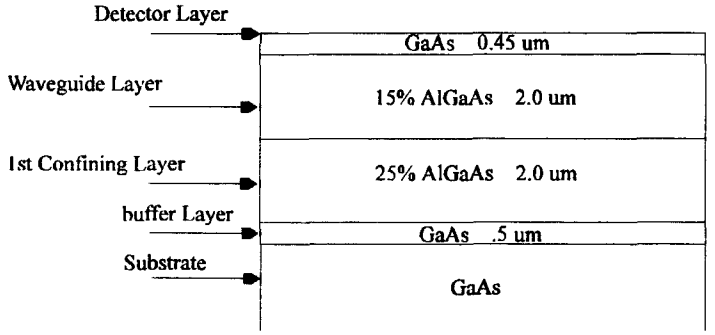

Wafer #94-093 Multimode Waveguide/Detector

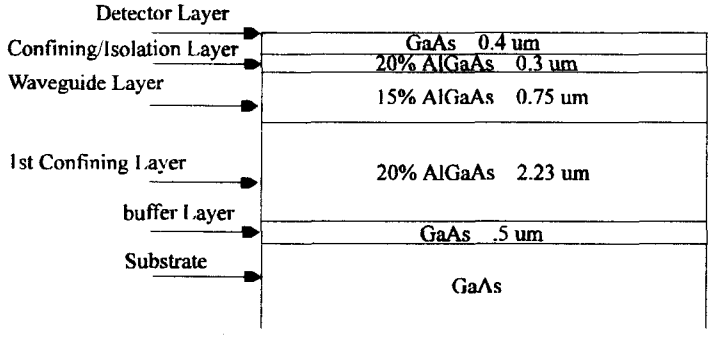

Wafer #94-095 Singlemode Waveguide/Detector

Figure 2.8 Multimode and single mode waveguide-detector thicknesses and material composition.

Figure 2.8 illustrates each layer with a brief description of their growth purpose. Essentially the waveguiding region must be chosen such that the index of refraction of the centre layer is higher

than that of both confining layers. Buffer layers are added to reduce the amount of coupling between the waveguiding and detector regions and to ensure smooth growth transitions between GaAs and AlGaAs layers.

The single mode structure was examined first. Assuming a proposed 0.25 μm ridge etch depth the effective index method was used to determine the confinement in the lateral direction. For a quarter micron etch depth two confined mode solutions were found in the horizontal direction. The confinement factor for the fundamental mode was found to be 87%. From this we can infer that a quarter micron etch depth is sufficient in obtaining a low loss ridge waveguide. The structure was also analyzed as a planar waveguide given in Figure 2.8. The modal solution is plotted in Figure 2.9.

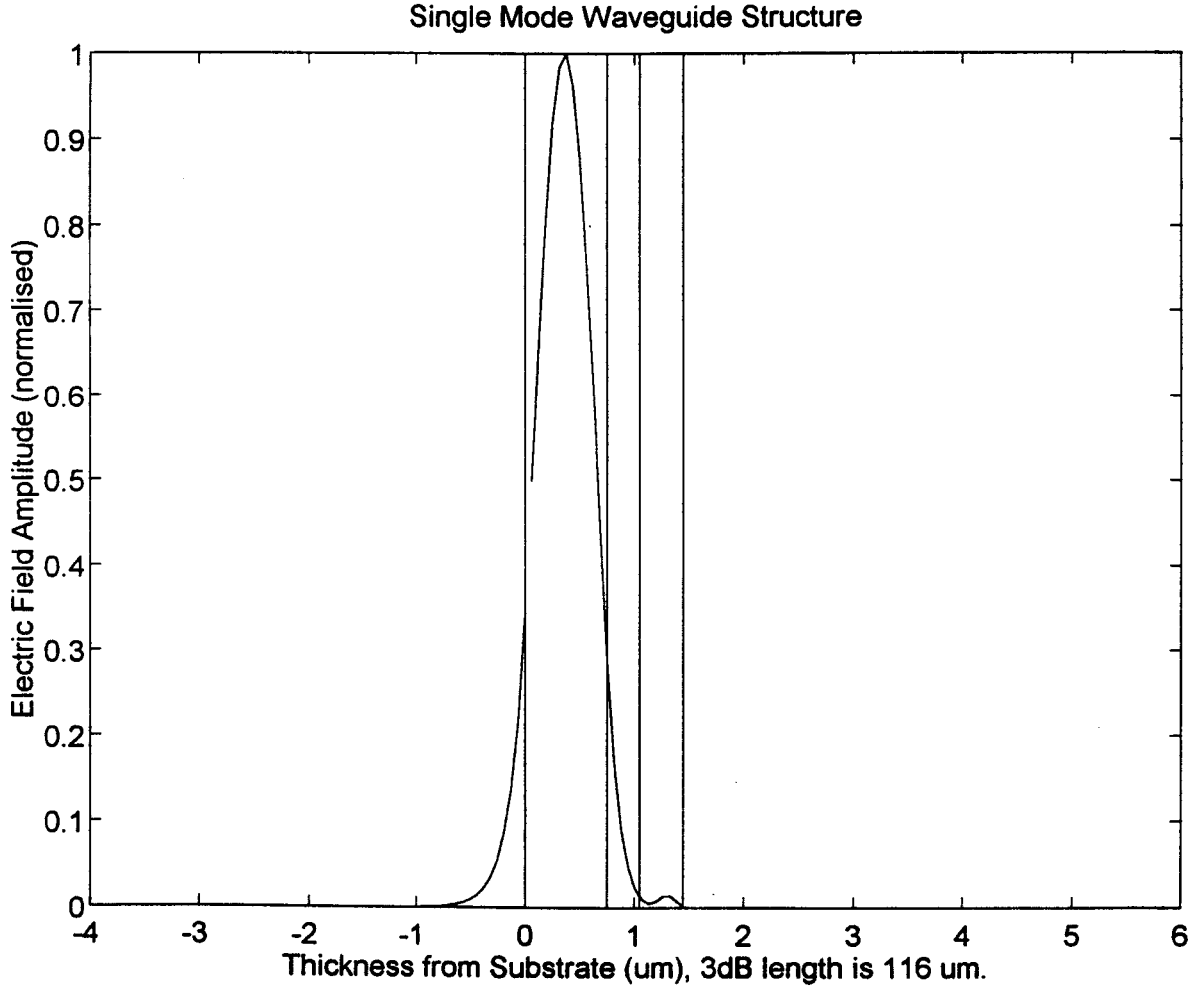

Figure 2.9 Modal field distribution of the single mode waveguide structure.

Figure 2.9 illustrates that the optical power does not penetrate substantially into the absorbing substrate and, more importantly, the power is mostly confined to the waveguide. The detector region has just enough power coupled into it so that this structure has an effective 3dB attenuation of approximately 116 μm. This is consistent with the absorption coefficient derived in the previous section, since the optical power is confined only fractionally (calculated coupling to GaAs was approximately 0.0059) to the GaAs, the attenuation coefficient will be a fraction of the incident optical power. Mathematically, the apparent absorption coefficient in the detector region $\alpha_{app} = \Gamma \alpha_{GaAs}$, where Γ is the confinement factor of the optical mode.

As a first guess, planar waveguides solutions are important, but the beam propagation method is much more accurate at determining losses in three dimensional structures. The single mode structure of Figure 2.8 was solved for a 10 micron wide and 0.25 micron deep ridge waveguide. The optical power attenuation was obtained and is plotted in Figure 2.10. The 3dB power loss with this method was found to be 118 μm. This is in excellent agreement with the 3dB length obtained with the matrix transfer method above. In general, the objective was not to determine an exact attenuation coefficient but, to obtain a waveguiding structure that would be close to the 100 μm 3dB length used in the mask design. If the attenuation is not close to the absorption assumed in calculating the detector lengths the switch will not be balanced.

The multimode structure was also modeled using the beam propagation method. The attenuation of power in the detector regions is plotted in Figure 2.11. Here we obtain a 3dB length of approximately 92 μm. This again is fairly close to the required 100 μm 3dB length.

After the design and modelling of the single and multimode structures was completed, the structure designs were sent to the Communication Research Centre for growth. Hall effect measurements were performed and an intrinsic background doping of approximately $1x10^{15}$ donors/cm^{-3} was determined. The two wafers were then processed according to the fabrication procedures specified in appendix 1.

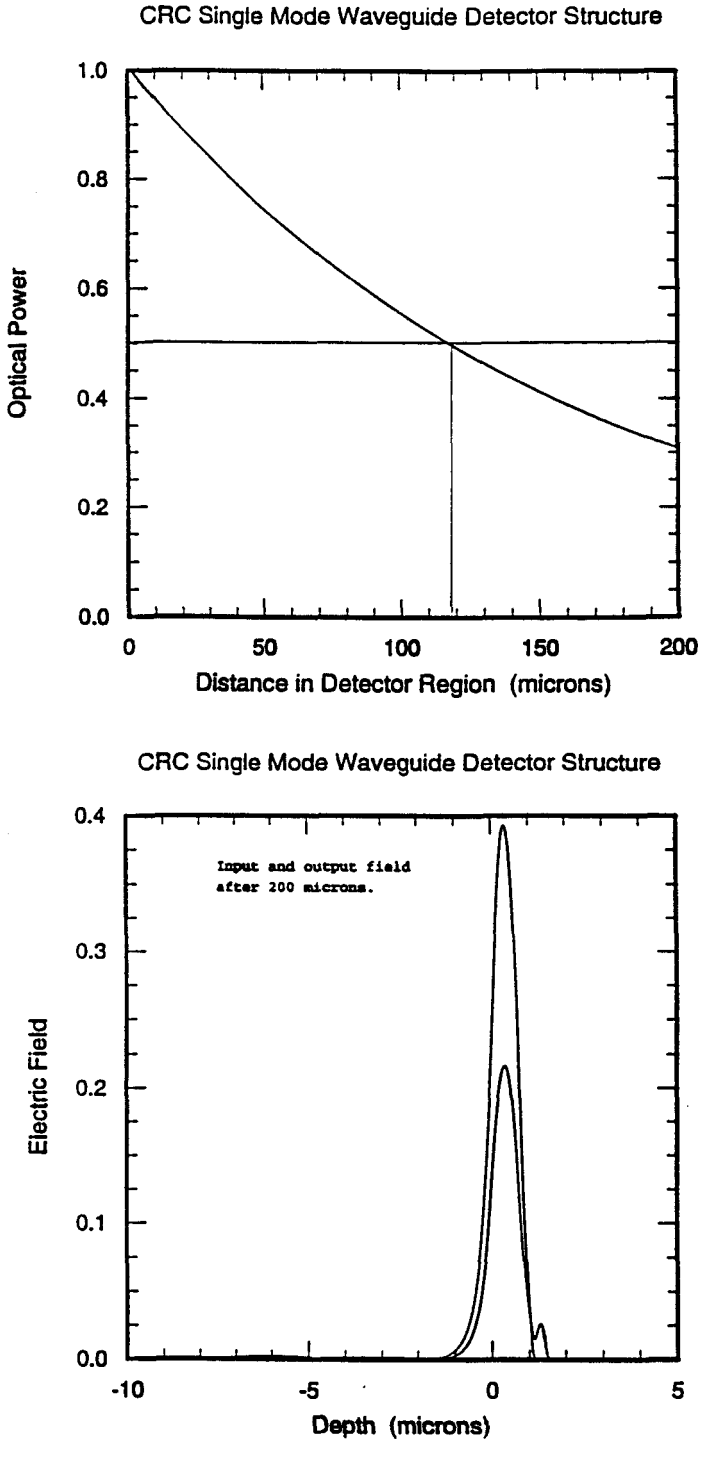

Figure 2.10 Optical power attenuation of the single mode waveguide structure using the Beam Propagation Method, BPM.

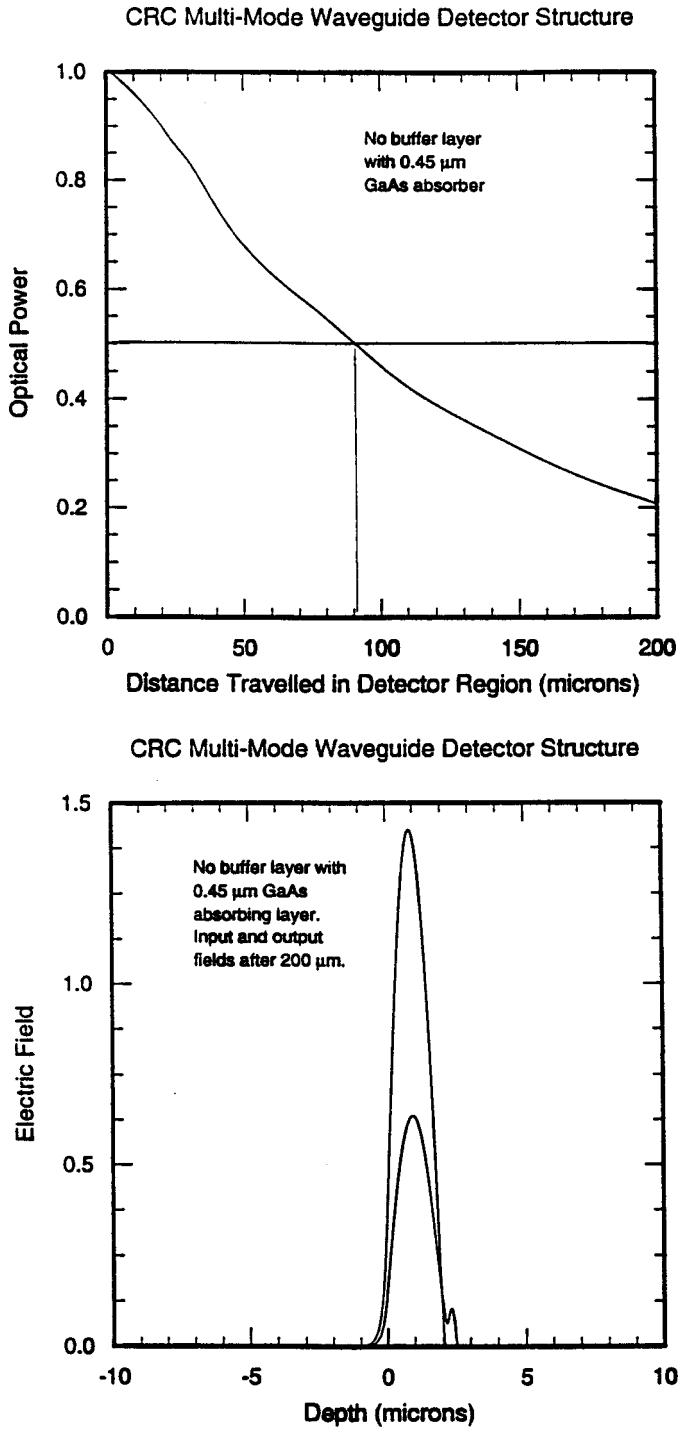

Figure 2.11 Optical power attenuation of the multimode waveguide structure using the Beam Propagation Method, BPM.

Chapter 3: Detector Theory

3.1) Introduction:

It is a well established fact, that semiconductor photon detectors play an important role in the integration of optoelectronic devices [10]. This chapter will begin with a general introduction into semiconductor photodetectors. The difference between photoconductors and photodiodes will be analyzed, and properties such as quantum efficiency, responsivity, gain, and noise will all be discussed. The change in conductivity, due to the absorption of photons, in photoconductors will then be derived along with the current transport of a one dimensional MSM. Using the one dimensional model, current vs. voltage relations will be generated and a comparison will be made with experimental observations.

3.2) General Detector Properties:

Chapter Two presented an in depth view of the physical processes underlying photon absorption in semiconductors, but it did not discuss how the conductivity, or other physical quantities, of the material change with the generation of electron-hole pairs. Since, in most applications, we are concerned with the changes of physical quantities such as current, a mathematical relation must be established relating the incident photon flux to the observed photocurrent. This is done by first examining the statistical aspects of electron hole creation in semiconductors.

It was previously demonstrated that photons incident on a semiconductor can be either scattered, absorbed, or reflected. When a photon is absorbed by a semiconductor, the probability that the created electron-hole pair successfully contributes to photodetector current is defined as the internal quantum efficiency ζ, $0 \leq \zeta \leq 1$. For a general photodetector, the external quantum

efficiency η, can be expressed as,

$$\eta = (1 - R)\zeta[1-\exp(-\alpha d)] \tag{1}$$

where the first term is simply the transmitted optical power at the surface of the detector, and is a function of the index of refraction of the medium [11]. The last term, [1-exp(-αd)], is simply the fraction of photon flux which is absorbed by the semiconductor in the detector length d. This is consistent with the different types of photon absorption discussed in Chapter Two; α the total absorption coefficient accounts for the fraction of photons which are absorbed by the material, and ζ is the probability that the created electron-hole pair successfully contributes to the electric current in an external circuit. Using this result the responsivity of a photodetector can now be determined.

The responsivity of a photodetector is simply the ratio of the photocurrent to the incident photon flux ϕ. For low photon intensities, this proportionality constant is linear. Therefore, if a semiconductor is irradiated with an incident optical power of $P=h\nu\phi$ (watts), and for every absorbed photon a charge e is generated in the external circuit, (Ramo's Theorem) [10] the current can be expressed as,

$$i_p = e\phi = \frac{eP}{h\nu}. \tag{2}$$

Since not all absorbed photons contribute to photocurrent (see above), equation 2 must be multiplied by the quantum efficiency, thereby obtaining,

$$i_p = \frac{\eta q P}{h\nu} = RP, \tag{3}$$

The responsivity, R can be rewritten as,

$$R = \frac{\eta q}{h\nu} = \eta \frac{\lambda_0}{1.24}, \text{ where } \lambda_0 \text{ is the wavelength in microns .} \tag{4}$$

Because semiconductor photon detectors produce charges q in the external circuit, which are different than e, equations 3 and 4 can be restated, in a more general form, to include detector gain. The number of electron-hole pairs produced must be an integral number of e charges, so the gain G, can be expressed as G = q / e, and equations three and four are restated as,

$$i_p = \frac{G\eta eP}{h\nu} = RP, \tag{5}$$

where the responsivity R is now,

$$R = G\eta \frac{\lambda_0}{1.24} \tag{6}$$

The expression obtained for the current in equation five must be understood from a statistical point of view. Because photons arrive in a random fashion, the current in equation five must be interpreted as the average current measured by the detector. Noise in photoconductors comes in a variety of different forms, essentially all processes which lead to quantum events, cause fluctuation in the measured current. For example, there are two major types of detector noise which cause the current to fluctuate about its average value. The first and most obvious is that photons do not arrive in linear streams but are spread out in a random fashion[1] so their arrival times are considered statistical events. This causes the creation of carriers to be statistical which directly affects the linearity of the measured current. Secondly, because the quantum efficiency is itself a probabilistic interpretation of carrier transport, the current will also fluctuate due recombination and generation noise.

3.3) Photodetectors:

Semiconductor photodetectors can be divided into two major classes, photoconductors and photodiodes. Section 3.3A will derive the change in conductivity of a photoconductor that is

---

[1] The distribution of photons is typically represented as a Poisson distribution.

illuminated by a discrete laser source at wavelength λ_0, and section 3.3B will derive the current transport equations for a one dimensional MSM photodiode. Because our devices showed characteristics of both photoconductors and photodiodes, a review of both types of photon detectors is necessary.

3.3A) Photoconductors:

A photoconductor is a semiconductor material in which generated photo-carriers are collected with ohmic contacts. An absorbed photon flux will therefore increases the conductivity of the material. The contacts can be placed either on top, or at the ends of the semiconductor, as illustrated in Figure 3.1. When the semiconductor material is illuminated with an incident photon flux Φ, electron-hole pairs will be produced, at a pair production rate per unit volume, R_{eh} given by,

$$R_{eh} = \frac{\eta \Phi}{wA}. \tag{7}$$

From simple recombination-generation rate theory, the rate at which electrons recombine with holes[2] is given as $\Delta n/\tau$. Under steady state conditions the generation rate must equal the recombination rate so that the number of photogenerated electrons Δn is expressed as,

$$\Delta n = \frac{\eta \tau \Phi}{wA}. \tag{8}$$

Equation 8 gives us the change in carrier concentration from its equilibrium value. The change in carrier concentration, can be related to a change in conductivity by using the following relation,

$$\Delta \sigma = e \Delta n (\mu_e + \mu_h) = \frac{e \eta \tau (\mu_e + \mu_h)}{wA} \Phi. \tag{9}$$

---

[2] This assumes that the incident photon flux does not cause any degeneracies or non-linearities..

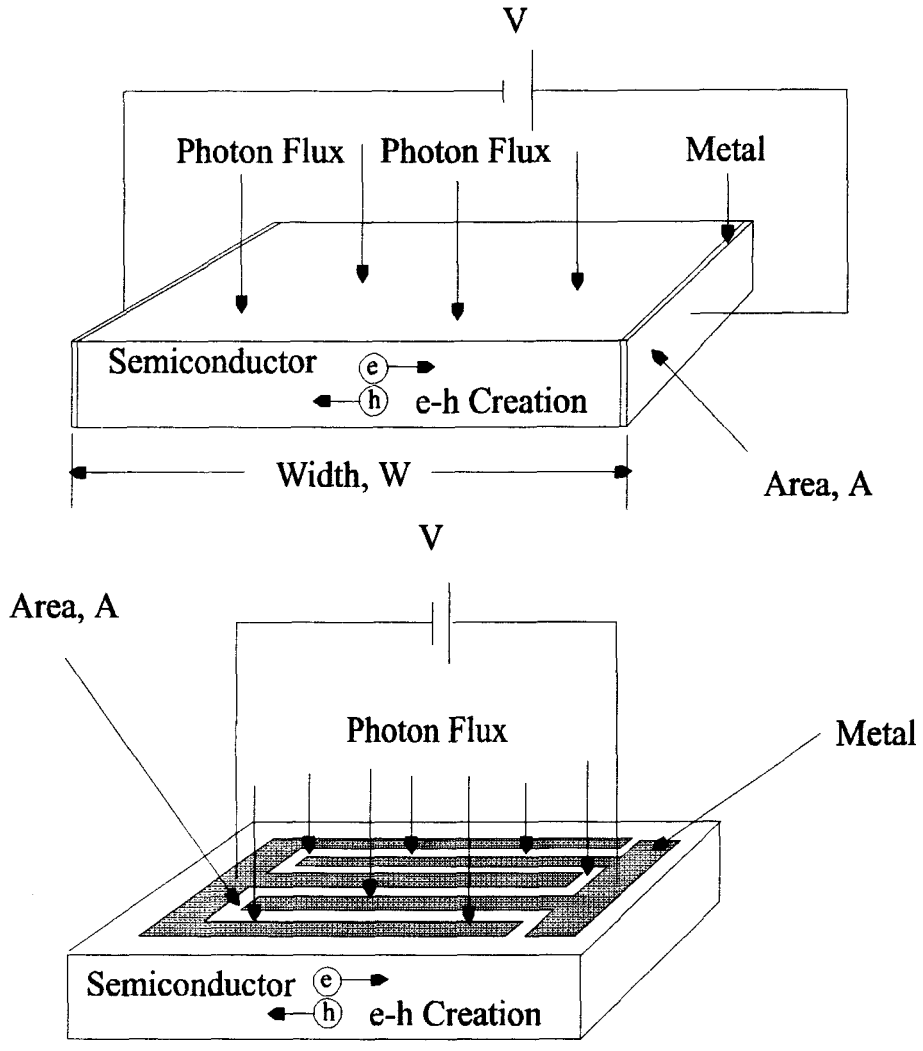

Figure 3.1 Two different metal deposition geometries on a semiconductor photodetector..

In practical applications the conductivity is rarely measured directly, but the current is readily obtained, by using, $J=\sigma E$ and $v_e = \mu_e E$ and restating equation 9 to obtain,

$$i_{ph} = \frac{e\eta\tau(v_e+v_h)}{w}\Phi \qquad \textbf{(10)}$$

There are two important points concerning equation 10 which are worth noting. The first, is that

the current is directly proportional to the incident photon flux, which is consistent with the previous results obtained in equation 8. Secondly by comparing equation ten and equation six, the photoconductive gain G, can be expressed as,

$$G = \frac{\tau(v_e+v_h)}{W}. \qquad (11)$$

The gain arises because the recombination lifetime τ is generally different than the carrier transit times. The gain in semiconductor photoconductors can range anywhere from 1 to 10^6 [10], depending on the excess carrier lifetimes. The carrier transit time[3] is also a very important factor in determining the detector speed, one would want to minimize the transit time spread as much as possible[4], while keeping the capacitance the same. This creates a delicate balance between the gain achieved in a photoconductor and the speed of the detectors.

3.3B) Photodiodes:

A photodiode, unlike a photoconductor, collects the photogenerated carriers in a depletion region. Photodiodes normally have very low dark currents, and tend to be extremely fast since high electric fields quickly sweep out photo-generated carriers. A reversed bias p-n junction, p-i-n junctions, and Schottky barrier MSM's are typical examples of photodiodes. In the case of p-n or p-i-n diodes the reverse bias current isn't very high and therefore, when an optical signal is injected into the device, there is a dramatic increase in current. MSM's also have very low dark currents but unlike p-n junctions, MSMs have back to back diodes operating simultaneously. When a bias is applied to the device, one diode will be forward biased and one diode will be reverse biased. Because the resistance of the reverse biased diode is typically much greater than that of the forward biased diode, most of the applied potential is dropped across the reverse

---

[3] Another important property which limits device speed is the RC time constant. This will be a function of both device geometry and experimental setup.

[4] Minimizing the transit time spread is important, but knowledge concerning the capacitance must also be noted since by changing the geometry you can increase the capacitance which slows the device down. The capacitance and transit time spread are competing effects.

biased contact thereby obtaining very low dark currents. Since we are solely concerned with the operation of MSM's, this section will first look at some essential properties of a metal semiconductor contact, and then develop a one dimensional current model for a metal semiconductor metal contact.

3.3C) Metal Semiconductor Contact:

The deposition of metal on a semiconductor can result in the formation of two very different types of contacts. If before contact between the semiconductor and metal is made, the Fermi energy in the metal is greater than the Fermi energy of the semiconductor, the resulting contact is ohmic for an n-type semiconductor[5]. This occurs because the electrons do not have to overcome any potential barriers in moving from the semiconductor to the metal. When the Fermi energy of the semiconductor is greater than the Fermi energy of the metal before contact, the junction is called a Schottky contact. In this case there is now a potential barrier which must be overcome by the electrons. Around 1938 Schottky suggested that for rectifying contacts, the potential barrier arises due to the formation of stable space charge regions [12].

For MSM photodetectors, a Schottky contact is desirable to obtain photodiode responses. To understand how the stable space charge region is formed it is necessary to refer to the energy band diagram of a metal and n-type semiconductor initially infinitely separated, as in Figure 3.2.

[5] For a p-type semiconductor, under the same conditions, the contact would be rectifying, like a p-n junction.

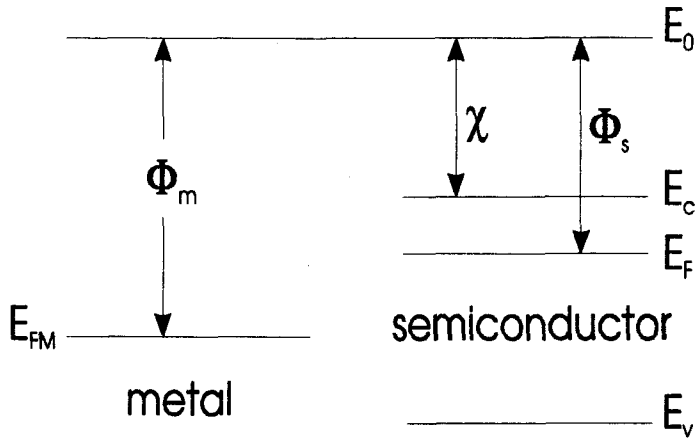

Figure 3.2 Energy band diagram of a an infinitely separated metal and semiconductor.

The work function of the metal Φ_M , is defined as the energy required to move an electron from the Fermi level in the metal, E_{FM}, to the vacuum energy level E_0. The work function of the semiconductor is similarly defined as the energy required to move an electron from the Fermi level E_{FS}, to the vacuum energy E_0. But, for a semiconductor, normally there are no electron states at $E=E_{FS}$, the electron states are at the conduction band energy $E=E_c$ or higher. Therefore, for semiconductors the electron affinity χ is also defined. The electron affinity is simply the difference in vacuum energy E_0 and the conduction band energy E_c. Mathematically we have the following equations,

$$\Phi_S = \chi + (E_c - E_{FS})_{Bulk} \tag{12}$$

$$\Phi_M = E_0 - E_{FM} \tag{13}$$

where χ is,

$$\chi = (E_0 - E_c). \tag{14}$$

Figure 3.3 illustrates how the energy band diagram of a metal semiconductor interface changes when the materials are brought into intimate contact. Because electrons in the semiconductor have higher energies than electrons in the metal, when the materials are brought into contact, electrons in the n-type semiconductor will diffuse into the metal[6]. Since charge must be conserved, electrons leaving the semiconductor will leave behind positive donors, and will pile up as a sheet charge σ on the metal[7]. The diffusion of electrons into the metal cannot proceed indefinitely, eventually the potential barrier will be large enough to prevent more electrons from diffusing from the semiconductor into the metal. Physically this barrier arises because, before the materials are combined the Fermi level in the semiconductor is higher than the Fermi level in the metal. As was previously stated for an n-type semiconductor, when $\Phi_M > \Phi_S$ the metal-semiconductor contact is called a Schottky barrier (When $\Phi_M < \Phi_S$ you obtain an ohmic contact.).

To understand this mathematically we once again refer to Figure 3.3, which illustrates the energy band diagram of a metal semiconductor interface under thermal equilibrium conditions. Conservation of charge demands that the charge sheet formed in the metal must be equal to the charge formed in the depletion region of the semiconductor, $Q_s = q\, N_d\, x_n$. Poisson's equation in the semiconductor depletion region can be written as,

$$E(x) = \frac{1}{K_s \epsilon_0} \int q N_d^+ dx = \frac{q N_d x}{K_s \epsilon_0} + A \tag{15}$$

Where N_d is the doping of the semiconductor, K_s is the dielectric constant, and A is a constant of integration. Using the boundary condition that the electric field at the edge of the depletion region $x=x_n$ be equal

---

[6] The diffusion process is similar to that of a P^+N junction.

[7] This is only true for ideal Schottky contacts, and does not include any surface state effects which can destroy the charge barrier region. [12]

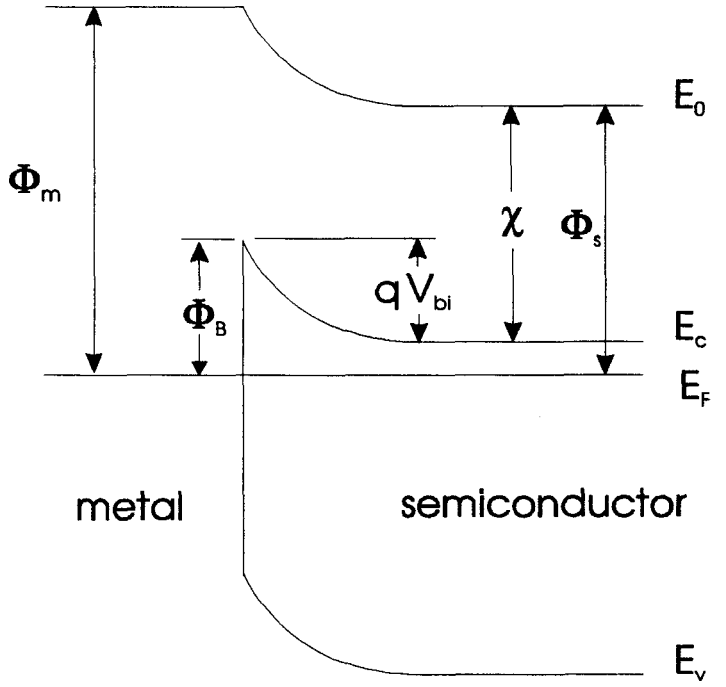

Figure 3.3 Metal semiconductor junction under thermal equilibrium conditions.

to zero, equation 15 can be solved for E(x) to obtain,

$$E(x) = -\frac{qN_d}{K_s\epsilon_0}(x_n - x) \tag{16}$$

Before obtaining the potential in the depletion region, the built in potential V_{bi} for electrons going from the semiconductor to the metal must first be determined. The energy barrier that electrons must overcome in going from the metal to the semiconductor is given by the difference in the two work functions, $qV_{bi} = \Phi_M - \Phi_S$. Substituting equation twelve for Φ_S we obtain,

$$qV_{bi} = \Phi_M - \chi - (E_c - E_f)_{bulk} \tag{17}$$

The potential distribution in the semiconductor can be obtained by once again employing Poisson's equation,

$$V(x) = -\int E(x)dx + A_2. \tag{18}$$

Using equation 16, and the boundary condition $V(x_n)=V_{bi}$, the potential V(x) is written as,

$$V(x) = V_{bi} - \frac{qN_d}{2K_s\epsilon_0}(x_n - x)^2 \tag{19}$$

Equation 19 can be used to obtain the width of the depletion region by noting that the potential at x=0, the boundary interface, equals zero. Solving for x_n we obtain,

$$x_n = \sqrt{\frac{2V_{bi}K_s\epsilon_0}{qN_d}}. \tag{20}$$

An interesting consequence of equation 20 is that, to a first approximation, it can be used to obtain the capacitance of the metal semiconductor junction. Because a one dimensional metal semiconductor junction behaves as a parallel plate capacitor[8], the capacitance can be given by, $C=[K_s \epsilon_0 A]/ x_n$. By estimating the capacitance into a 50 ohm load, the RC time constant of the M-S contact can be determined. This in turn will give information on how fast the device can operate, assuming the device speed is not limited by the carrier transit times.

Using equation 17 and substituting into equation 20 we can obtain the length of the depletion region as a function of known semiconductor and metal parameters. The charge balance condition, electric field and potential are illustrated in Figure 3.4.

When the metal semiconductor interface is biased, the width of the depletion region will change, as is the case with p-n junctions. The barrier V_{bi} will either increase or decrease, depending on the sign of the applied bias. To account for this, the barrier V_{bi} in equation 20 is changed to $q(V_{bi} - V_a)$ where V_a is the applied voltage. Equation 20 then becomes,

---

[8] This is only true for one dimensional devices, the capacitance for a planar MSM is given by Chin et al. [18].

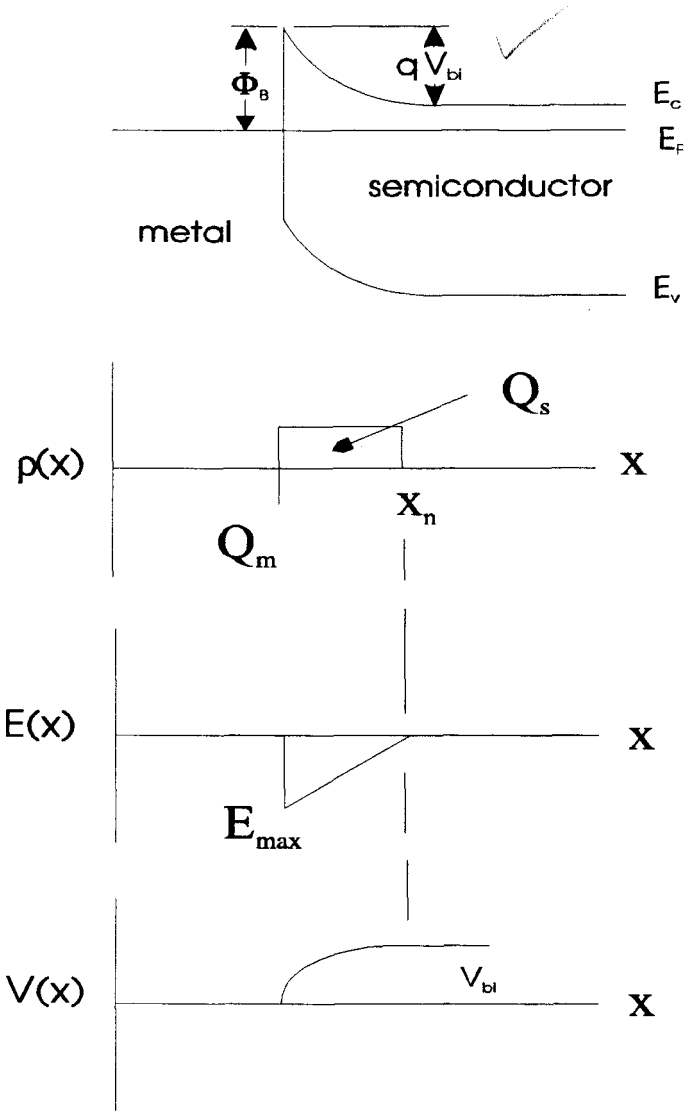

Figure 3.4 Charge density, electric field and potential distribution of a metal semiconductor contact at equilibrium.

$$x_n = \sqrt{\frac{2K_s\epsilon_0}{qN_d}(V_{bi}-V_a)}. \tag{21}$$

An important result of metal-semiconductor contacts is that the potential barrier on the metal side, $\Phi_{b,}$ is independent of bias. This implies that (under normal applied biases) the reverse bias current is independent of applied bias.

As a final refinement to the above model, we must include the image charge lowering of the potential barrier. This is done by examining the force, or potential, induced on an electron at a distance x from the metal. The image force lowering is based on a well established fact that when an electron is at a distance x from a metal, the metal will induce a positive force of attraction on the electron which is equivalent to placing a positive charge at -x [12]. The force of attraction between the metal and the electron is called the image force, or Schottky effect[9], and is given by [12],

$$F = \frac{-q^2}{4\pi(2x)^2\epsilon_0}. \tag{22}$$

Using equation 22 one can calculate the potential associated with the applied force, called the image charge potential. By summing any external potentials already present, the total potential in the vicinity of the metal can be obtained. (See Figure 3.5 [12]). Mathematically we obtain,

$$PE(x) = \frac{q^2}{16\pi\epsilon_0 x} + qEx, \tag{23}$$

[9] This effect is extremely interesting because it is only present when an electron is in the vicinity of the metal and is not a permanent effect.

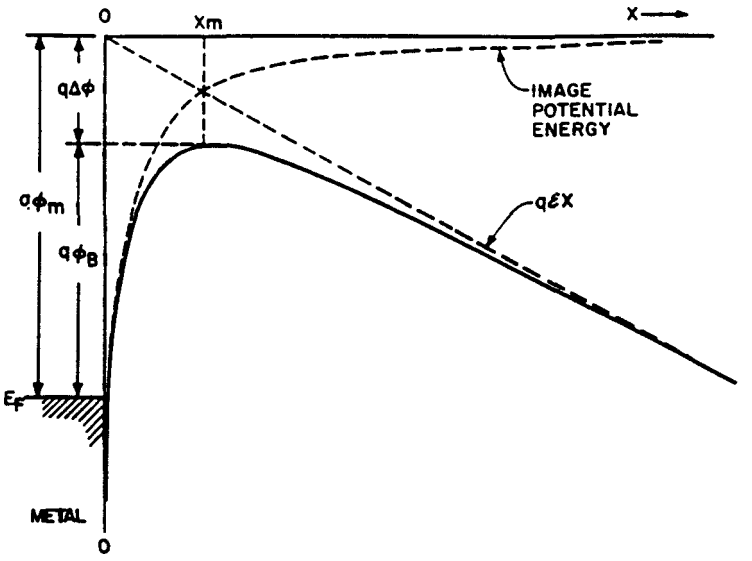

Figure 3.5 Energy band diagram between a metal surface and a vacuum. After [12].

The condition where the slope of the potential equals zero d[PE(x)]/dx =0 is now the new equilibrium position of the barrier [12]. Taking the derivative of equation 23 and setting it equal to zero we obtain the energy lowering $\Delta\phi$, and the location of the lowering x_m [12],

$$x_m = \sqrt{\frac{q}{16\,\pi\,\epsilon_0 E}} \qquad cm \tag{24}$$

$$\Delta\Phi = \sqrt{\frac{qE}{4\,\pi\,\epsilon_0}} = 2Ex_m \qquad V. \tag{25}$$

Typically, the higher the electric field the greater the energy barrier lowering. At high fields this effect can become quite pronounced.

The above analysis can be extended to metal-semiconductor (M-S) interfaces, by replacing the electric field with the maximum field at the interface and changing ϵ_0 to $\epsilon_s = \epsilon_0\,\epsilon_r$. For a semiconductor, where $\epsilon_s = 12\,\epsilon_0$ and the electric field is approximately 10^5 V/cm. The image

charge lowering is 0.035 V [12]. This effect might seem negligible but is in fact very important when considering carrier transport across the M-S junction.

3.3D) Thermionic Emission Theory:

To obtain the electric current for a one dimensional MSM detector, the current across a M-S junction must first be determined. There are a number of theories which adequately describe the transport of carriers across the M-S junction. Because GaAs is a high mobility semiconductor, thermionic emission theory will be used[10]. Thermionic emission theory [12] is derived using the basic premises that the barrier height $q\Phi_b$ is much larger than kT, thermal equilibrium prevails at the point of electron emission, and current flowing in the device does not destroy this equilibrium [12]. These assumptions allow for the superposition of both electron fluxes. Therefore the total current is simply the sum of the current flowing from the semiconductor to the metal and the current flowing from the metal to the semiconductor $J_{s\to m} + J_{m\to s}$.

It is obvious that the current flow in the metal semiconductor contact will only be a function of barrier height. Unlike a p-n junction, the current in a metal semiconductor junction flows due to the transport of majority carriers. Since we are dealing with an n-type GaAs sample, the electrons can either jump over the barrier V_{bi}, tunnel through this barrier, or recombine with a hole. These processes are illustrated in Figure 3.6 [12].

For an electron to overcome the potential barrier V_{bi} and contribute to the current, the electrons must have an energy greater than $E_f+q\Phi_b$. The current from the semiconductor to the metal $J_{s\to m}$ can be obtained by summing all electrons with energies greater than $E_f+q\Phi_b$, therefore $J_{s\to m}$ is obtained as follows,

$$J_{s\text{-}m} = \int_{E_F+q\Phi_B}^{\infty} q v_x dn, \qquad (26)$$

[10] For further information the writer refers to Sze [12] chapter 5.

where v_x is the electron velocity from the metal to semiconductor, dn is the electron density in an incremental energy interval dE which is given by,

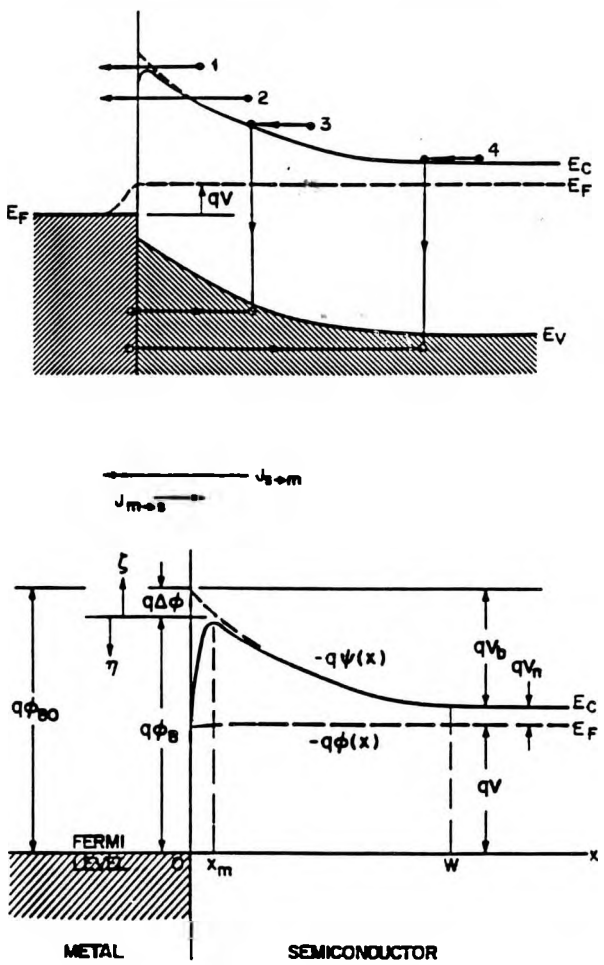

Figure 3.6 Current transport processes across a M-S contact. After [12]

$$dn = N(E)F(E)dE \tag{27}$$

and the electron density of states N(E) and the Fermi function F(E) are well known functions for semiconductors. N(E) and F(E) can be substituted into equation 27 obtaining,

$$dn = 2\left(\frac{m_*}{h}\right)^3 \exp\left(-\frac{qV_n}{kT}\right) \exp\left(-\frac{m^* v^2}{2kT}\right) (4\pi v^2 dv), \tag{28}$$

where $qV_n = E_c - E_f$. Equation 28 is simply the number of electrons distributed over their three dimensional velocity vector v. Since we are only interested in the velocity component in the x direction when integrating equation 26 both v_y and v_z integrations must extend from zero to infinity. Substituting equation 28 into 26 and transforming the integral from energy to velocity, the current obtained $J_{s\to m}$ is,

$$J_{sm} = [\frac{4\pi q m^* k^2}{h^3}] T^2 \exp(-\frac{qV_n}{kT}) \exp(-\frac{m^* v_{ox}^2}{2kT}). \tag{29}$$

For an electron to overcome the potential barrier in the x direction, the kinetic energy must be at least equal to the potential barrier V_{bi} . Mathematically,

$$\frac{1}{2} m^* v_{ox}^2 = q(V_{bi} - V) \tag{30}$$

where V is the applied voltage, and equation 29 can be restated as,

$$J_{sm} = A^* T^2 \exp(-\frac{q\Phi_b}{kT}) \exp(\frac{qV}{kT}). \tag{31}$$

where A* is called Richardson constant for electron thermionic emission.

$$A^* = [\frac{4\pi q m^* k^2}{h^3}] \tag{32}$$

Because the electron current from the metal to the semiconductor $J_{m\to s}$ is not a function of applied bias, the potential, in equation 31, can be set to zero. Under thermal equilibrium conditions the total current flowing at the junction interface is zero, so that the current density $J_{m\to s}$ can be written as,

$$J_{ms} = -A^{*}T^{2}\exp\left(-\frac{q\Phi_b}{kT}\right). \tag{33}$$

The total current flowing in a metal semiconductor interface can now be expressed as a sum of $J_{s\to m} + J_{m\to s}$ and is given by,

$$J_n = A^{*}T^{2}\exp\left(-\frac{q\Phi_b}{kT}\right)\left[\exp\left(\frac{qV}{kT}\right)-1\right]. \tag{34}$$

Equation 34 is used to obtain the current flowing in a metal semiconductor interface as a function of applied voltage. Since a metal-semiconductor-metal detector is basically two back to back metal semiconductor contacts, equation 34 will be instrumental in obtaining the current in a metal semiconductor metal contact.

3.3E) One Dimensional Metal-Semiconductor-Metal Contacts (MSM):

Figure 3.7 [13] illustrates the energy band diagram for an MSM contact under thermal equilibrium. With no applied bias the net electron and hole current at contacts one and two is equal to zero. Under applied bias one contact will be forward biased and one contact will be reverse biased. When a negative potential is applied to contact number one, the energy band diagram is obtained by pulling the Fermi level at contact one up and pulling the Fermi level of contact two down. The differences in Fermi levels must equal the applied voltage. This is illustrated in Figure 3.8 [13]. The applied potential is dropped across the regions of most resistance (the two depletion regions), and is zero in charge neutral semiconductor.

The operation of the MSM can be divided into three separate physical states. When the applied voltage V_a is such that the sum of the two depletion regions, given by equation 20, is

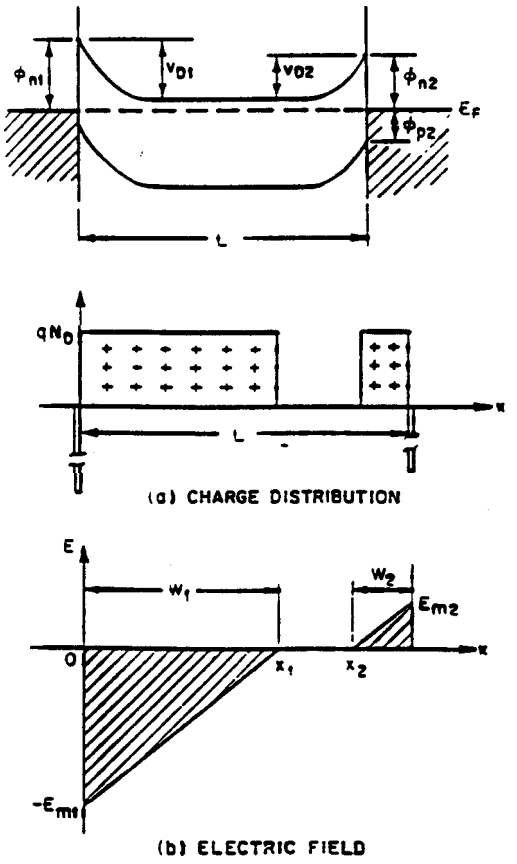

Figure 3.7 Energy band diagram of an MSM under no external bias. After [13].

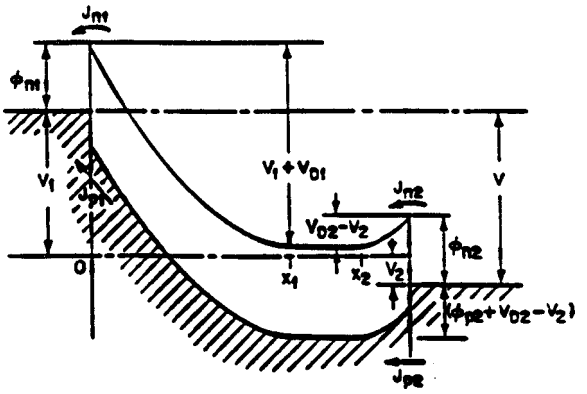

Figure 3.8 Energy band diagram of an MSM under bias. After [13].

smaller than the width of the MSM, the device is operating under small voltage conditions. When the sum of the depletion widths equals the width of the MSM, l, that voltage is designated the reach through voltage, V_{rt}, of the detector and is typically the voltage range where the photodetector would be operating, since the detector is entirely depleted of carriers. When the applied voltage causes the electric field to become flat (V_{fb}) at x=l, the hole barrier (Φ_b) has been reduced to its smallest value. Any voltages above reach through are not interesting in detector applications of MSM's since the minority hole current can increase to many orders of magnitude greater than the majority electron current [13].

In this model, the operating voltage range will be chosen as five volts, since this was determined as the experimental voltage before breakdown occurred. Using equation 34 the reverse bias current density at contact one ,see Figure 3.8, is given as [12],

$$J_{n1} = A^{*}T^{2}\exp\left(-\frac{q\Phi_b}{kT}\right)\exp\left(\frac{q\Delta\Phi_{n1}}{kT}\right)\left[1-\exp\left(\frac{-qV_1}{kT}\right)\right] \qquad (35)$$

where $V=V_1+V_2$,is yet to be determined. Similarly, using equation 34, the forward bias current density at contact two is given by,

$$J_{n2} = A^{*}T^{2}\exp\left(-\frac{q\Phi_b}{kT}\right)\exp\left(\frac{q\Delta\Phi_{n1}}{kT}\right)\left[\exp\left(\frac{-qV_2}{kT}\right)-1\right]. \qquad (36)$$

To determine the voltage dropped at each metal semiconductor interface, V_1 and V_2, we enforce continuity of current, requiring $J_{n1}=J_{n2}$. For a symmetrical MSM structure this becomes [12],

$$\left[\frac{q^{3}N_d}{8\pi^{2}\epsilon_s^{3}}\right]^{1/4}\left[(V_1+V_d)^{1/4}-(V_d-V_2)^{1/4}\right] = \frac{kT}{q}\ln\left[-\frac{e^{\beta V_2}-1}{1-e^{-\beta V_1}}\right] \qquad (37)$$

Equation 37 with the condition $V=V_1+V_2$ can be numerically solved to obtain V_1 and V_2.

In determining V_1 and V_2 equation 37 was set equal to a function $F(V_1)$ which was then plotted on the real axis from 0 to 5 volts. Solving equation 37 for V_1, it was found that most of

the applied potential is dropped across the reverse biased contact V_1 and was determined to be approximately 4.98 Volts. The hole current like the electron current must overcome the thermionic barrier at interface two. The hole barrier Φ_{p2} is obviously a function of applied voltage so that the hole current will be given as a thermionic emission term at contact two and a diffusion term in the field free region. This is a very important distinction between the hole current and the electron current. The hole current only has one thermionic barrier so that at high applied voltages it will begin to overtake the majority n carrier current. The derivation of the hole current is very similar to the electron current derivation and is given as [13],

$$J_{p1} = \frac{qD_p p_{no} \tanh[(x_2 - x_1)L_p]}{L_p}(1 - e^{-\beta V_1}) + \frac{A_p^* T^2 e^{\beta(\Phi_{p1} + V_{bi})}}{\cosh[(x_2 - x_1)/L_p]}(e^{\beta V_2} - 1), \quad (38)$$

where L_p is simply the diffusion constant and A^*_p is the effective Richardsons constant for holes.

Physically, when the semiconductor region is entirely depleted of carriers, $x_2 - x_1 = 0$, equation 38 will simply reduce to the thermionic emission of holes at contact two. This is expected, since there is no diffusion region when the semiconductor is depleted. Finally by summing the hole current (equation 38) and electron current (equations 35 and 36), we can obtain the total current flowing in an MSM.

$$J_{total} = J_n + J_p \quad (39)$$

Using standard values for the diffusion coefficients and barrier heights equation 39 was plotted as a function of applied voltage. The result is illustrated in Figure 3.9. To obtain the current flowing in the device its necessary to find the effective area of the MSM. For a 100 μm MSM, with 2 μm finger spacing and finger width (on a 10 μm waveguide) the area was found to be in the order of 4.6×10^{-6} cm^2. This would amount to a measured dark current of $\approx 10^{-12}$ amps at 5 volts. Using equation 5, 6 and 39 current vs. voltage for various input powers can be obtained. Since the fabricated devices had dark currents of approximately 10^{-6} amps, it was concluded that these devices behaved essentially as a mix between photoconductors and

photodiodes. Experimentally Zeghbroeck, Patrick et al.[14], have demonstrated MSM detectors with dark currents on the order of 1 nA. Because we did not actively seek to optimize the electrical characteristics of the MSM contact (our emphasis was put mainly on the coupling between the waveguide and detector layer), the large leakage currents would not present a problem as long as the detectors responded adequately to normal input light levels.

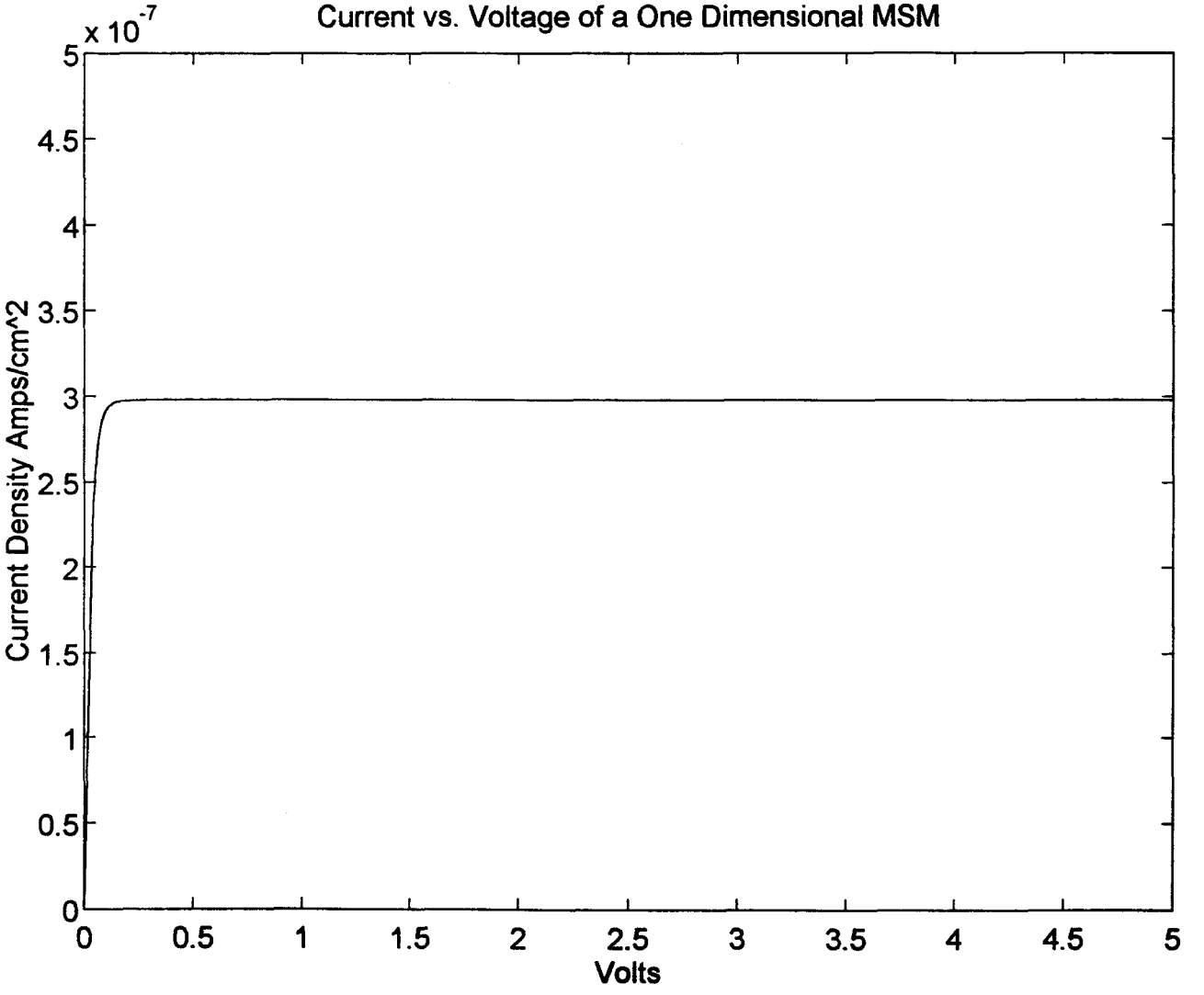

Figure 3.9 Theoretical current flowing in a one dimensional MSM contact.

Chapter 4: Experimental Results

4.1) Introduction

Chapter Two presented a theoretical model that analyzed various solutions of semiconductor dielectric waveguides. Using these models, a single and multi-mode waveguide structure was designed and grown on semi-insulating GaAs (nominally doped to $1x10^{15}/cm^3$). This chapter will begin with an optical analysis of the fabricated waveguides, and present the absorption coefficient of the waveguides in both the passive and detector regions. Once the optical losses were established, the detector responsivities were calculated to obtain an idea of the carrier collection efficiencies. With the dc characterization complete, we examine both the frequency response and the electrical isolation of the detectors.

The waveguide/detector structures were fabricated using the procedures specified in Appendix One. Before the fabrication of the single and multimode structures, a test material sample, which consisted of a GaAs substrate layer, a two micron AlGaAs layer, and a GaAs cap layer, was grown to ensure that device fabrication was not a problem. Figures 4.1 and 4.2 illustrate how the current varies as a function of bias voltage under no illumination and under illumination with a white light source. The presence of the ridge waveguides underneath the MSM detectors did not impede the electrical performance of these devices. The responsivities of these devices were not measured since they were made without the use of a proper mask or waveguiding structure. After the examination of the test waveguide structure was completed, three device structures were grown: The two specified in Figure 2.8 of Chapter Two, and one waveguiding test sample which was used to determine if an etch depth of 0.25 microns, determined by using the effective index method in Chapter Two, was appropriate.

The test waveguide structure labelled #94-091 was grown on semi-insulating GaAs and is

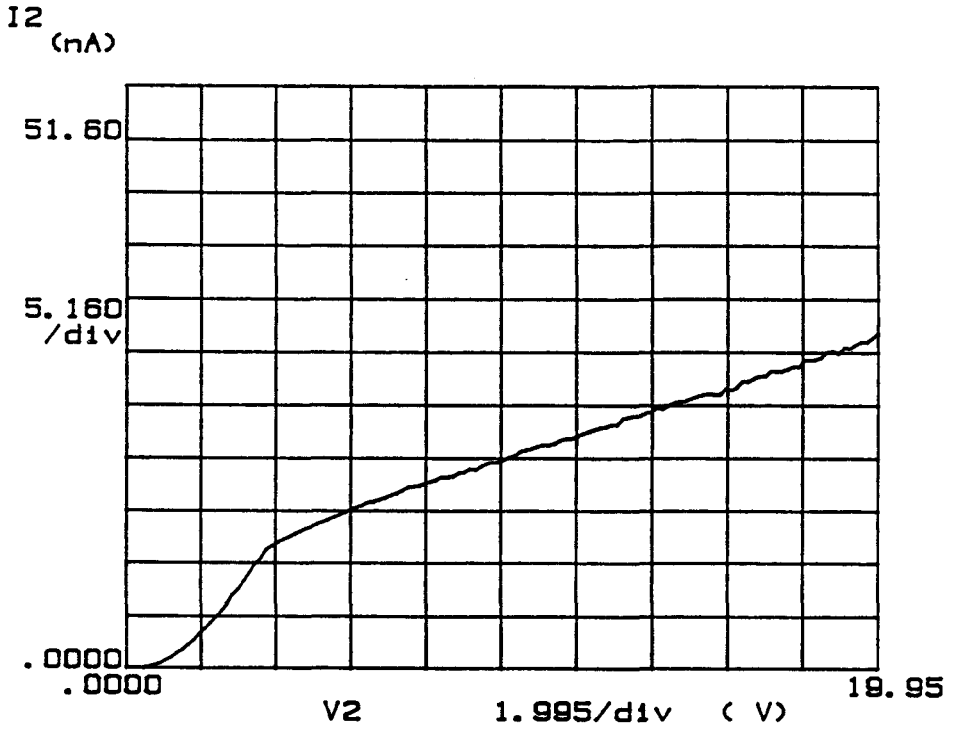

Figure 4.1 Dark current of test waveguide/detector integrated MSM.

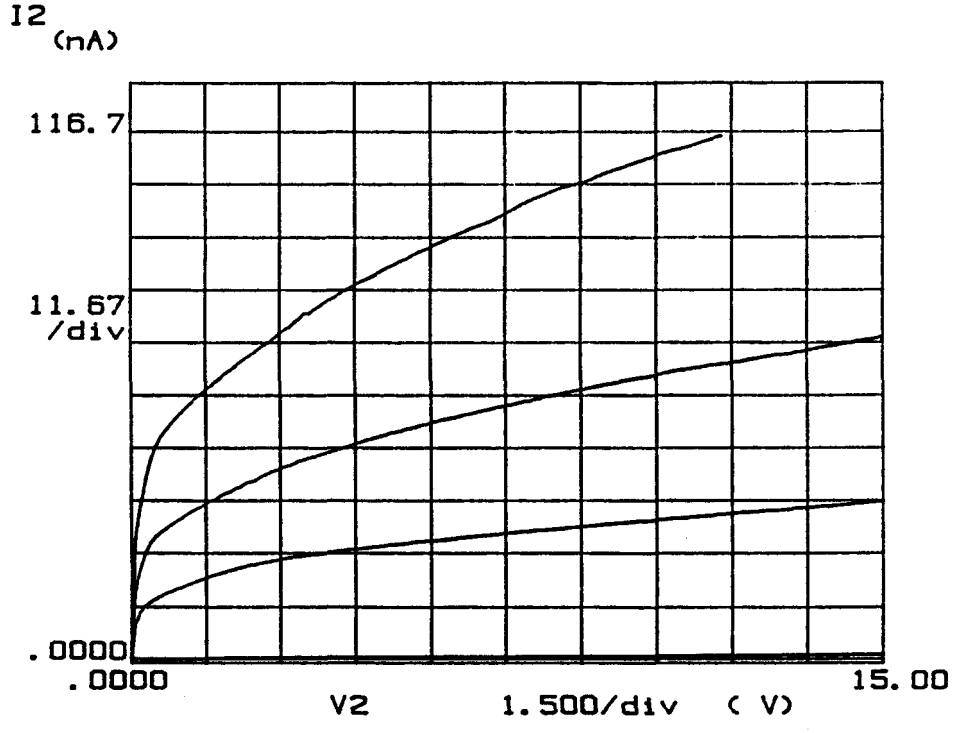

Figure 4.2 Optical response of test waveguide/detector integrated MSM.

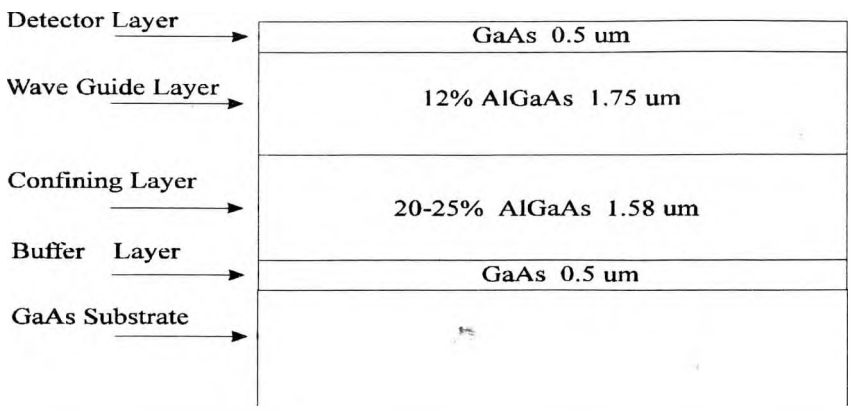

Figure 4.3 Test waveguide material growth specifications.

illustrated in Figure 4.3. To examine the material losses, ridge waveguides were fabricated as specified in Appendix 1. Because we were only interested in the waveguiding characteristics of the sample, and did not concern ourselves with the detector regions, the entire GaAs cap layer was removed to eliminate any excess photon absorption. The sample was mounted on a piezo-electric-controller and then injected with a single mode laser light source at 820 nm. The set up is

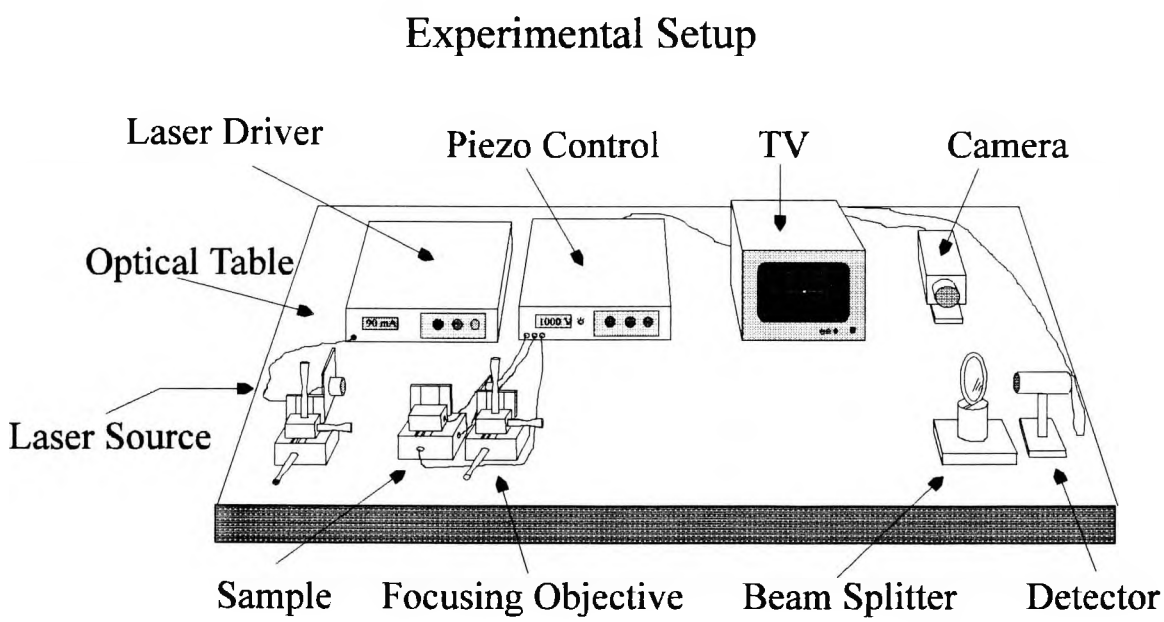

Figure 4.4 Experimental setup for optical attenuation measurements.

illustrated in Figure 4.4.

The laser source was set to an input power of 4543 μW. The system was characterized for optical losses, and it was found that the focusing microscope objective transmitted 81% of the incident optical signal. The Beam splitter transmitted 76% of the incident light, and Fresnel reflection losses [11] for GaAs amounted to a transmission of 70%. In this experiment the beam splitter was not used, but Fresnel and other system losses were accounted for to obtain an effective input power of 1803 μW. The measured output optical powers for both the three and ten micron waveguides are listed in table 4.1.

Table 4.1 Output power of 3 and 10 micron wide test waveguide structure.

Waveguide Width	**Power Out (μW)**	**Loss in decibels (dB)**
3 micron	360 μW	-7
	430 μW	-6.2
	388 μW	-6.7
10 micron	490 μW	-5.7
	330 μW	-7.4
	452 μW	-6
	375 μW	-6.8
	355 μW	-7.1
	440 μW	-6.1
	438 μW	-6.1
	361 μW	-7
Average Power / Loss for 10 μm	405 ± 53μW	-6.5 ± 0.58 dB

The length of the probed sample was approximately 1.358 cm, which would correspond to an

average loss per cm of -4.8 ± .43 dB/cm for the 10 μm waveguides. Because our calculations did not involve the removal of any insertion losses, which arise because the optical modes of the waveguide do not match that of the input fiber, the loss obtained above is quite reasonable. Typical insertion losses vary anywhere from 2dB to 6dB. In general, the amount of coupling between an input optical field and output optical field is determined by the overlap integral of the input and output modes (See [10]). Insertion losses can only be determined by first determining the optical attenuation of power in the waveguide and then subtracting the propagation losses from the total measured loss in the waveguide. Since the fabricated waveguides displayed very little attenuation, an etch depth of 0.25 μm was found to be adequate and would be used in the fabrication of both the multimode and single mode structures.

The structures (Figure 4.5 and 4.6) were grown by MOCVD at the Communication Research Centre. Both structures were grown on semi-insulating GaAs and no layers were intentionally doped. The surface of both detectors was found to have a doping density of approximately 10^{15} donors/cm^2 which is suitable for obtaining a good Schottky contact. The first objective was to determine the absorption of both the passive and detector sections.

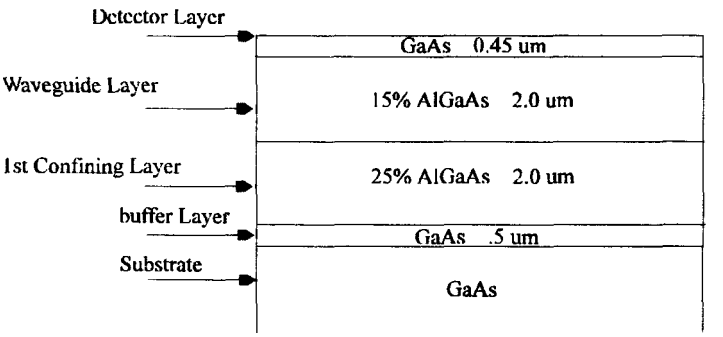

Wafer #94-093 Multimode Waveguide/Detector

Figure 4.5

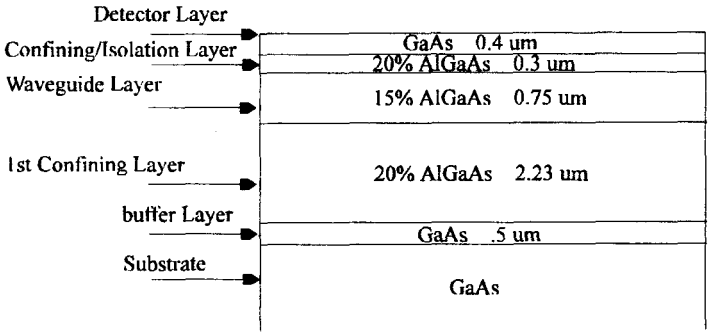

Wafer #94-095 Singlemode Waveguide/Detector

Figure 4.6

4.2.1) Optical Measurements

Optical measurements were carried out for both the single mode and multimode waveguide structures. To determine the detector responsivities, the waveguiding losses in both the passive and detector regions must first be determined. This was done by using a number of different electrical and optical techniques and verifying that each technique was consistent in determining the absorption coefficient. This section will look at the absorption coefficient in both the passive waveguide and detector regions. Optical measurements for the multimode structure are not presented, because these devices displayed very little light sensitivity when placed in detector chains on a waveguide. The losses for the multimode passive waveguides were determined to be either less than or equal to those of the single mode structure.

The optical attenuation of the single mode structure was measured by using the cutback method. This is done by cleaving the sample and measuring the output power at a number of different lengths. The attenuation of power in the waveguides is then determined by examining the exponential decay of power as a function of different length. The single mode structure was cleaved into two different lengths, and the output power was measured at each length as is presented in table 4.2.

Table 4.2 Output power of 3 and 10 micron wide single mode waveguide structure.

Waveguide Width	**Power Out, Length 1.475 cm**	**Power Out, Length 0.719 cm**
3 microns	275 μW	466 μW
	337 μW	406 μW
	243 μW	317 μW
		270 μW
10 microns	310 μW	364 μW
	384 μW	438 μW
	276 μW	430 μW
	326 μW	383 μW
	342 μW	380 μW
	356 μW	
	326 μW	
	355 μW	

The attenuation coefficient alpha, and therefore the propagation losses can be determined by using the empirical relation $I=I_0 \exp(-\alpha x)$ which describes the exponential decay of optical power in the optical waveguides[1]. The measured losses in the passive regions must be determined with relatively long waveguide lead ins because the optical modes require a certain distance to adapt to their waveguide structure [15]. A plot of Log Power vs. distance for the 10 micron waveguides is illustrated in Figure 4.7.

[1] The transfer of power to absorbing layers in stacked dielectric waveguides is not always an exponential decay. There is a certain amount of time required for the power to couple into the absorbing layer [15]. For the single mode structure the losses can be approximated as an exponential decay of power.

Examining the graph, it is evident that the error bars are quite large. This is not an indication of the quality of the experimental data because the scatter in measured power is roughly on the order of 8% which is fairly good. The problem is that the scatter in power is

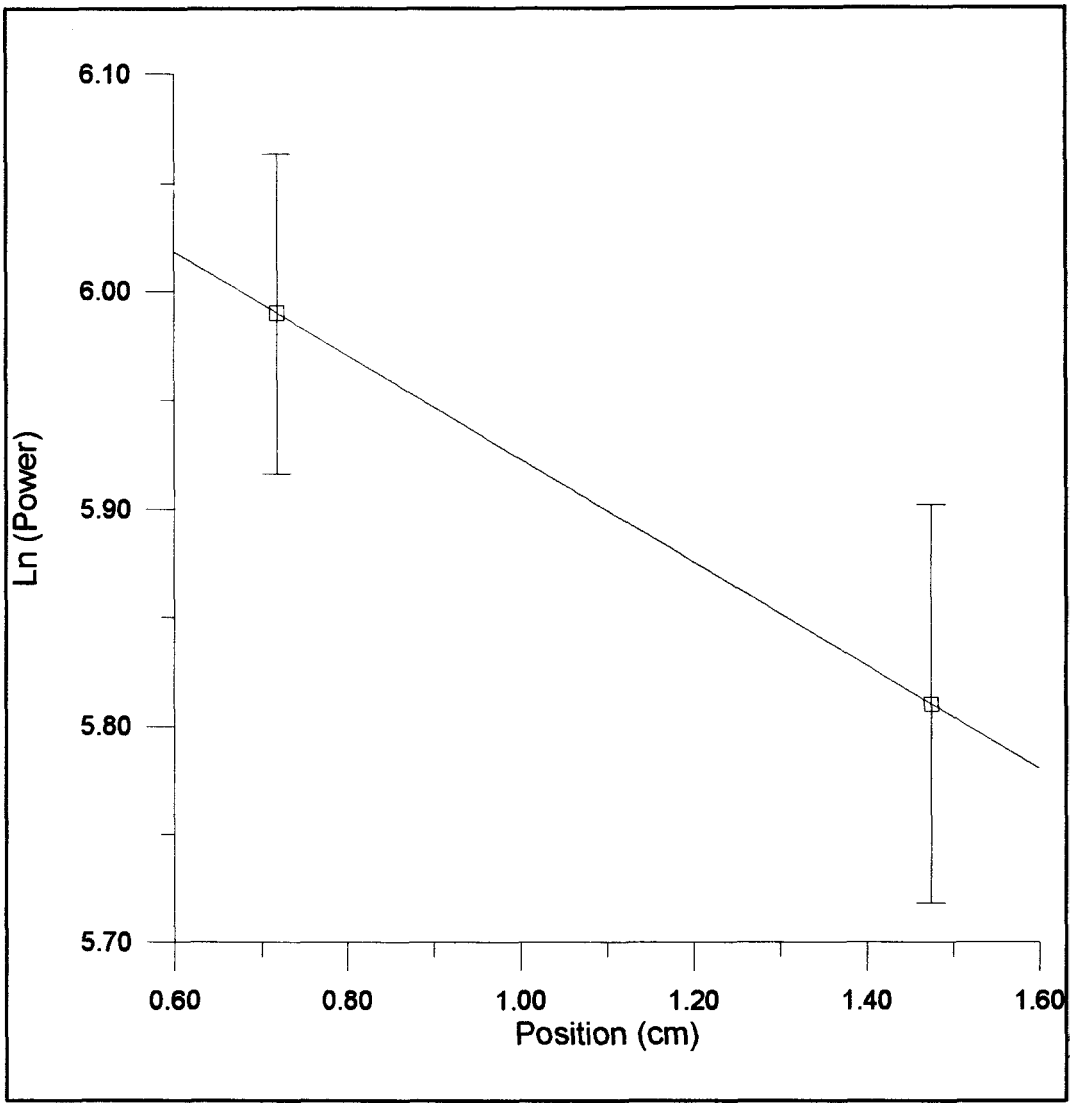

Figure 4.7 Attenuation of optical power in 10 μm single mode passive waveguide section.

spread out over a small distance, which causes an increased sensitivity when calculating the absorption coefficient α. In the extreme case, alpha can take on a value, approximately twice that of the average value. Using the experimental data for the 10 μm waveguides, the attenuation in

the passive section was determined to be approximately 1 ± 0.9 dB/cm. This value is not unreasonable, waveguide losses in GaAs/AlGaAs systems have been reported as low as 0.1 dB/cm [16]. For the three micron waveguides the loss was determined to be approximately 1.4 dB/cm, which is slightly higher than for the ten micron waveguides. This is not unexpected, since a smaller waveguide confines the guided optical mode to a smaller region which makes it more susceptible to waveguide imperfections and defects.

Once the losses in the passive sections are determined, the insertion losses of the waveguides can be calculated. Since the insertion loss is a strong function of both the incident and the coupled waveguide modes [10], the ten micron waveguides are expected to have a lower insertion loss than the three micron waveguides (for the same input field profile). To determine the insertion losses, the passive waveguide loss was subtracted from the total waveguide loss at 1.475 cm. For the 10 micron waveguides the insertion loss was determined to be -4.5 dB and for the 3 micron waveguides the insertion loss was approximately -4.7 dB. This result is consistent with our understanding of overlap integrals, because the three micron waveguides have a smaller mode profile than the ten micron guides. For the same input field, the power coupled into the 3 micron guides should therefore be less than the ten micron waveguides.

4.2.2) Attenuation in the Detector Region

To obtain the absorption coefficient of the material in the detector regions, three different methods were employed. The experimental measurement of alpha in the detector region α_d was fairly tedious to calculate because the material was so strongly absorbing at the operating wavelength of 820 nm. A 100 μm detector region absorbed up to 70% of the incident light, cutback would be almost impossible because the minimum size of the cleaves is larger than the resolution required.

To overcome this problem the mask was designed with sections that had chains of detectors with two micron spacing between them (See Appendix 1). By measuring the photo-current along a detector chain, the absorption coefficient can be obtained. This is only valid

because the absorption coefficient at 820 nm for GaAs is almost all interband absorption. For example, from Figure 2.7 of Chapter Two the experimental absorption coefficient at 820 nm for GaAs is approximately $1.6 \times 10^4\,cm^{-1}$, the interband absorption coefficient derived in Figure 2.5 of Chapter Two is approximately $1.0 \times 10^4\,cm^{-1}$, which is almost equal to the experimental value. The problem encountered with this method was the instability of the piezo-electric positioner. Since very little light made it to the end of any detector chain, any decoupling of the light from the waveguide into the slabguide caused an artificial increase in the photocurrent of the end detectors. This would introduce an unwanted random noise in the measured current.

A second method of measuring the absorption coefficient in the detector region was to examine the ratio of photocurrents for two detectors separated by a fixed distance. Since the current is a function of the incident and absorbed power, alpha can be determined. This was by far the most effective way of determining α_d, and will be presented first.

A third method of determining alpha is to examine the optical output power of small detector chains, and then compare the measured output power to waveguides which had no detectors. A drawback of optical measurements is that the scattering at each detector/waveguide region is not readily obtainable. This does not account for any processing or edge effects that can greatly increase the amount of scattered power[2]. The overlap integral of the input mode and detector guided mode, for a single mode slab waveguide in the vertical direction, yields a 0.98 power transfer (98% of the incident light will be transmitted to the detector guided mode). The overlap integral in the horizontal direction is a function of detector length, since the width of the detector regions are wider than the ridge waveguides, the optical mode will propagate and spread out like a Gaussian beam. Poor confinement in the lateral direction can only decrease the amount of power transferred at the intersections. It will be shown that the optical measurements are fairly consistent in determining α_d when scattering is considered. [A true verification of alpha will be the determination of the responsivity of detectors with equal lengths. If the correct percentage of power is removed the responsivities should be approximately equal.]

As was discussed in Chapter 2 and above, the decay of optical power in waveguides can

---

[2] Since, there is no selective etch for GaAs on 15% AlGaAs, timed etches were required which could have penetrated deeper into the waveguiding regions. This would have had a large effect on both the incident mode and power transfer to the detector mode.

be expressed as an exponential. Therefore, the measured photocurrent in the detector regions can be written as, (see Chapter 3)

$$I_{1,2} = RP_{1,2}(1 - e^{-\alpha_d L}), \tag{1}$$

where $P_{1,2}$ is simply the power input into the detector, and R is the responsivity of the device. Since the responsivity is the same for identical detectors, the ratio of the current for two adjacent detectors, $I_{1,2}$ can be expressed as,

$$\frac{I_1}{I_2} = \frac{P_1}{P_2} = e^{\alpha_2 d} e^{\alpha_1 L}. \tag{2}$$

By experimentally measuring the current in both detectors, and using the observed value of alpha $\alpha_1 = 1$ dB/cm in the passive waveguiding region, we can determine the absorption coefficient α_d. A two dimensional representation of the decay of power is illustrated in Figure 4.8. By looking at ten different detector chains, alpha in the detector region was determined and the results are given in table 4.3.

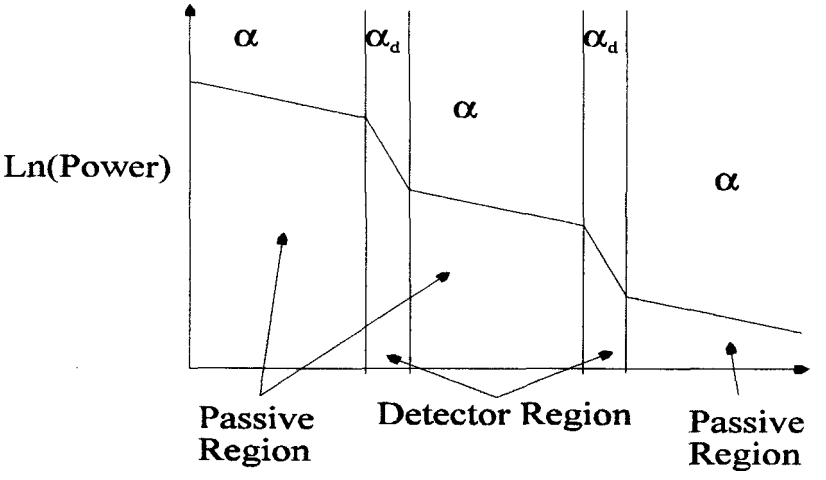

Figure 4.8 Cross-section of power attenuation in two detector waveguide.

Table 4.3 Measured currents of sequential detectors on a single mode waveguide/detector structure. Used to determine the absorption coefficient in the detector region.

Measured Current Detector Number 1 Amps (A)	**Measured Current Detector Number 2 Amps (A)**	**Calculated Alpha (cm^{-1}) using equation 2.**	**Variance**
0.00065419	0.00022825	-100.9	193.8
0.00080785	0.0002632	-107.7	50.0
1.24100E-03	3.5131E-04	-121.8	48.7
1.24100E-03	3.7470E-04	-115.3	0.3
7.2870E-04	0.00029366	-86.5	802.9
9.0071E-04	0.00033236	-95.3	381.1
6.11660E-04	3.05500E-04	-130.0	231.3
7.20860E-04	3.46000E-04	-137.9	536.6
7.62970E-04	3.86600E-04	-127.1	152.0
8.26750E-04	4.22700E-04	-125.3	110.9
	Average Alpha	-114.8	Std. dev: 15.8

The average value of alpha obtained for the waveguide detectors using this method is 115 cm^{-1} ± 16 cm^{-1}. This value is significantly different than the required 70 cm^{-1}, which would balance the optical switch. There are a number of reasons why the observed alpha is different than the modelled alpha, the most important are layer thickness variations and imperfections in the processing. The effect this has on the observed current will be explained later.

To verify the attenuation of optical power in the detector regions, the exponential decay of current in detector chains was also examined. These measurements were taken with the use of a lock-in amplifier at a laser modulation frequency of 1000 Hz. Alpha was determined for the single mode structure in a number of different detector chains. Figure 4.9 illustrates the exponential decay of current with distance penetrated into the detector chain. The range of the measured α_d using this method was approximately α_d=98 cm^{-1} to α_d=128 cm^{-1}. Although this method was not

as accurate as the first method, the results of both methods did not conflict with one another. You will notice that the value of alpha determined above including the scattering envelopes both extremes of α_d measured with this method.

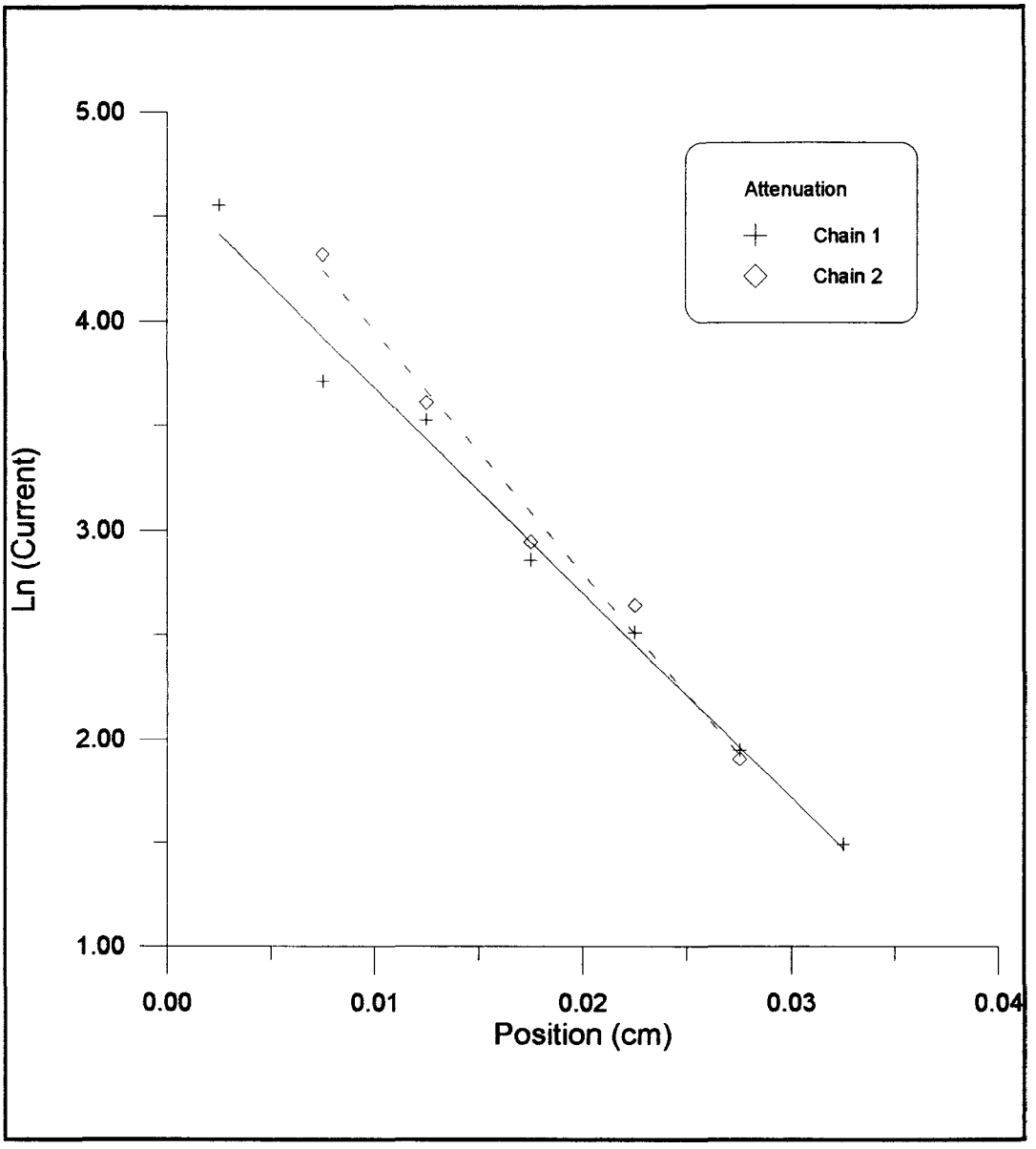

Figure 4.9 Attenuation of power in the detector region using "chain detectors".

As a final method of verifying alpha in the detector region, optical through-put

measurements for straight waveguides with no detectors were compared with waveguides that had two equal length detectors[3]. By looking at the measured output power of the waveguides with detectors, we can obtain an idea of the power absorbed in the detector regions. Since the length of the detectors is known, the absorption coefficient can be verified. Ten waveguides were analyzed in total, five waveguides had no detectors, and five waveguides had either 50 μm or 100 μm long detectors.

Because the optical mode is undergoing a change in the surrounding medium when it enters the detector sections, a fraction of the incident light will be scattered at each detector/waveguide intersection [9]. This scattered light comes about because of the difference in mode profiles in both the passive and detector regions, and due to processing imperfections. Since we cannot quantify the amount of scattering incurred due to processing, only the scattered power due to mode mismatch will be considered, and the true scattering can only be greater than this value.

The overlap integral of the incident waveguide mode and detector mode, will determine how much of the incident light is coupled into the detector modes. For the single mode structure it was determined that the optical power transfer to the detector region, in the vertical direction, is approximately 0.98 %, as discussed above. The problem with this derivation is that the electric field is also confined in the horizontal direction and since these devices were fabricated with a detector that was much larger than the waveguide, confinement in the horizontal direction will be poor[4]. To find how much power is lost in the horizontal direction, the overlap integral in the lateral direction must be determined. When this is considered, coupled with the fact that the processing can increase the power lost, the results are fairly consistent.

A simple and accurate method of determining the overlap integral in the horizontal direction is to use a Gaussian beam propagation. Since we are only interested in an approximate solution, most of the optical power (99%) was confined to a Gaussian beam inside a 10 μm

---

[3] This method assumes that the cleaves, and hence the insertion losses, for adjacent waveguides are equal.

[4] The light will spread out in the horizontal direction because the waveguide detector intersection will behave like a slit.

waveguide. The beam was then allowed to propagate down the detector region and the overlap integral was determined. By confining the light entirely to the waveguide region we will obtain a upper limit on the amount of transferred power. The true loss can only be greater than this. The amount of scattered light for various detector lengths is illustrated in table 4.4. You will observe that the detectors should have approximately the same width as the waveguides if 100% throughput is required.

Table 4.4 Power transfer between waveguide/detector interface.

Detector Length	**Power Transferred at Detector Waveguide Interface.**
45 μm	90 %
63 μm	81 %
106 μm	59 %
177 μm	31 %

A section of material was cleaved to approximately 2.25 mm and mounted in the experimental setup of Figure 4.4. In total, 10 adjacent waveguides were examined, 5 waveguides did not have detectors and 5 waveguides had 2 detectors each. Table 4.5 presents the measured experimental data. Column 2 is the power measured through an adjacent straight waveguide with no detectors. Column 3 is the calculated output power using an absorption coefficient of 115 cm^{-1} and the scattering at each detector obtained above. Column 4 is the experimentally measured power. At first glance it is evident that the calculated power and measured power do not agree very well. We must remember that our method in determining the overlap integral was a lower limit. The true loss can only be greater than the numbers that we have determined. Unfortunately there is no way of quantifying exactly all the different experimental losses. Since we are only dealing in the tens and hundreds of micro-watts, and because our analysis was simply an approximation, the results are not unreasonable.

Table 4.5 Comparison between measured and calculated output optical power in waveguides with detectors and waveguides with no detectors.

Detector Length 10 μm Waveguides	**Measured Power No Detectors**	**Calculated Power Output**	**Measured Power with Detectors**
100 μm	482 μW	14 μW	5.37 μW
50 μm	471 μW	106 μW	40.1 μW
50 μm	490 μW	109 μW	39.3 μW
100 μm	504 μW	15 μW	4.75 μW
50 μm	480 μW	108 μW	52 μW
Average Power	485.4μW		

Since we have measured the output power of five waveguides that are different from those used in the cutback method, we are in a position to verify the validity of the losses computed for our optical system. The input power in all measured cases including column 2 of table 4.5 was determined to be approximately 4500 μW. Fresnel losses for GaAs are approximately 30% absorption/facet [11], the beam splitter reflects approximately 24% of the incident light, the microscope focussing objective reflects 18.82 % of the incident light. The computed insertion from section one for 10 μm waveguides was approximately -4.5 dB. The power remaining is approximately 487 μW, accounting for the absorption in the waveguides, which was calculated to approximately 1dB/cm the power at the waveguide should measure approximately 460 μW. Using the average value of power measured in column two this corresponds to an error of approximately 5 %.

4.3) Detector I-V Response and Responsivities

Section 4.3 will examine the electrical characteristics of the fabricated waveguide detectors. Using the experimentally determined absorption coefficient for both the passive and waveguiding regions, the dc responsivities for the 50 μm and 100 μm long detectors will be calculated. Both the three and ten micron wide waveguides of the single mode and multimode detectors were deposited with Platinum, Gold and fabricated according to the procedures specified in Appendix 1. By looking at the electrical characterization of the detectors we will demonstrate that the 10 μm wide single mode structure is the best candidate for the 4x4 switch.

The single and multimode waveguides were mounted in the experimental setup of Figure 4.10. A HP parameter analyzer was used to acquire the current vs. voltage characteristics at various input laser light intensities. Many devices were analyzed and typically all devices had a dark current of approximately 1-20 μA at 5 volts. Figure 4.11 illustrates the dark current for a typical 100 μm long,

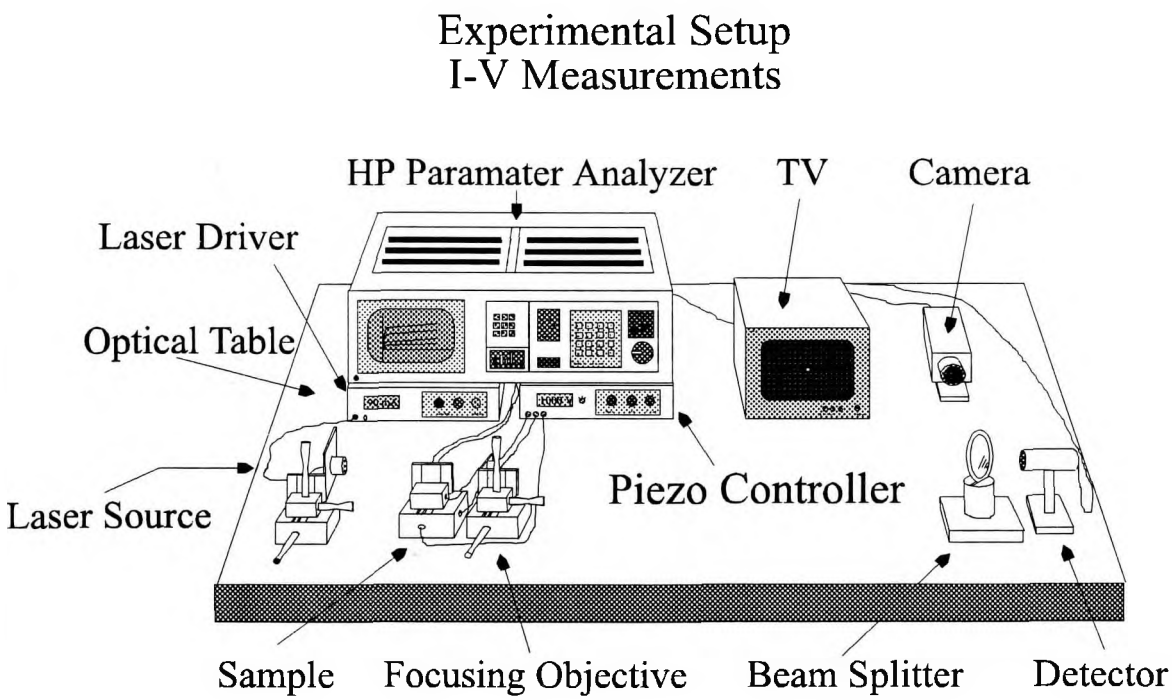

Figure 4.10 Experimental setup for electrical characterization.

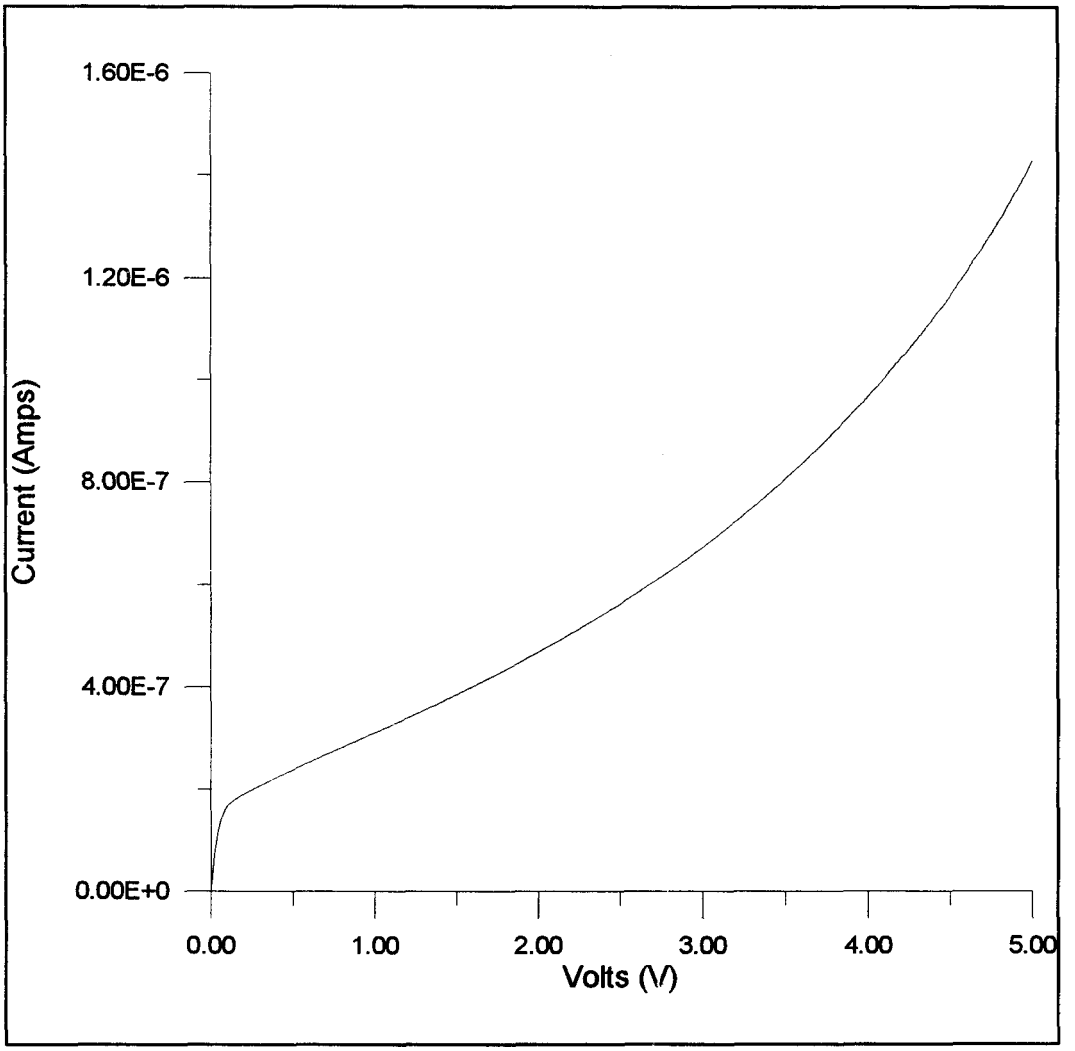

Figure 4.11 Dark current for a 100 μm long, 10 μm wide, single mode waveguide detector.

10 μm wide, single mode detector. It is evident that the electrical response of the 100 μm detector, does not correspond to the I-V's of a good MSM photodiode. The current in Figure 4.11 behaves as a combination of both a photodiode and photoconductor. It is evident that the diode has a definite photoconductive component, which is characteristic of an ohmic contact. Comparing this to Figure 3.9 of Chapter Three, we see that there is a substantial leakage current at the MSM interfaces[1]. The current for an MSM photodiode should remain flat up to the reach

[1] To obtain a good Schottky contact the number of surface defects should be kept to a minimum, the fact that the metal was deposited on a ridge waveguide must have introduced a number of surface defects which pinned the Fermi level [12].

voltage, and then exponentially increase as the applied bias decreases the thermionic emission hole barrier to its limiting value[2].

To calculate the responsivities of the detectors, the I-V's were obtained for different input laser powers. The current as a function of input power, should scale according to equation 5 of Chapter Three. Figure 4.12 illustrates the I-V characteristics of a typical 100 μm long detector on a 10 μm single mode waveguide under different input laser powers.

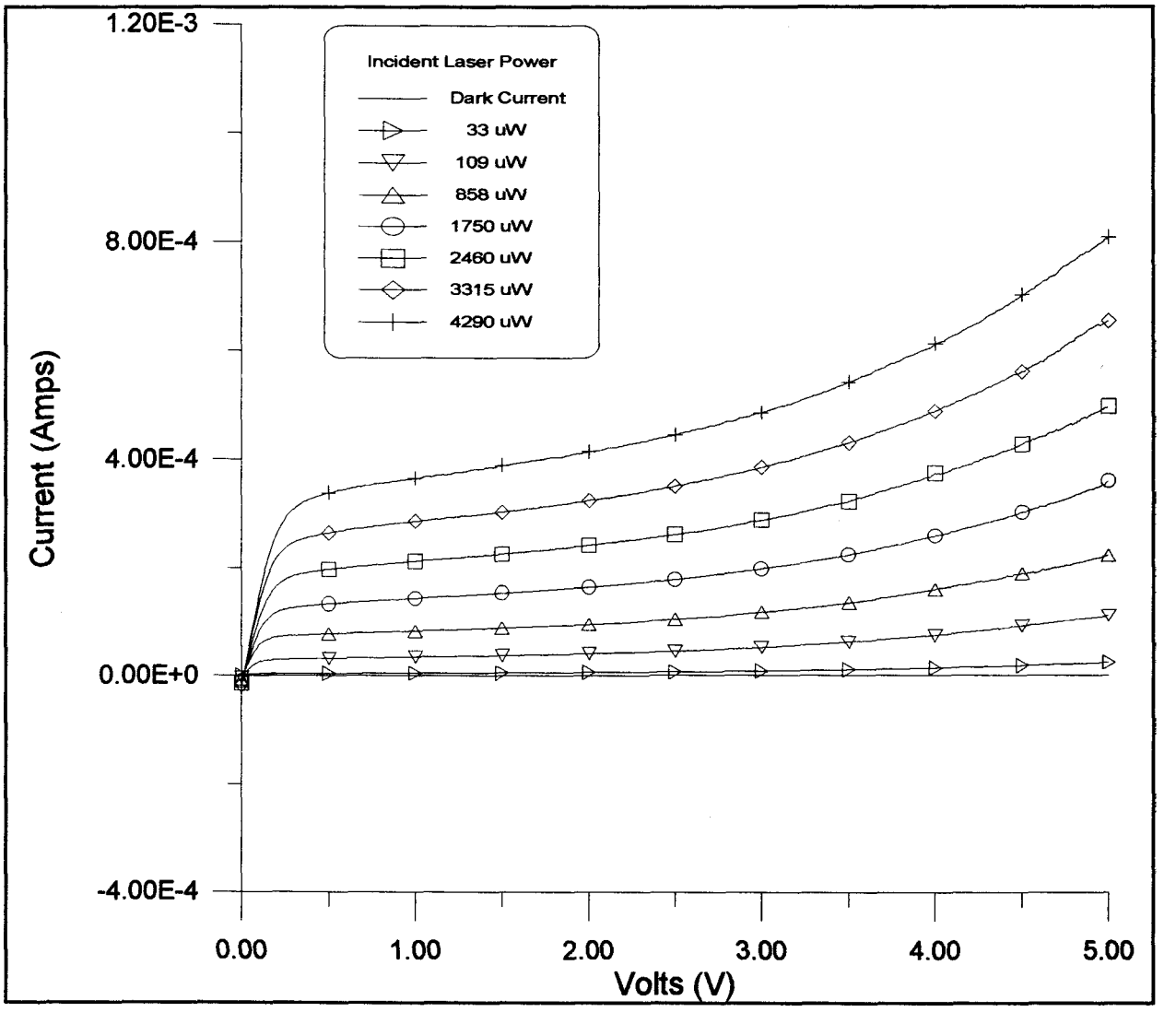

Figure 4.12 Detector I-V of a 100 μm long, 10 μm wide, single mode detector at different input laser powers.

[2] See chapter two.

The dark current, which is illustrated in Figure 4.12, is not observable due to the difference in scale. It was found that all single mode detectors displayed a large sensitivity to incident laser light, however, this was not the case for the multimode structure.

In the multimode sample, only the first detector in a detector chain had a significant response to the incident light. Furthermore, the output optical power in the waveguides was many orders of magnitude greater than that of a corresponding single mode waveguide. This was not consistent with the theoretical waveguide calculations of Chapter 2 because the GaAs should have absorbed the incident power according to the BPM results[3]. The downfall of the multimode structure is inherently due to its multimode nature. Because the GaAs cap only absorbs the evanescent tail of the incident mode, the amount of coupling in the GaAs layer will be a strong function of how much power is coupled into specific guided modes. The coupling into specific guided modes is determined by the overlap integral of the incident and guided modes [9]. Therefore, if most of the laser light is coupled into the fundamental mode, the coupling into the GaAs layer will not be very strong. For example, if there were three guided modes in the multimode waveguide, the higher order modes would be absorbed first because they have the longest and hence the deepest penetrating evanescent tail. As the electromagnetic wave propagates down the guide, only the first detector will respond to the incident light since there may be very little power left over for the remaining detectors. This creates a "mode selector", whereby only the lower order modes survive, and is not very useful for a switch since you need all detectors on a waveguide to be sensitive to the incident light. Typical I-V curves at various laser powers for a 100 μm multimode detector are illustrated in Figure 4.13. Examining Figure 4.13, one might be inclined to think there is nothing wrong with the response of the 100 μm detector. In fact, the observed dc responsivity of this detector is quite poor at 0.07 A/W, as compared to single mode detectors, which had typical responsivities of 0.7 A/W. In general, the best responsivities were obtained by the 10 μm single mode waveguide structure.

The dc responsivities for the single mode detectors were calculated using the optical characterization described in the previous section. In this case, we are only interested in the

---

[3] Or very similar to the BPM results.

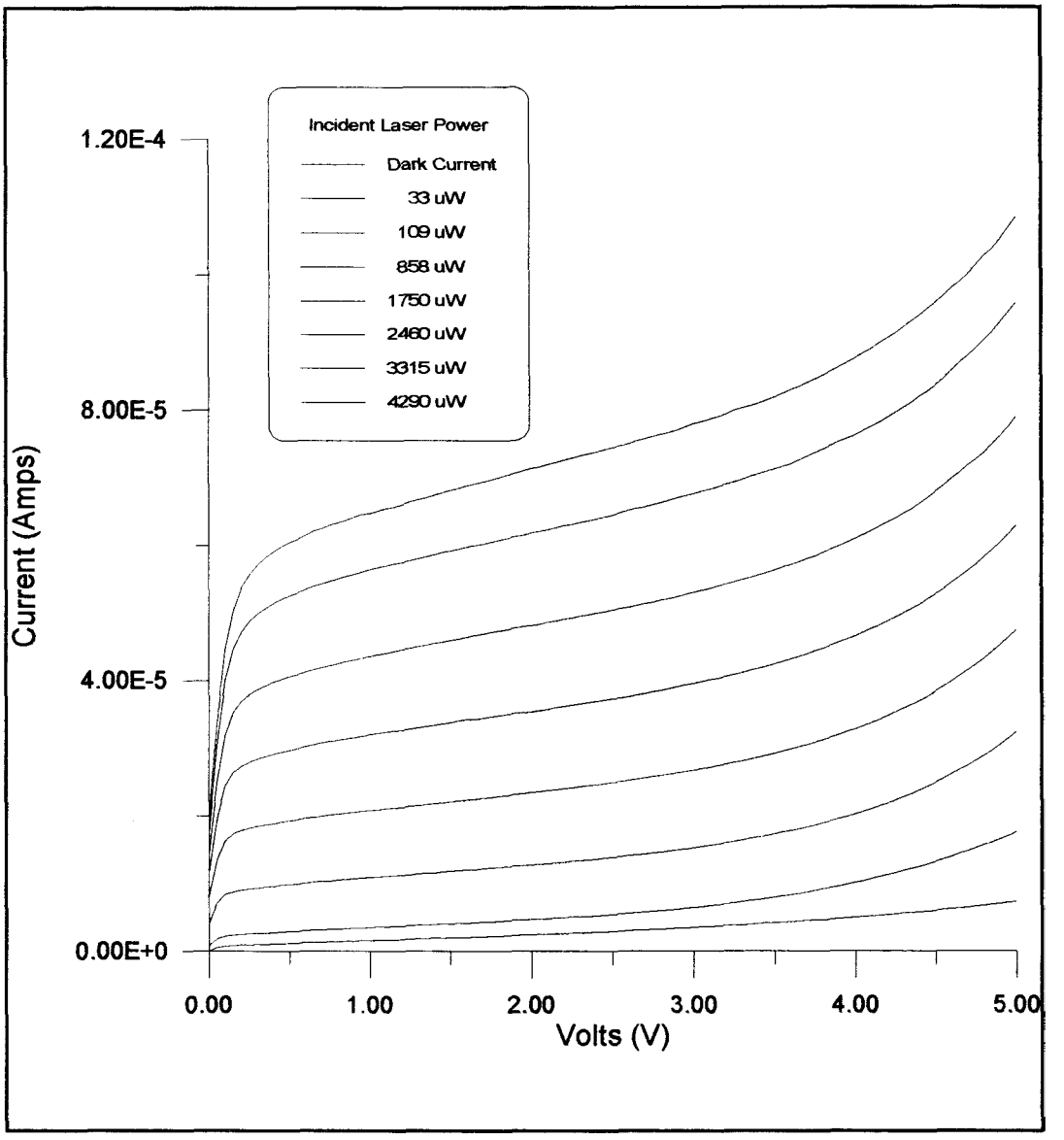

Figure 4.13 Detector I-V of a 100 μm long, 10 μm wide multimode detector at various input laser powers.

response of the detectors and not the waveguide as a detector. The definition of responsivities can be somewhat confusing. For instance, if these devices were going to be used as waveguide detectors, the power that is reflected at the surface and absorbed in the lead-in section of the passive waveguide should not be removed when calculating the input power but, since we are primarily interested in the responsivity of the detector section the system losses must be removed.

This is an important point which should not be confused when calculating the quantum efficiency since otherwise, erroneous calculations would be obtained.

The responsivities of the single mode waveguide detectors were determined at an operating voltage of five volts[4] and only 10 μm waveguides were analyzed, since they worked much better than other waveguide combinations. The input laser power for each detector was determined by subtracting from the measured input power the optical losses, obtained from the previous section. Figure 4.14 illustrates the responsivity of a 100 μm detector. For this particular detector the calculated responsivity was approximately 0.77 A/W. In almost all cases the devices responded linearly to various input powers, and no measured responsivities ever exhibited a goodness of fit less than 0.95. In fact most cases exhibited a goodness of fit which was approximately 0.99.

The detector responsivities were determined both for waveguides that had single detectors and detectors pairs that were spaced by 1000 μm. The results are listed in Table 4.6. When the detectors appear sequentially down a waveguide, they are numbered in the order that they appear. Most detectors of similar length exhibited similar responsivities, as is expected. The responsivities for 50 μm detectors were roughly in the range of 0.5 - 0.6 A/W while the 100 μm detectors exhibited responsivities between 0.8 and 1 A/W. An important consequence of this result is the verification of the optical measurements above.

[4] Five volts was chosen because it seemed to be the voltage just before device breakdown. Since we are interested in depleting the entire semiconductor, 5 volts was determined to be adequate.

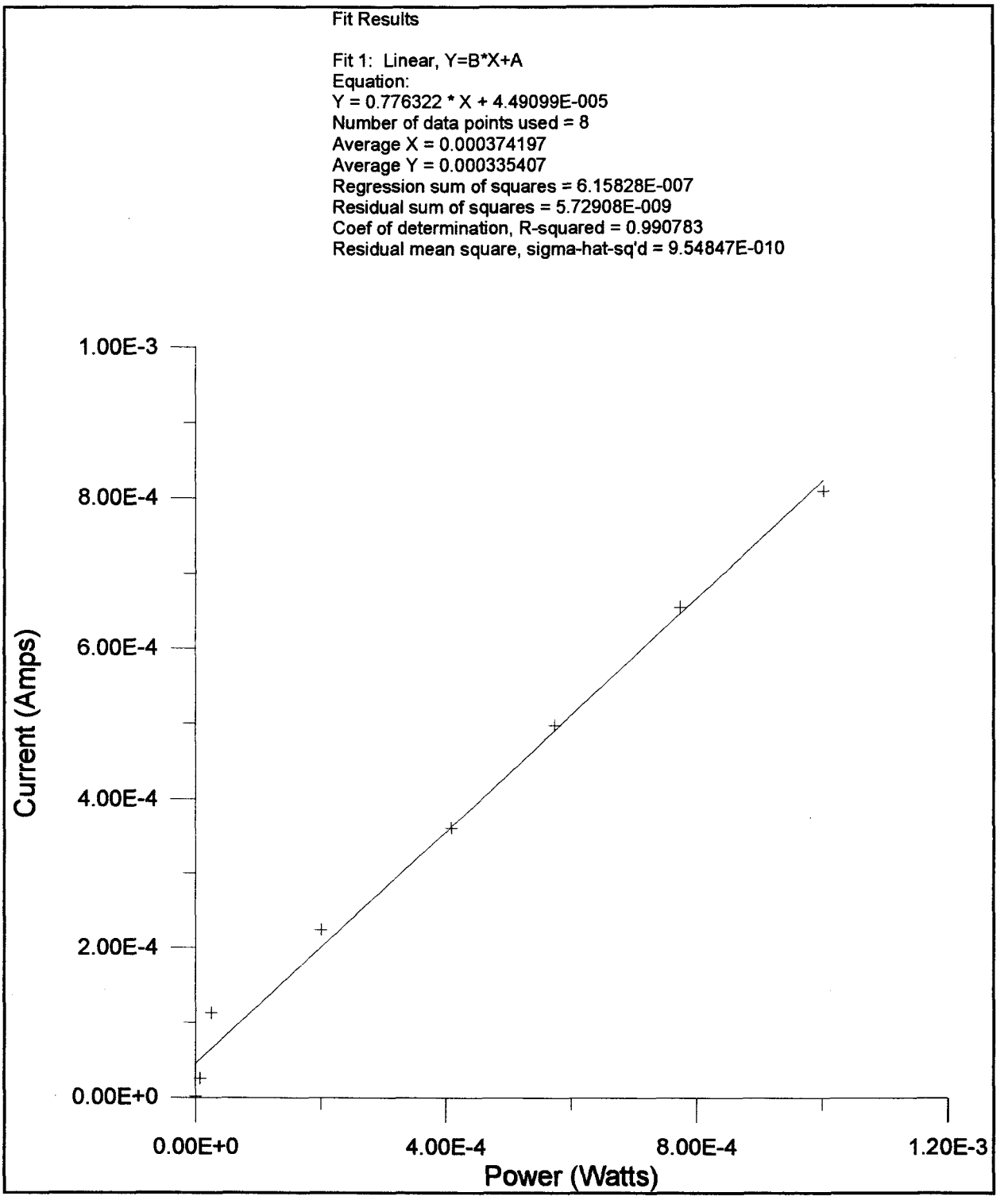

Figure 4.14 Responsivity of a 100 μm long 10 μm wide single mode detector.

Table 4.6 Measured detector responsivities as a function of detector length.

Detector Type	**Detector Number in Waveguide chain.**	**Detector Length**	**Measured Responsivity**
MSM	Detector One	100 μm	0.78 A/W
MSM	Detector Two	100 μm	0.64 A/W
MSM	Single Detector	200 μm	0.93 A/W
MSM	Single Detector	100 μm	2.00 A/W
MSM	Detector One	100 μm	1.05 A/W
MSM	Detector Two	100 μm	0.65 A/W
MSM	Detector One	100 μm	0.77 A/W
MSM	Detector Two	100 μm	0.79 A/W
MSM	Detector One	50 μm	0.52 A/W
MSM	Detector Two	50 μm	0.36 A/W
MSM	Single Detector	50 μm	0.60 A/W
CMSM	Detector One	100 μm	0.98 A/W
CMSM	Detector Two	100 μm	0.95 A/W
CMSM	Single Detector	50 μm	0.58 A/W

The high responsivities exhibited by these detectors is directly linked to the photoconductive gain process discussed in Chapter Three. Since the gain is a strong function of the carrier transit times and excess carrier recombination lifetimes, a comparison of theoretical and experimental responsivities would not be productive. But, using equation 4 of Chapter Three and the experimentally determined absorption coefficient of 115 cm^{-1}, we can show that the responsivities of the 100 μm detectors should be approximately 1.4 times the responsivities of the 50 μm detectors. This is in good agreement with the experimental values and is a strong verification of the absorption coefficient in the detector section.

The electrical response of multimode waveguide detector was not nearly as sensitive to incident light as a corresponding single mode waveguide. The best responsivities obtained for a 3 μm multimode 100 μm detector was 0.12 A/W, which was significantly less than the worst 10 μm single mode detector. All 10 μm wide multimode waveguide detectors had responsivities which were typically in the tens of mA/W range. Because of the poor results obtained for the multimode waveguides, and the 3 μm single mode waveguides, they will not be analyzed further.

Another important factor which was not addressed in the mask design was the optical isolation of the waveguides. The optical isolation is simply the amount of waveguided light that leaks to an adjacent waveguide, thereby increasing the amount of input optical power. To demonstrate the optical isolation, the laser light was injected into a straight 10 μm waveguide adjacent to the waveguide that incorporates a 100 μm detector that was biased from 0 to 5 volts. Figure 4.15 illustrates the change in the noise level of the 100 μm detector before and after illumination. The dark line is the detector dark current with no light in an adjacent waveguide and the dashed line is the current with the laser light injected into an adjacent waveguide. This problem is not insurmountable since, by etching isolation trenches down to the substrate layer between waveguides, the light leakage could be reduced to zero. The light would then be confined to both the ridge waveguide and a small planar waveguide slab region. Although the amount of power coupled into the adjacent waveguide is small, the high speed performance might be affected by this power thereby infecting the quality of information transferred. The amount of coupling between waveguides could not be specified, since the amount of waveguide coupling was strongly dependent on the input fiber position.

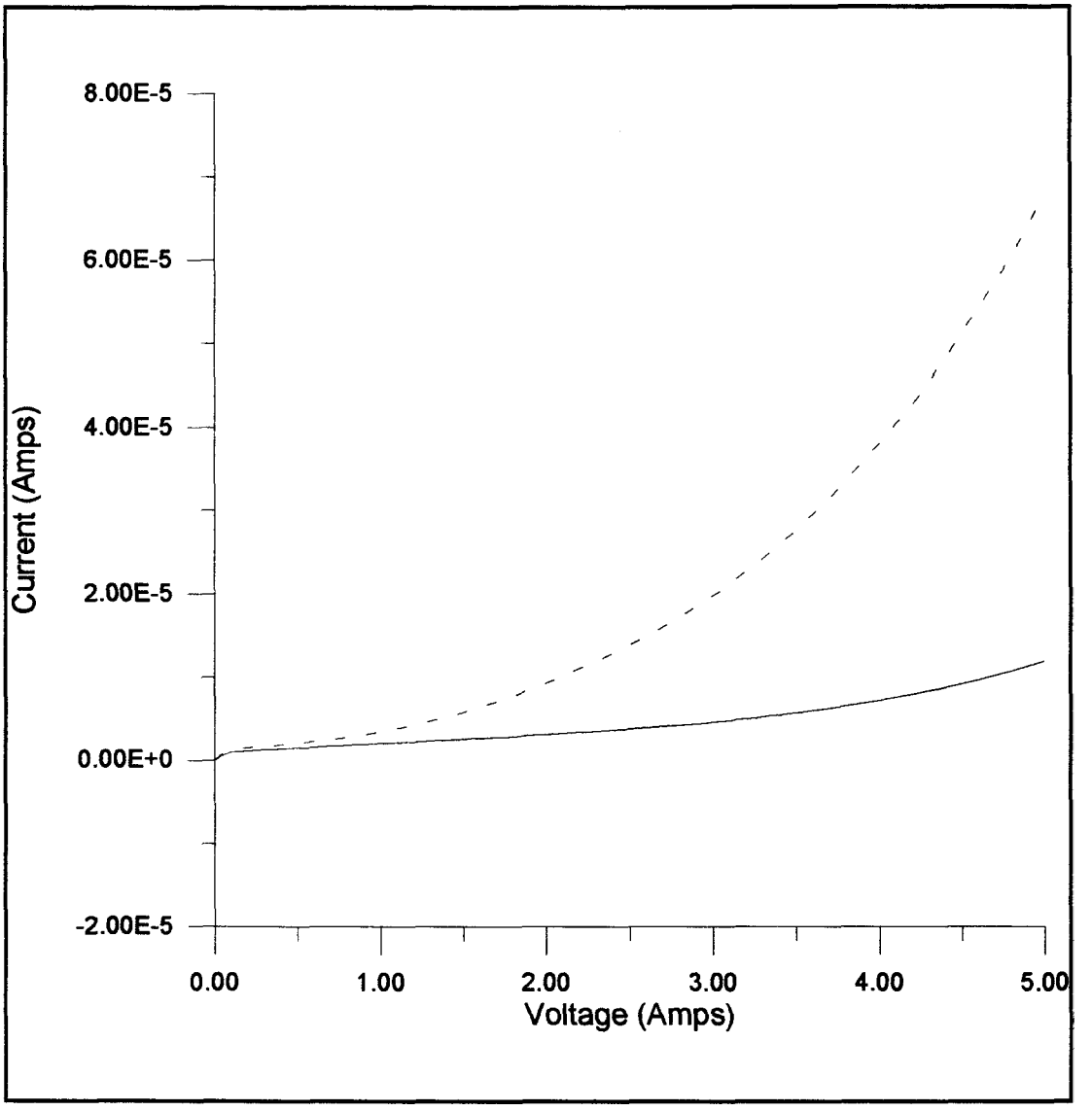

Figure 4.15 Optical isolation of a 100 μm long single mode waveguide detector.

4.4) Analysis of a 4x4 MSM Detector Array

After establishing the best combination of waveguide detector structure and thickness, a single mode 10 μm device was fabricated according to the procedure specified in Appendix One. It was stated in the mask design that the absorption lengths for the switch were designed with the intention of 100 μm 3 dB length absorption coefficient. We have demonstrated however, that the

absorption coefficient for the waveguide detector regions is much larger than the theoretically modeled value. Having an absorption coefficient different from the required value will cause the detectors in the 4x4 switch to absorb unequal amounts of power. (In systems applications this is an unwanted effect. While it is not crucial to balance the switch the detectors should absorb roughly equal amounts of power.) We will show, that the theoretical absorption of power in each detector as a function of absorption coefficient and the measured absorbed power as a function of wavelength follow very similar trends.

The responsivities for various detectors in the matrix switch were also examined. Figure 4.16 illustrates a typical current vs. voltage characteristic for the first detector in a row of a 4x4 waveguide. The responsivity of this particular detector was 0.34 A/W, which is consistent with the responsivities of other detectors measured above. We will now investigate how the current varies down a waveguide detector chain.

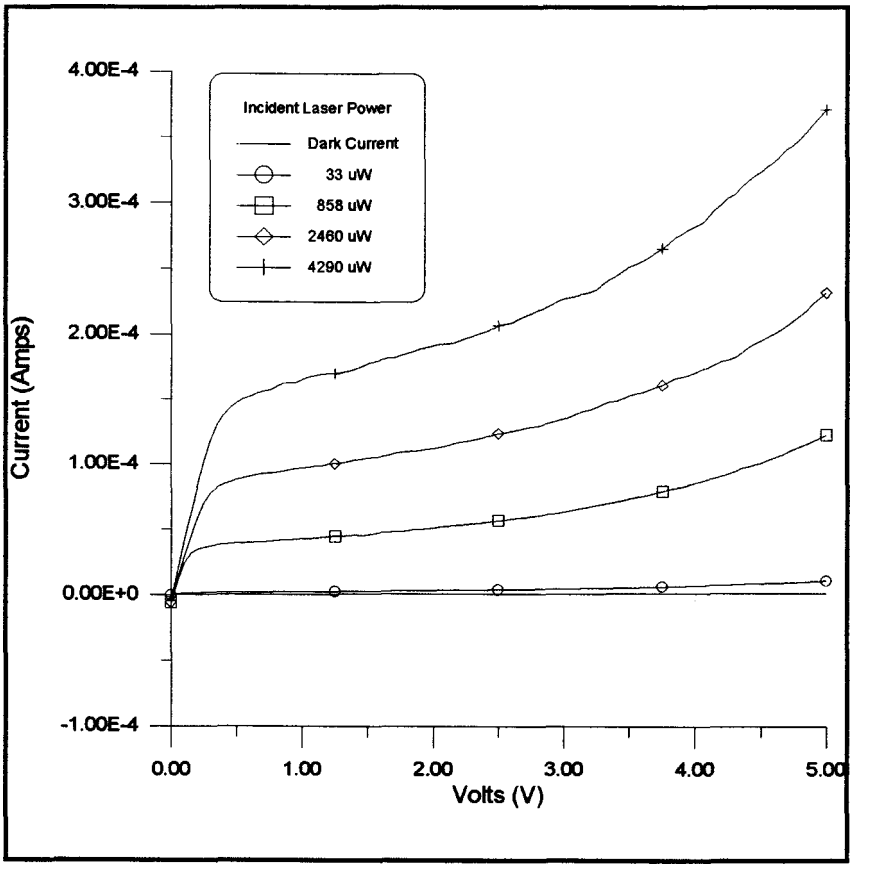

Figure 4.16 Responsivity of the first detector in the 4x4 switch.

The four detectors on the single mode waveguide switch had lengths of 45,63,106 and 177 microns (See Figure A.4 of appendix 1). With 4.4 mW of power injected into the waveguide, the observed photocurrent was plotted as a function of detector number down the waveguide chain. The observed current for a typical waveguide in the 4x4 array is plotted in Figure 4.17.

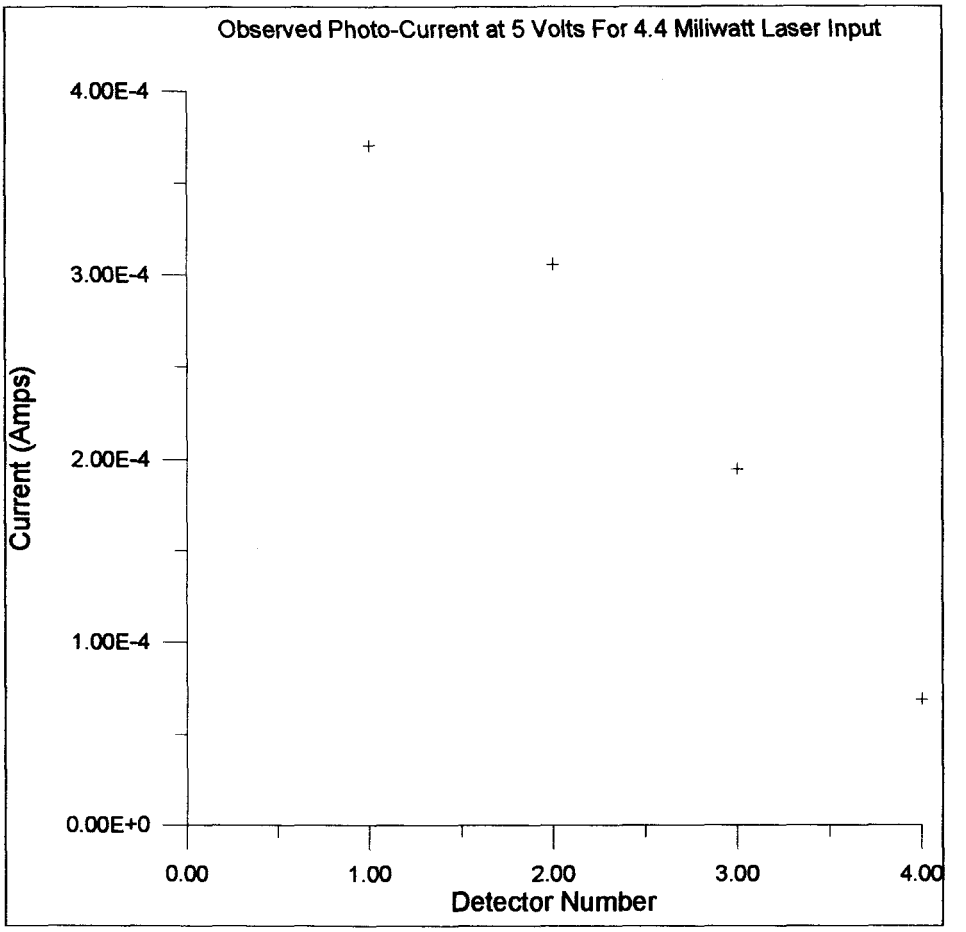

Figure 4.17 Variation of photo-current in a 1x4 detector waveguide chain.

Using Equation 3 of Chapter Three we can estimate how much power is being absorbed by each detector as a function of absorption coefficient. Figure 4.18 illustrates the theoretically absorbed power as a function of absorption coefficient. Notice that theoretically all four detectors do not absorb exactly equal powers for any value of the absorption coefficient. This is because the last detector in the switch should be infinitely long to tap all of the remaining optical power. At an

absorption coefficient of 115 cm^{-1} we see that the detectors cannot absorb equal amounts of power.

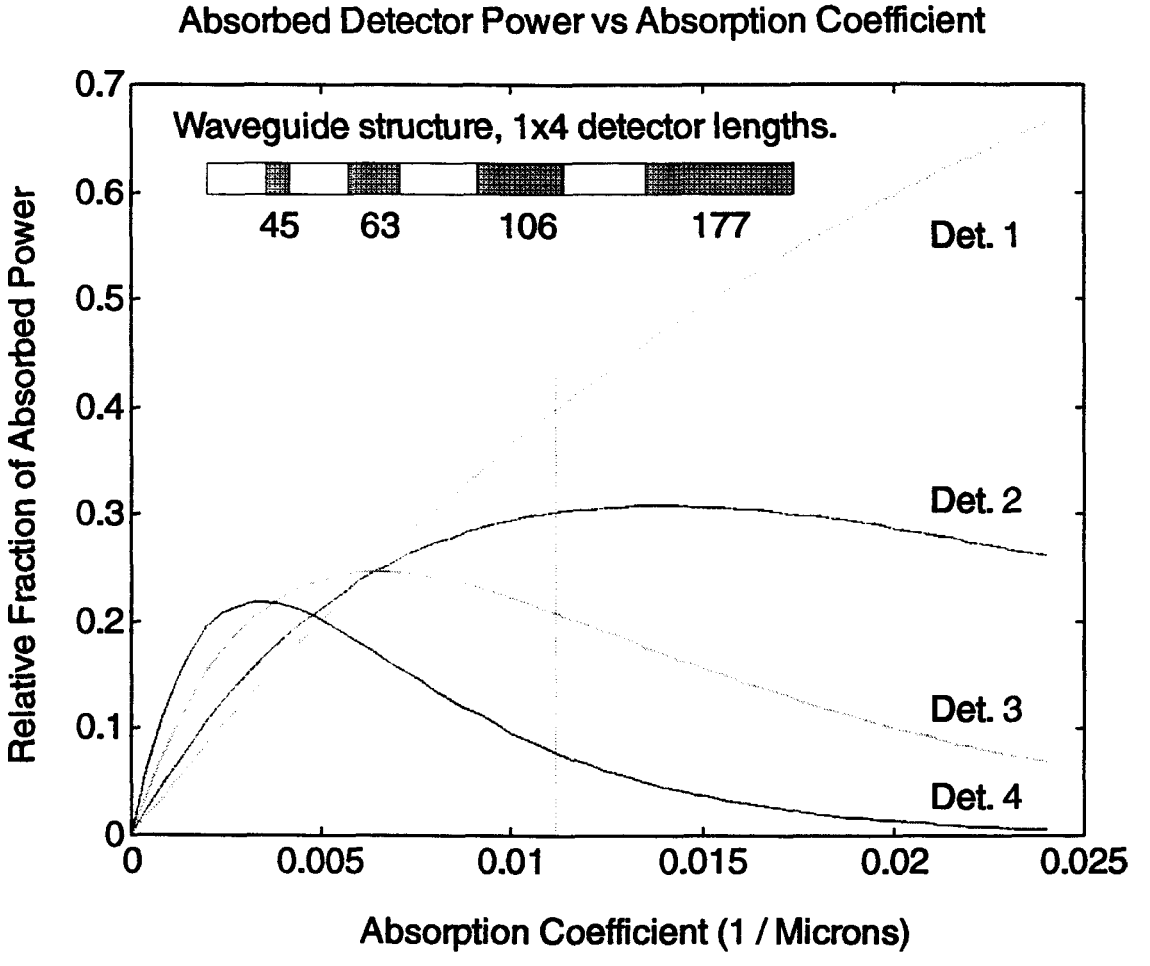

Figure 4.18 Ideal power absorption of each detector on a waveguide detector chain. The dashed line is the experimental absorption coefficient obtained.

In fact, it is evident, even if the graph is only an approximation, that we have missed the balancing point by quite a bit. To verify the validity of Figure 4.18 we will now vary the input laser wavelength and measure the absorption of power in each detector.

Figure 4.18 illustrated the absorption of power vs absorption coefficient. In Chapter Two

we have demonstrated that the absorption coefficient is a function of wavelength. Therefore, by sweeping out a wavelength range from 0.80 μm to 0.96 μm we can tune the absorption coefficient through a large absorption range (See Figure 2.7), and try to find a wavelength where all four detectors are balanced. We should obtain a graph which is similar to Figure 4.18 above. An important distinction between the two plots is that the absorption coefficient is not a linear function of wavelength and therefore, Figures 4.18 and 4.19 will not be directly related. This does not concern us because we are only interested in verifying a nominal operating wavelength. Another important distinction between Figures 4.18 and 4.19 is that Figure 4.19 appears backwards, this occurs because the absorption of the material increases as the wavelength decreases around the bandgap energy.

Figure 4.19 illustrates the experimental absorption of power vs wavelength. You will notice that both graphs are fairly consistent. While we do not have a wavelength that corresponds nicely to all four detectors absorbing as in Figure 4.18, at a wavelength of 0.85 μm, the first three detectors cross very close to one another. The fourth detector does not come close but this is consistent with the trend of detector 4 in Figure 4.18.

In the above analysis we have demonstrated a very important point. Since the absorption coefficient was not close to the required 70 cm^{-1}, by simply changing the input laser wavelength, all sixteen detectors on the 4x4 switch can be tuned to absorb different amounts of power.

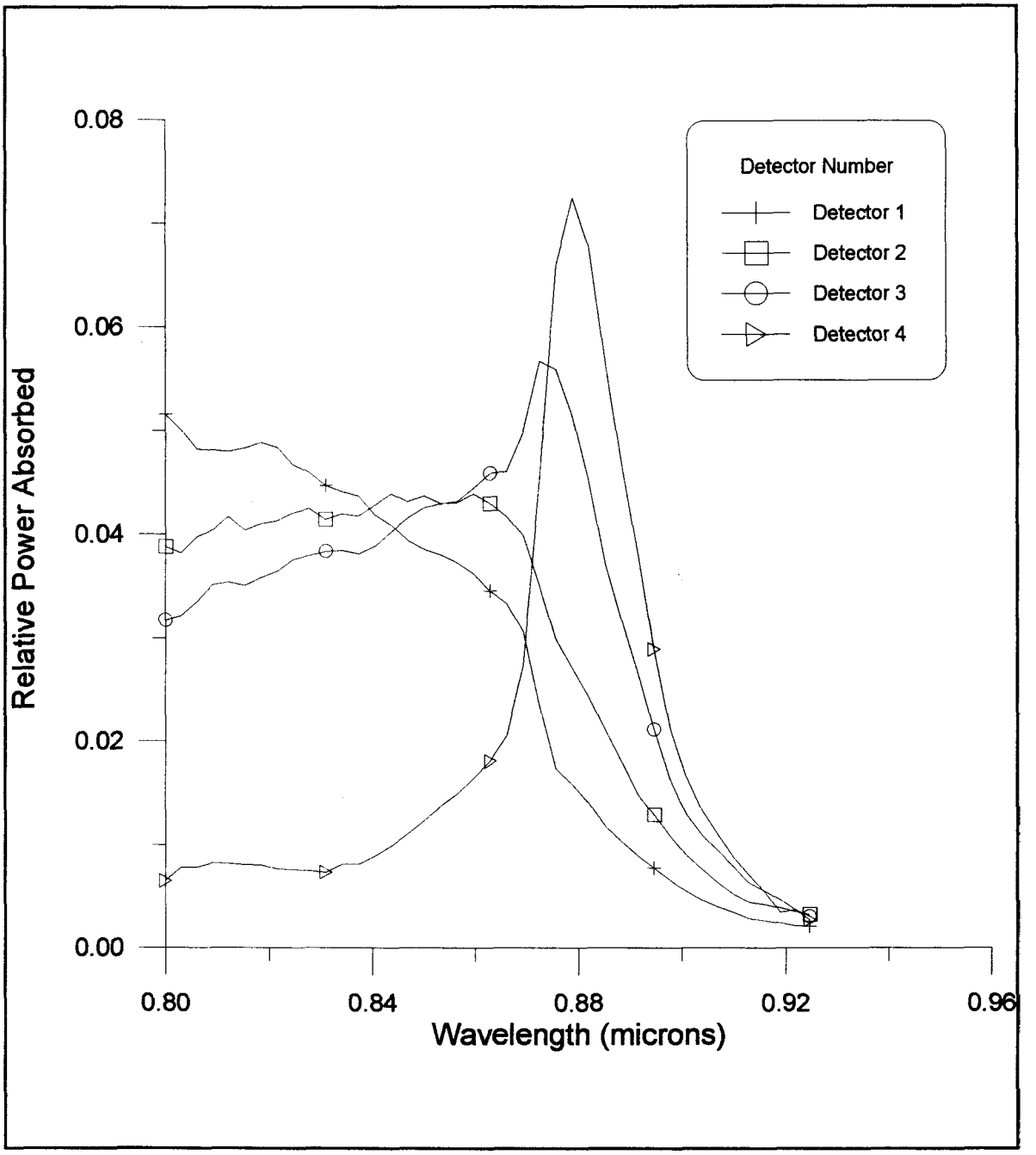

Figure 4.19 Measured absorbed power in a 1x4 waveguide/detector chain.

4.5) Frequency Response

Section 4.4 presented the dc characteristics of the waveguide integrated MSM detectors. We showed that the detectors behaved as a mix between photoconductors and photodiodes. The high speed performance of optoelectronic switches is perhaps the most important physical property which must be addressed since a good switch should be able to support large modulation frequencies. This section will examine the high speed performance of the detectors, and another important property of switches, the electrical isolation. We will show that these detectors, which exhibit a high photoconductive gain, are useful up to modulation frequencies of approximately 1 Ghz when electronic compensating circuits are employed.

The speed of semiconductor detectors is limited by two very important physical properties, the RC time constant and the carrier transit times. For an MSM photodiode the capacitance can be written as, [17,18]

$$C = \frac{K(k)}{K(k')}\,\epsilon_0\,(1+\epsilon_r)\,\frac{A}{fingerperiod}$$

$$where\ K(k) = \int_0^{\pi/2} \left[\frac{1}{\sqrt{(1-k^2\sin^2\varphi)}}\right] d\phi \qquad (3)$$

$$with\ k = \tan^2\left[\pi(fingerwidth)/4(fingerperiod)\right]$$

$$and\ k' = \sqrt{(1-k^2)}$$

For finger lengths of approximately 100 μm and finger widths of 2 μm, the capacitance is in the order of hundred femto farads [17]. When the circuit is connected to a fifty ohm load, the RC time constant is in the order of a few ps. This means that for MSMs the limiting factor in speed is normally the carrier transit times. If the speed of our detectors is governed solely by the transit time spread, the speed of the detectors should be well into the high MHz into the tens of GHz. As we will show our devices did not respond that quickly.

For photoconductors, the limiting factor in speed is the same as for photodiodes. But because photoconductors exhibit large photoconductive gains, the electrical 3 dB point as a function of frequency will be much lower than for a corresponding MSM photodiode. This occurs because as the modulation frequency approaches the carrier transit time spread, fewer and fewer

electrons will be generated in the gain process. In effect, because the photoconductive gain is a slow process as the frequency increases the amount of gain will decrease quite rapidly. The current for a photoconductor which has a modulated input laser power can be written as [19,12],

$$I_P = \eta e m F_0 A \frac{\tau}{T_r} \frac{1}{(1+j\omega\tau)} \tag{4}$$

where,

η is the quantum efficiency,

e the electronic charge,

m the modulation depth,

F_0 photon flux density,

A detector cross-section,

τ mean hole lifetime,

T_r electron transit time,

and ω is signal angular frequency.

For GaAs the recombination lifetime is typically on the order of 1 ns [10], and using a two micron finger spacing to compute the transit time spread we can plot equation 4 as a function of frequency. Figure 4.20 illustrates the loss in dB as a function of frequency for a typical GaAs MSM photoconductor.

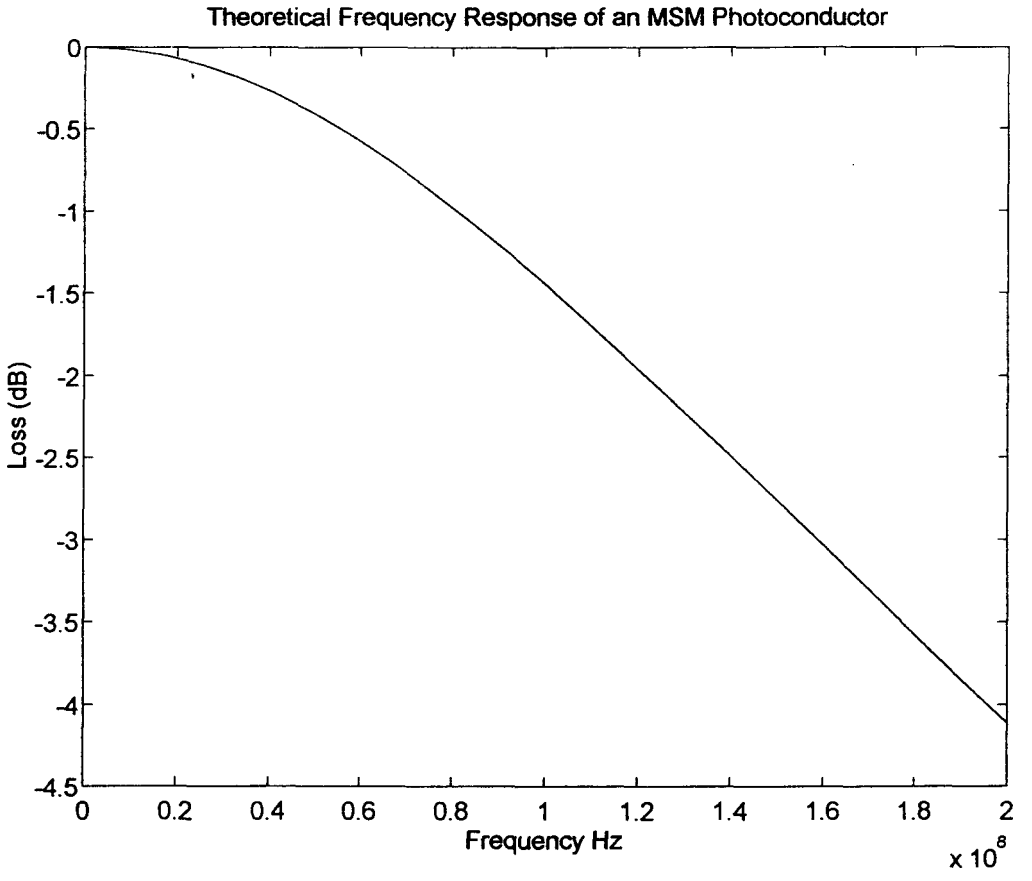

Figure 4.20 Frequency response of a one dimensional GaAs MSM photoconductor.

The 3dB point was calculated to be approximately 150 MHz. The low 3dB point is associated with a very large low frequency responsivity. Although useful, the 3dB roll-off obtained above should not be taken at face value. If the recombination lifetime was 50 ns, there would be almost a 150 MHz swing in the 3dB point. Figure 4.20 simply illustrates that the 3 dB response of photoconductors is typically in the range of a few hundred MHz. We will show that our devices have a similar frequency response.

The high speed experimental setup is illustrated in Figure 4.21. The speeds of the MSM's were measured with the use of a HP8702B Light Wave Component Analyzer, a high speed pico probe model 40A, and a New Focus high speed detector model 1434 which had a flat electrical response out to 15 GHz. The laser beam was modulated with the use of a CRC modulator good

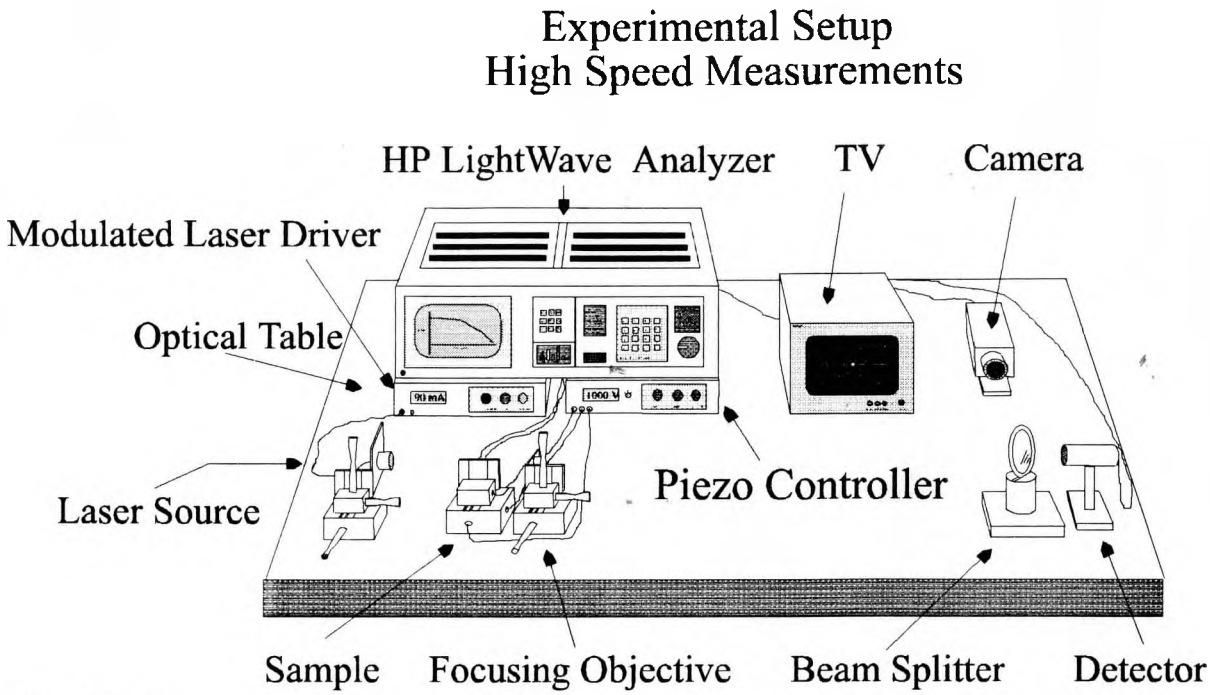

Figure 4.21

to 6 GHz. Before the speeds of the detectors were determined a system calibration was required. With the sample removed from the optical setup, the system frequency response was determined using the New Focus high speed detector. The system response is illustrated in Figure 4.22. To obtain the true response of the detectors the system speed must be divided out. The speed of the photodetectors was determined by first dividing out the response of the system and then normalizing the power to 1 at the starting frequency of 0.3 MHz. This does not alter the speed of the detectors and facilitates the graph's interpretation. Both 100 and 50 μm detectors were analyzed. There was no visible dependence in the speed of the detectors on the detector length. The speed of a typical 100 μm detector is illustrated in Figure 4.23. It is evident that the detectors are relatively flat to1 MHz and then begin to fall off quickly. This roll-off does not indicate that the devices are only good to 15 Mhz. By using a high pass filter we can flatten out the response of the detectors out to 1 GHz. This is possible because the detector responsivity is still quite high at 1 GHz. This has already been demonstrated by Veilleux et al. [1]. Their detectors had a response similar to our own, except the large roll-off was corrected electronically.

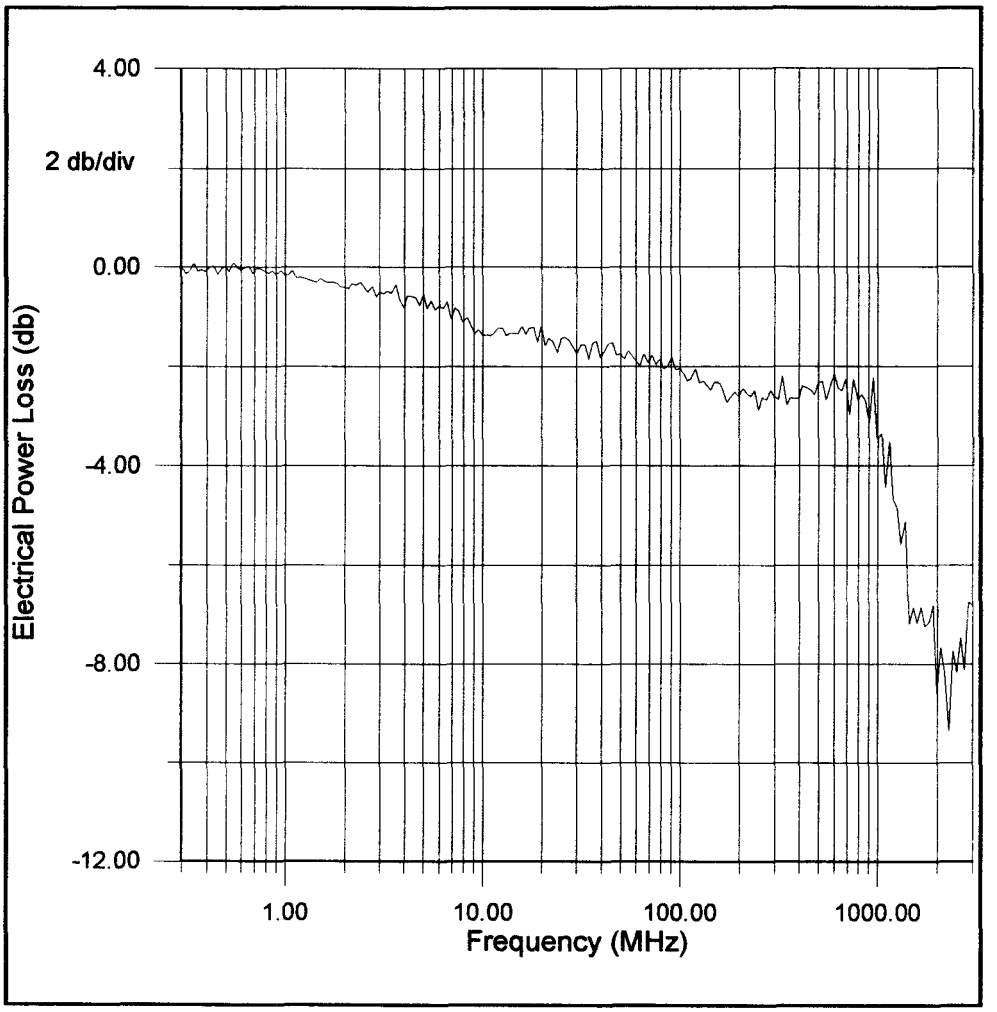

Figure 4.22 Frequency response of experimental setup.

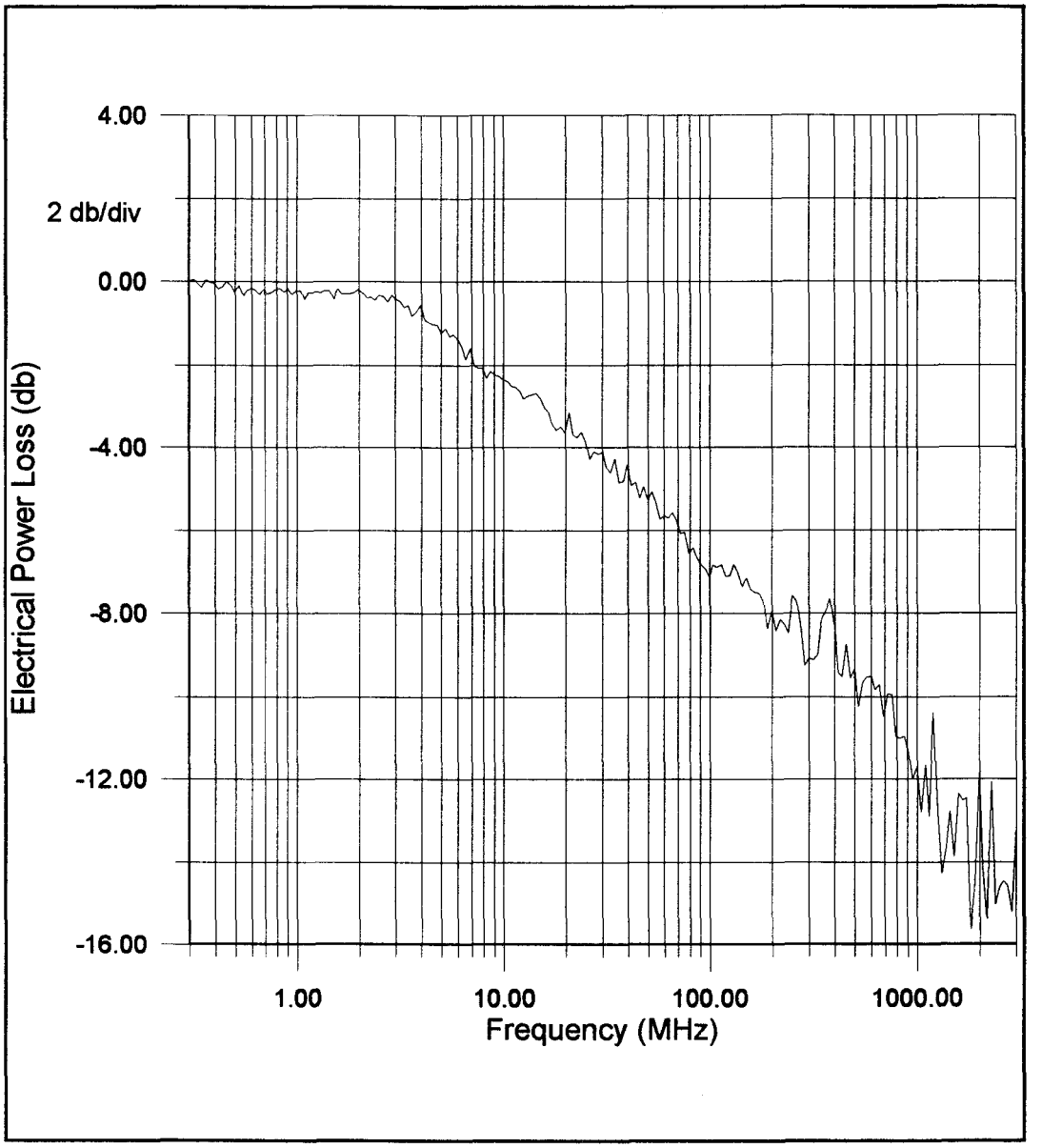

Figure 4.23 Typical frequency response of a 100 μm detector at 5 volts.

The 3dB point of this detector was determined to be approximately 15 Mhz. This is slower than the theoretical response determined above, but it is still in the same range. Table 4.7 illustrates the measured speed of other detectors as a function of voltage and size.

Table 4.7 Measured frequency response of various length single mode detectors.

Detector Length	Bias Voltage V	Measured 3dB Roll-off MHz
100 μm long 10 μm guides	5	15
100 μm long 10 μm guides	5	16
100 μm long 10 μm guides	3	18
100 μm long 10 μm guides	1	60
100 μm long 10 μm guides	5	15
100 μm long 10 μm guides	3	40
100 μm long 10 μm guides	1	75
100 μm long 10 μm guides	5	3
100 μm long 10 μm guides	5	1
50 μm long 10 μm guides	5	23
50 μm long 10 μm guides	3	72
50 μm long 10 μm guides	1	90
50 μm long 10 μm guides	5	6
*100 μm long 10 μm guides	5	11
*100 μm long 10 μm guides	3	12
*100 μm long 10 μm guides	1	36
100 μm long 3 μm guides	5	5

* Two finger detectors 6 μm finger spacing, CMSMs.

In general, the measured photodetector speeds were consistent with the calculation of the detector responsivities. The detectors do not exhibit any dramatic differences in speed for detectors of different length , but there is a noticeable difference in speed due to changes in bias. At first glance, this does not make any sense because the detectors are essentially faster at lower device biases. This occurs because the mobility for GaAs actually turns over and decreases for high applied fields. Therefore, by lowering the potential you lower the applied field thereby

increasing the mobility of the carriers and the speed of the photodetectors.

The ac responsivities for the detectors can be approximated by using the measured dc responsivities and the frequency response obtained above. Because the current is directly proportional to the responsivity, the ac responsivity can be obtained by determining the current as a function of frequency. Figure 4.23 illustrates the optical power attenuation as a function of frequency for a 100 μm detector. Since the power was obtained by using a 50 ohm load we simply use $P=I^2R$ to determine the current and therefore the responsivity as a function of frequency. The dc responsivity for this detector was determined to be approximately 0.77 A/W, by looking at the current attenuation as a function of frequency, we can show that the detector responsivity at 1GHz is still relatively high at 0.1 A/W. In effect, the high responsivity offsets the low frequency response. If compensating electronics were used to flatten the response of this detector, it could easily be used up to 1 GHz.

The isolation of a detector is another very important parameter of switches. It is defined as the ratio of power measured when the device is on over the power measured when the device is off. The isolation must be relatively high since if someone is connected to the switch who is not supposed to be receiving the information there should be sufficient attenuation of the signal. The isolation is what favours the use of MSM over p-i-n photodiodes. In the case of p-i-n diodes, to obtain the required high isolation the detectors must be forward biased, thereby wasting large amounts of power. For MSMs the high isolation is achieved by simply not applying a bias to the device, which is both economical and efficient. Figure 4.24 illustrates the measured photocurrent of a typical 50 μm long detector. The lower curve is the photocurrent under zero bias and the upper curve is the photocurrent at the operating voltage. For GaAs photoconductors and photodiodes, isolations of 60dB or greater have been obtained [2,3]. The isolation of the 50 μm detector in the figure varies from 40 dB at low frequencies to 20 dB at 3 GHz. This indicates high leakage currents and RF noise present in the detector at high frequencies. Other devices had similar isolations.

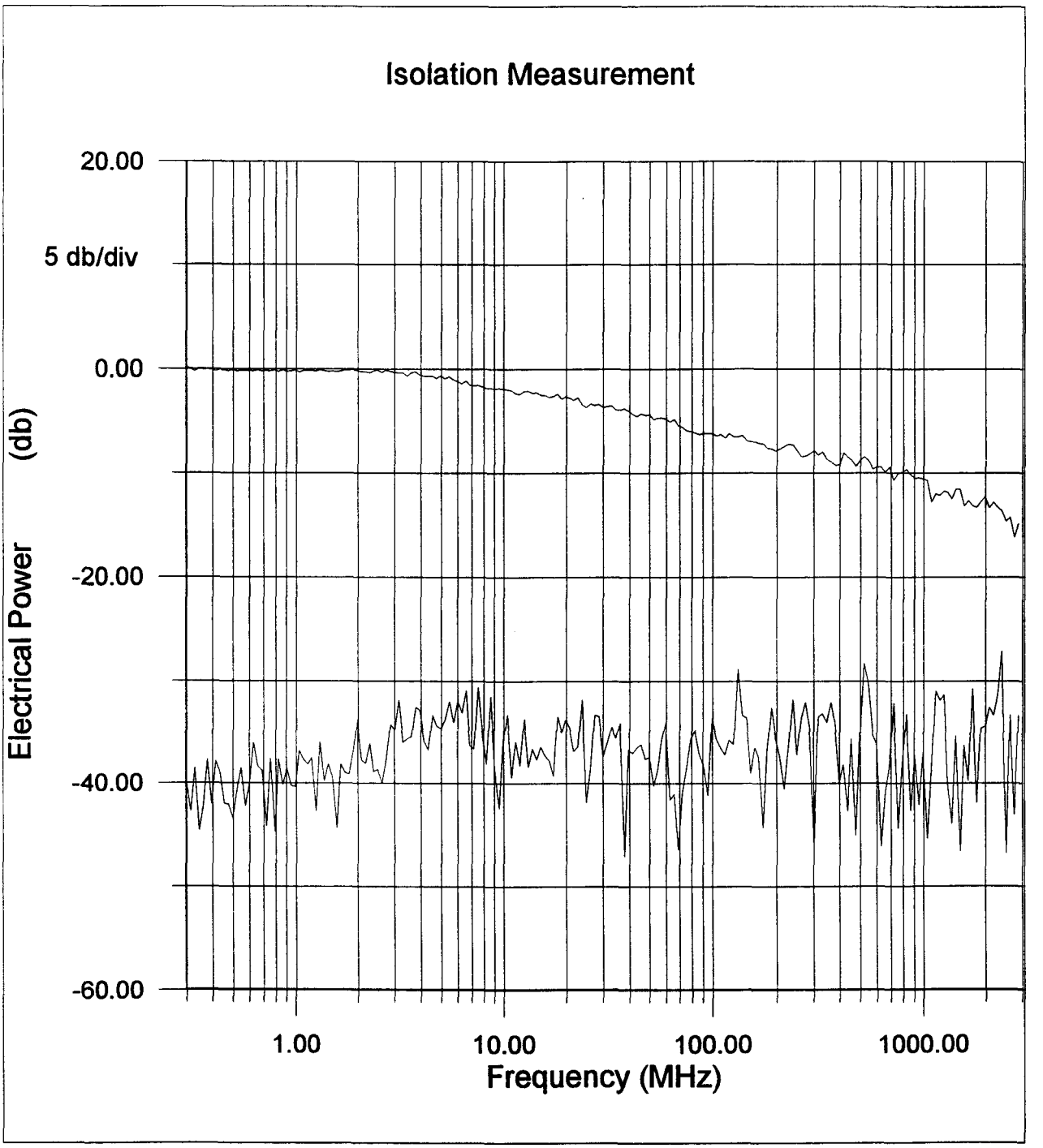

Figure 4.24 Measured photocurrent with bias (upper curve) and measured photocurrent without bias (lower curve) for a 50 μm long single mode detector.

Chapter 5: Conclusions and Future Work

5.1) Conclusions

The speed and simplicity of MSM photodetectors has made them prime candidates for integration in optoelectronic circuits. In this thesis we have demonstrated the operation of both surface integrated MSM waveguide detectors and a four by four element optoelectronic matrix switch. Two waveguide structures were designed, and it was found that the single mode structure was required to obtain adequate light sensitivity. The high responsivities exhibited by the 10 μm single mode waveguide detectors was a direct indication of photoconductive gain. This in effect enhanced the response of the detector at low frequencies but was eliminated when the frequency approached 1 GHz.

There are a number of improvements which can significantly increase the electrical performance of the fabricated devices. The first and most important modification to the devices is the actual processing. Since, the metal was deposited along the sides of the ridge waveguides, the number of surface states present might have caused the material to form an ohmic contact at the sides of the waveguides. This would have destroyed any Schottky diodes formed on top of the GaAs cap layer because the resistance of an MSM photodiode is much larger than a corresponding MSM photoconductor. To overcome this problem, it is possible to make the GaAs cap layer as big as the width of the fingers but, this would destroy the confinement of the optical mode in the waveguide. Therefore, the only solution is to grow an oxide layer, before the deposition of the metal, and open widows in the glass directly above the waveguide/detector structure. Another modification in the processing is to etch isolation trenches down to the GaAs substrate layer. This would eliminate any electrical noise from adjacent waveguides and any optical leakage between waveguides.

To further improve the detector sensitivity, to the incident laser light, the quantum efficiency of the detectors can be increased by grading the aluminum concentration in the GaAs cap layer from 15% (The waveguide concentration.) to 0%, 0.1 microns from the metal contacts. This would grade the absorption coefficient from approximately 0 to 10^4 , and the photons would

then be absorbed deeper into the cap layer. This would ensure that most of the photo-generated carriers are created closer to the metal semiconductor fingers, which would increase the quantum efficiency, and hence the responsivity of the detectors.

5.2) Future Work

While the object of this thesis was to examine the integration of photdetectors and waveguides into an optoelectronic switch, the grand plan was to use the information obtained to develop a Franz Keldysh, optoelectronic switch. This would allow control over how much light is absorbed and would circumvent the difficulty in tailoring the absorption coefficient to a specific value, which would make the fabrication of large array systems more practical.

Appendix 1

I) Mask Design:

The optoelectronic mask for both the integrated waveguide detectors and 4x4 switch is illustrated in Figure A.1. The motivation for the mask design of the integrated waveguide MSM detectors was to acquire optical and electrical information of the material. To accomplish this various detector configurations were drawn to obtain as much flexibility as possible. For the optoelectronic switch the only criteria was to try and equalize the absorption of all four detectors. This section, of appendix 1, will examine some of the different structures designed in the mask which facilitated the analysis of material characteristics.

The integrated waveguide MSM detector sections were designed for both the 10 μm and 3 μm waveguide widths as is illustrated in Figure A.1. There were two types of interdigital MSM contacts designed. Conventional MSM were designed with the electrodes perpendicular to the direction of optical power flow, as in Figure 1.2 and, a second MSM detector, which was not analyzed in this thesis, was designed with only two electrodes, both parallel to the direction of the light propagation. These detectors are labelled CMSM (Capacitance-metal semiconductor metal contact.) in Figure A.1 and, were designed with the intention of using the electrooptic effect so that the detector absorption can be controlled electrically.

Figure A.2 illustrates the typical layout of the MSM waveguide detectors. Depending of which waveguide, the detectors are either spaced at increasing distances, equal distances or, with no spacing at all. This is done so that both optical and electrical characterization can be compared with different detector chains.

The lengths of the detectors were also varied so different amount of absorption could be compared with different amounts of measured current. In general the masks flexibility made it possible to examine detector sections which absorbed a lot of power. This was done by connecting many detectors in a chain with two micron spacing between them (See Figure A.3). By measuring the current in the chain and looking at the electrical attenuation, an estimate of the

optical attenuation can be obtained.

The lengths of the 4x4 detectors were designed by assuming an absorption of 3dB in 100 microns. Since we can approximate the loss in a waveguide using an exponential decay of power, the corresponding lengths to balance the switch are 44, 77, 100 and 177 microns (See Figure A.4). Because the passive waveguide losses were not known, they were ignored in the above calculation. This would not have a big effect since the passive waveguide losses will be small compared to the detector losses..

Once the basic structure of the mask was completed, the number of layers were separated to obtain the different mask levels required in the processing. The separated mask is illustrated in Figure A.5. There were five mask levels in total, the processing steps are discussed in the next section.

II) Processing:

This section of Appendix 1 will outline all processing steps followed in the fabrication of the optoelectronic switch and integrated waveguide detectors.

1) Cleaning and preparation of samples for processing using Methanol Trichloroethylene process.

-Heat two separate baths of Methanol and Trichloroethylene to 90 degrees Celsius.
-Place sample in first Methanol beaker and leave for 10 minutes.
-Place sample in second Methanol beaker leave for 10 minutes and repeat for Trichloroethylene baths.

2) Oxide removal process for GaAs.

-Prepare HCl:DI, 1:1 and NaOH:DI, 1:1.
-Dip samples in HCl:DI solution for 30 seconds, rinse in DI Water for 2 minutes and repeat procedure for NaOH:DI solution.

3) Preparation of samples for standard lithographic procedure.

-Spin on SiO_2 glass at 3000 rpm for 20 seconds and bake samples at 250 degrees overnight.

-Remove samples from oven, cool down and spin Shippley 1808 photoresist at 4000 RPM for 30 seconds.

-Soft bake samples for 1.5 minutes at 110 degrees Celsius.

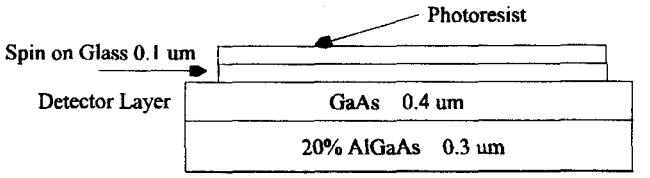

4) Patterning of GaAs absorbing layer.

-Using the 'Mesa' square of the processing mask, see Figure 3. Expose the sample with the Mask aligner for three seconds. This patterns the GaAs absorbing layers on the photoresist.

-Develop using 351 developper:DI, 1:5 solution for approximately 25 seconds. This procedure cannot be quantified exactly since many factors affect the developing time.

-Hardbake sample at 150 degrees for two minutes.

-Dip sample in Hf:NH_4F, 1:10 solution for thirty seconds. This removes the glass from all regions that were not patterned in the exposure, and leaves the top of the GaAs detectors unexposed.

-Remove the photoresist using the positive photoresist stripper heated to 85 degrees Celsius in two separate 5 minute baths.

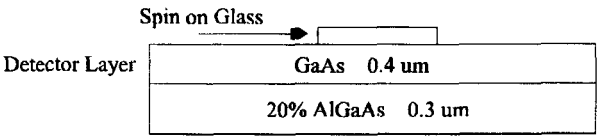

5) Etching of GaAs absorbing layer.

-Mix Sulphuric acid H_2SO_4, Hydrogen peroxide H_2O_2, and DI water in a 1:8:160 solution ratio. This will etch the GaAs at approximately 1/4 micron/minute. The sample must be placed and agitated once inside the solution. If the sample is not agitated the etch time will be wrong. The samples were then etched by removing all of the GaAs in regions where light absorption was undesirable. The etch times for both the single mode and multimode structure were different since the GaAs layers had different thicknesses.

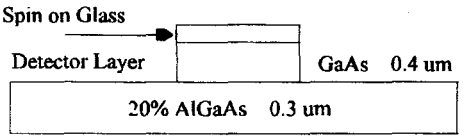

6) Patterning of the ridge waveguide.

-Spin on 1808 photoresist as in step three, but do not spin the SiO_2 Glass.
-Using the 'Ribs' square of the processing mask see Figure 3. Expose the sample with the Mask aligner for three seconds. This patterns the ribs on the photoresist.
-Develop using 351 developper:DI, 1:5 solution for approximately 25 seconds.
-Hardbake sample at 150 degrees for two minutes.

7) Etching of the ridge waveguides.

-Mix Sulphuric acid H_2SO_4, Hydrogen peroxide H_2O_2, and DI water in a 1:8:160 solution ratio. This will etch the AlGaAs at approximately 1/4 micron/minute as in step 5.

The sample must be placed and agitated once inside the solution as before.

-The samples were then placed inside the bath and etched for approximately one minute. Since an etch depth of 0.25 microns determined in chapter two, was determined adequate for proper mode confinement.

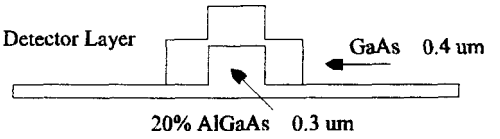

8) Patterning of the Metal

-Repeat procedure three (3).

-Using the 'PWIN' square of the processing mask, see Figure 3. Expose the sample with the Mask aligner for three seconds. This patterns windows above the GaAs absorbing layers on the photoresist.

-Develop using 351 developer :DI, 1:5 solution for approximately 25 seconds.

-Hardbake sample at 150 degrees for two minutes.

-Dip sample in Hf:NH_4F, 1:10 solution for thirty seconds. This removes the glass from all regions that were not patterned in the exposure, and leaves the top of the GaAs detectors exposed. This allows the metal to make a Schottky contact only to the GaAs.

-Remove the photoresist using the positive photoresist stripper heated to 85 degrees Celsius in two separate 5 minute baths.

-Spin Shippley 1808 photoresist at 4000 RPM for 30 seconds, wait five minutes.

-Soft bake samples for 1.5 minutes at 80 degrees Celsius.

-Using the 'Metal' square of the processing mask, see Figure 3. Expose the sample with the Mask aligner for 3.5 seconds. This patterns MSM above the GaAs absorbing layers on the photoresist.

-Dip samples in toluene for six minutes.

-Develop using 351 developer :DI, 1:5 solution for approximately 1.5 minutes seconds. (This undercuts the photoresist, which allows acetone to remove the photoresist in all undesired places.)

-Deposit TiPtAu, or PtAu, different metals were tried to enhance the Schottky contact.

-Place samples in acetone for 10 minutes and clean with methanol and DI water. This should remove the metal everywhere except where the MSM's are placed.

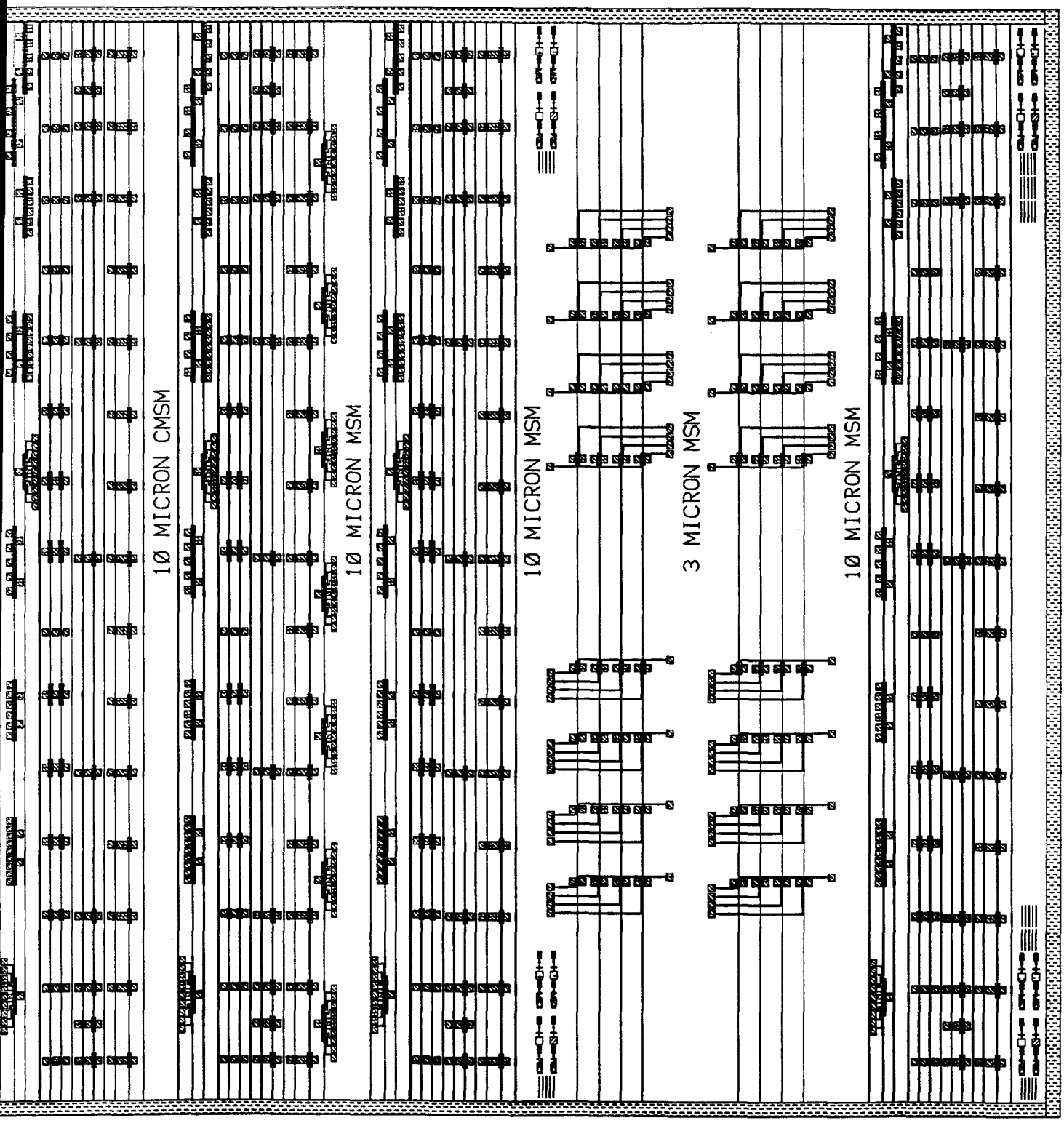

Figure A.1 Mask Structure.

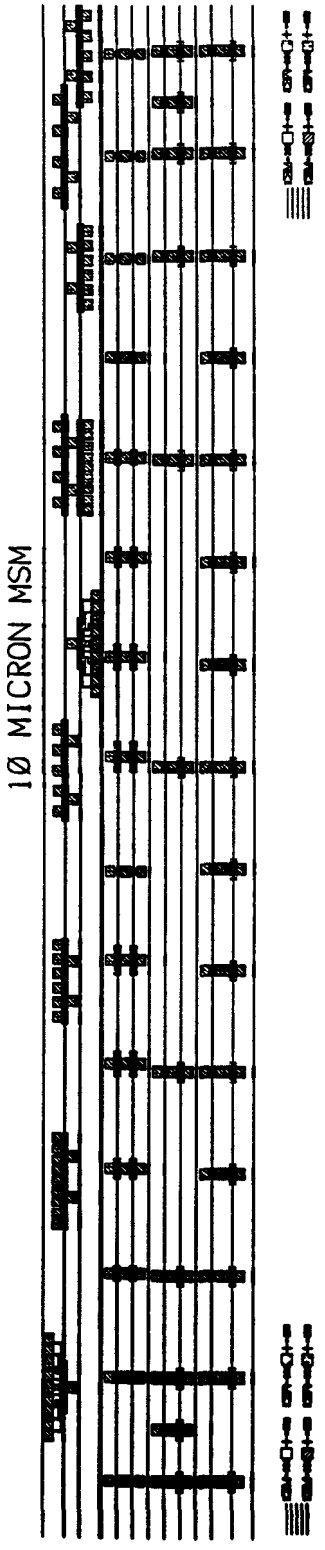

Figure A.2 Integrated waveguide/detector characterization mask.

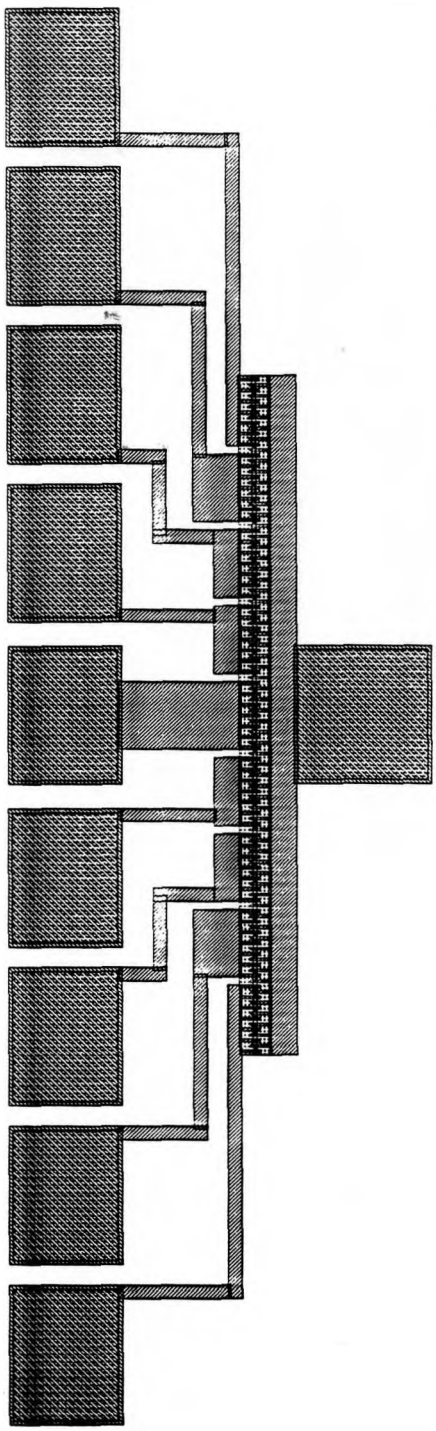

Figure A.3 Chain detectors, with 2 μm finger spacing. This was used to acquire the optical attenuation

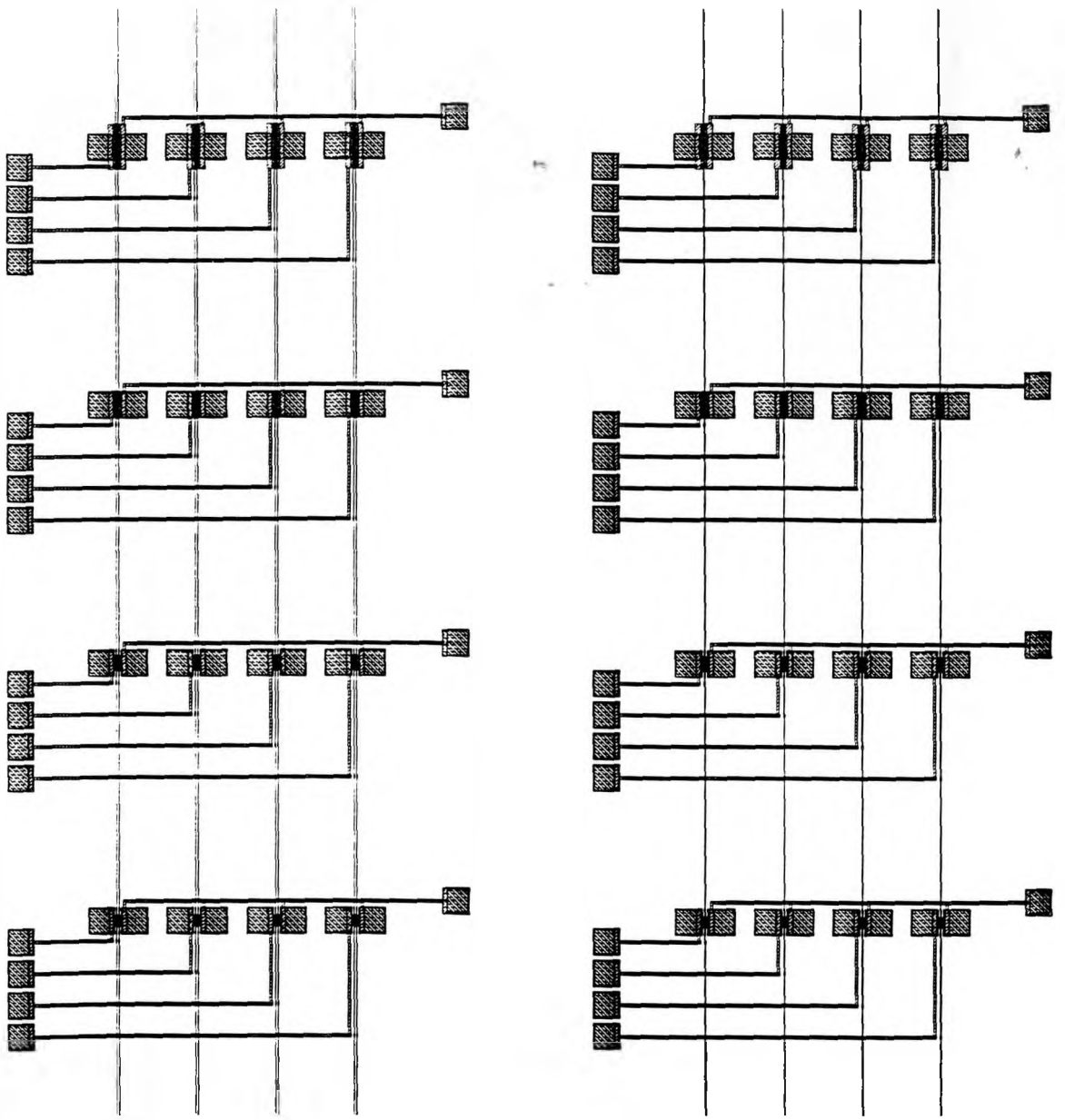

Figure A.4 Ten micron and three micron waveguide 4x4 optoelectronic switch.

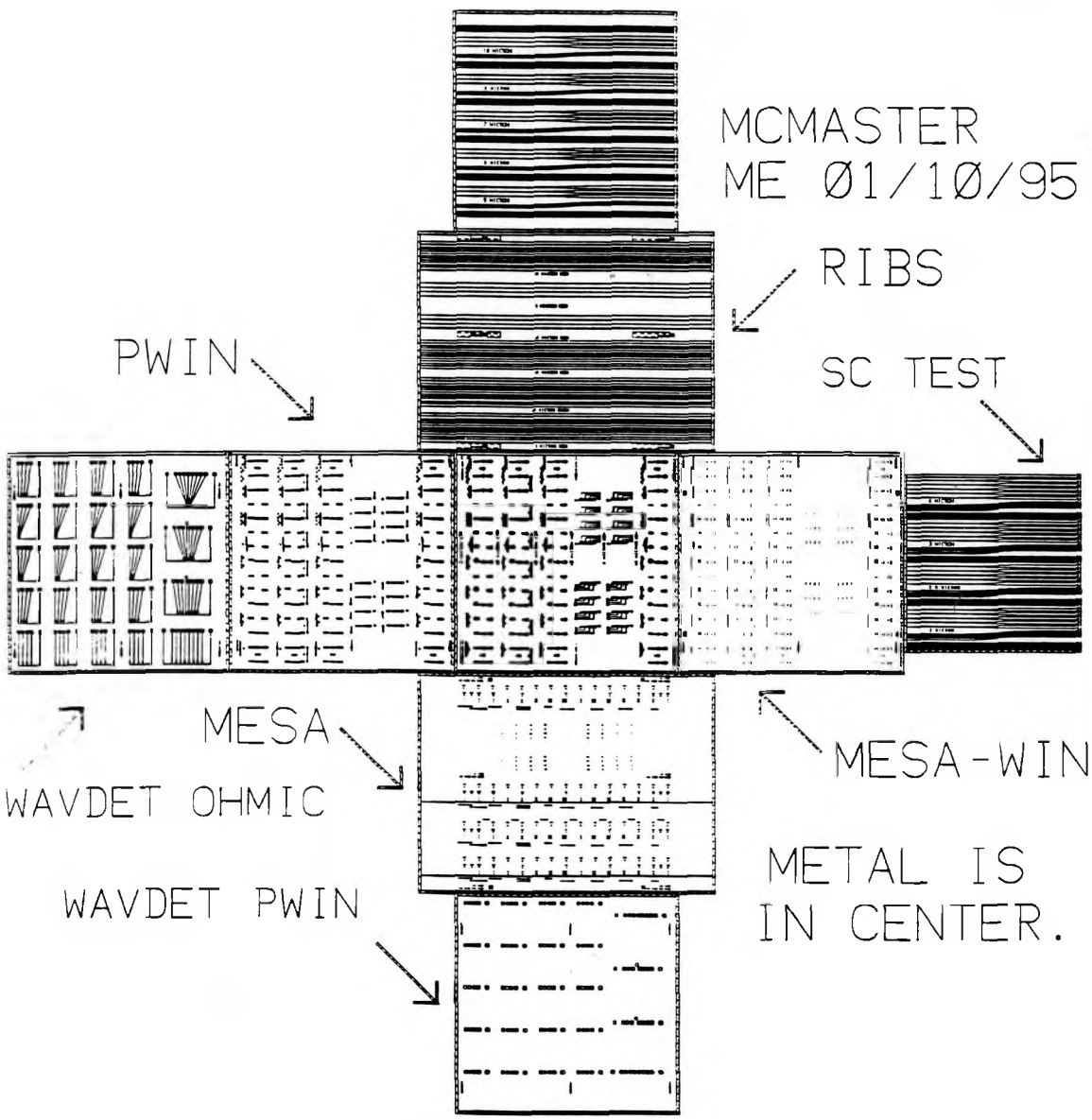

Figure A.5 Processing mask.

REFERENCES

[1] Veilleux, M., MacDonald, Ian R. An Optoelectronic Switching Matrix With High Isolation. Journal of Lightwave Technology, Vol. 10, No. 7, July 1992. p. 988.

[2] MacDonald, Ian R. Terminology for Photonic Matrix Switches. IEEE Journal on Selected Areas in Communications, Vol. 6, No. 7, August 1988. p. 1141.

[3] MacDonald, Ian R. Optoelectronic Matrix Switching. Canadian Journal of Physics, Vol. 67, 1989. p. 389.

[4] Gouin, F., Beaulieu, C., Noad, J. Design, Fabrication and Characterization of High Speed GaAs MSM's for OEIC Applications. Conference on Applications of Photonic Technology, June 21-23 1994, Toronto.

[5] Jackson, D. John. Classical Electrodynamics, 2nd Ed. New York: John Wiley and Sons, Inc., 1962, 1975.

[6] Walpita, L. M. Solutions for Planar Optical Waveguide Equations by Selecting Zero Elements in a Characteristic Matrix. Journal Optical Society of America, Vol. 2, No. 4, April 1985. p. 595.

[7] Tamir, Theodor. Guided-Wave Optoelectronics, 2nd Ed. Berlin Heidelberg: Springer-Verlag., 1988, 1990.

[8] Marcuse, Dietrich. Theory of Dielectric Waveguides, 2nd Ed. San Diego: Academic Press, Inc., 1974, 1991.

[9] Hunsperger, R. G. Integrated Optics: Theory and Technology, 3rd Ed. Berlin Heidelberg: Springer-Verlag., 1991.

[10] Saleh, E. A. Bahaa, Teich, Carl Malvin. Fundamentals of Photonics. New York: John Wiley and Sons, Inc., 1991.

[11] Hecht, Eugene. Optics, 2nd Ed. Reading, Massachusetts: Addison-Wesley Publishing Company, 1990.

[12] Sze, S. M. Physics of Semiconductor Devices, 2nd Ed. New York: John Wiley and Sons, Inc., 1981.

[13] Sze, S. M., Coleman, D. J. JR., Loya, A. Current Transport in Metal-Semiconductor-Metal (MSM) Structures. Solid State Electronics, Vol. 14, June 1971. p. 1209.

[14] Zeghbroeck, J. Van Bart, Patrick William, Halbout, Jean-Marc, Vettiger Peter. 105 Ghz Bandwidth Metal-Semiconductor-Metal Photodiode. IEEE Electron Device Letters, Vol. 9, No. 10, October 1988. p. 527.

[15] Narayanan, W. Ng, A., Hayes, R. R., Persechini, D., Yap D. High-Efficiency Waveguide-Coupled λ=1.3 μm $In_x Ga_{1-x} As$/GaAs MSM Detector Exhibiting Large Extinction Ratios at *L* and *X* Band. IEEE Photonics Technology Letters, Vol. 5, No. 5, May 1993. p. 514.

[16] Deri, Robert J., Kapon, Eli. Low-Loss III-V Semiconductor Optical Waveguides. IEEE Journal of Quantum Electronics, Vol. 27, No. 3, March 1991. p. 626.

[17] Soole, Julian B. D., Schumacher, Hermann. InGaAs Metal-Semiconductor-Metal Photodetectors for Long Wavelength Optical Communications. IEEE Journal of Quantum Electronics, Vol. 27, No. 3, March 1991. p. 737.

[18] Lim, Yu Chin, Moore, Robert A. Properties of Alternately Charged Coplanar Parallel Strips by Conformal Mappings. IEEE Transactions on Electron Devices, Vol. ED-15, No. 3, March 1968. p. 173.

[19] DiDomenico, M. Jr., Svelto, O. Solid-state Photodetection: A Comparison Between Photodiodes and Photoconductors. *Proc.* IEEE, Vol. 52, 1964. p. 136.